An Investigation of the Sound Field Above a Surface With Periodically-Spaced Roughness

Thesis

An Investigation of the Sound Field Above a Surface With Periodically-Spaced Roughness

Thesis Submitted By

Alexander Stronach

For the Degree of

Doctor of Philosophy

July 2019

School of Engineering & Innovation

Faculty of Science, Technology, Engineering and Mathematics

The Open University

Milton Keynes, United Kingdom

Certificate of Originality

Faculty of Science, Technology, Engineering & Mathematics

School of Engineering and Innovation

The Open University Walton Hall

Milton Keynes

MK7 6AA

United Kingdom

Tel +44 (0) 1908 653686

This is to certify that I am responsible for the work submitted in this thesis, that the original work is my own except as specified in acknowledgements, in text or in bibliography, and that neither the thesis nor the original work contained therein has been submitted to this or any other institution for a degree.

_____ (Signature)

_____ (Date)

Supervisors

Professor Keith Attenborough

Research Professor

Acoustics Research Group

School of Engineering & Innovation

The Open University

Milton Keynes, United Kingdom

Dr Shahram Taherzadeh

Associate Professor

Acoustics Research Group

School of Engineering & Innovation

The Open University

Milton Keynes, United Kingdom

Professor David Sharp

Research Professor/Head of School

Acoustics Research Group

School of Engineering & Innovation

The Open University

Milton Keynes, United Kingdom

Conference Publications

A**.** Stronach, S. Taherzadeh, K. Attenborough, I. Bashir (2016), 'Air-borne acoustic surface waves over periodic rough surfaces,' *Proceedings of the Institute of Acoustics,* **38** (1)

A. Stronach, S. Taherzadeh, K. Attenborough (2017), 'Surface waves due to periodically-spaced strips on an acoustically-hard surface,' *International Congress on Sound & Vibration 24,* London

A. Stronach. S. Taherzadeh, K. Attenborough (2019), 'An investigation of the sound field above surfaces with periodic roughness,' *INTERNOISE 2019,* Madrid

Awards

Young Acoustician Award

Presented by

International Institute of Noise Control Engineers

For a paper at

Internoise 2019, Madrid

Abstract

Outdoor audio-frequency acoustic signals can be amplified passively at selected frequencies by exploiting the interaction of incident sound with surfaces composed of periodically-spaced rectangular strips on an acoustically-hard base.

When sound is incident near grazing on acoustically-rigid ground with roughness composed from elements with periodic sub-wavelength spacing, air-borne acoustic surface waves are generated due to a high imaginary-component to the surface impedance as well as the formation and coupling of quarter-wavelength resonances in the gaps. This allows for passive amplification of acoustic signals at the surface wave frequency. This thesis provides a detailed, systematic study into the total sound field generated above surfaces with periodic roughness and how the topography and geometry affect the generation of air-borne acoustic surface waves.

Surfaces with a high number of scattering edges per wavelength result in strong surface wave generation due to high reactive component to the impedance. As the gap is increased thereby reducing the number of edges per wavelength, the gap resonances couple less strongly and the surface behaves as a rough surface. As the number of edges per wavelength approaches one, the signal enhancement is provided by Bragg diffraction. Through measurements and predictions, it is found that surface wave enhancement is not detected by a collocated geophone in sand via acoustic-seismic coupling since the sand is sufficiently absorbing so that no surface wave is detected. This systematic study provides a detailed insight into the formation of audio-frequency surface waves generated over periodically-rough surfaces.

Acknowledgements

I would firstly like to express my deepest gratitude to my supervisors, Professor Keith Attenborough and Dr Shahram Taherzadeh for their support, guidance and patience throughout this PhD project. It has been an honour to work alongside such esteemed and knowledgeable supervisors. I especially appreciate the patience in times of personal difficulty.

I would like to extend thanks to Komcept Solutions Ltd (KSL) for their part-funding of this PhD project and the supply of geophones for testing. The application of the theory to sensor performance has been extremely valuable and rewarding.

The assistance from the support staff at the Open University has been greatly appreciated. The supply of materials and organization of conferences and workshops has provided invaluable knowledge and experience.

The support from my peers at the Open University has been fantastic. Every conversation and cup of coffee has provided much needed support and relief at times of difficulty.

I would like to further extend my appreciation to my family without whom I would never have finished the thesis. The unwavering support has kept me going and thus I dedicate this thesis to them.

Finally, to the Taherzadeh family (Shahram, Halimeh, Aydin and Nina), I would like to give thanks for making me feel so at home at the Open University and in Milton Keynes. The hospitality, especially during the writing up phase, has made this final stage of the PhD run that bit smoother so I am forever grateful.

Table of Contents

List of Figures

List of Tables

Chapter 1

Introduction

This project is part-funded by Komcept Solutions Ltd (KSL) who are experts in the police and public security market. As part of their range of products, they develop geophones for the detection of seismic signals which are used, in particular, in perimeter security systems. These geophones are powered by lightweight, every-day batteries and deliver information remotely from their location. As a result, an increase in sensitivity results in an increased energy demand on the sensor which limits the distance and frequency range over which these sensors operate. Therefore, it is desireable to introduce passive means of enhancing the received signal in the space between the source of noise and the receiver.

The thesis is concerned with audio-frequency sound propagation above arrays of periodically-spaced rectangular strips placed on an acoustically-rigid surface. The presence of the strips effectively introduces a finite surface impedance. Near-grazing, broadband sound is enhanced at some frequencies and absorbed at others. This is well documented in the literature [32, 54] and has been proposed as a method of noise mitigation. The sound level enhancement at lower frequencies is associated with the generation of air-borne acoustic surface waves which counteracts any noise reduction, so the addition of absorption has been proposed to reduce them. However, it is the aim of this project to explore the signal-enhancement potential of surfaces formed from periodically-spaced rectangular strips on an acoustically-hard boundary and exploit the generation of surface waves to provide passive frequency-selective amplification at audio-frequencies which results in enhanced sensor performance. This project also aims to aid in the simplification of the design of such surfaces by relating surface wave frequency and magnitude to the geometry and topography of the rough surface.

In this context, the interaction of the incident sound field with periodically-spaced rectangular strips and the physical mechanisms that could be used to enhance acoustic signals is explored in detail using both experimental and numerical techniques.

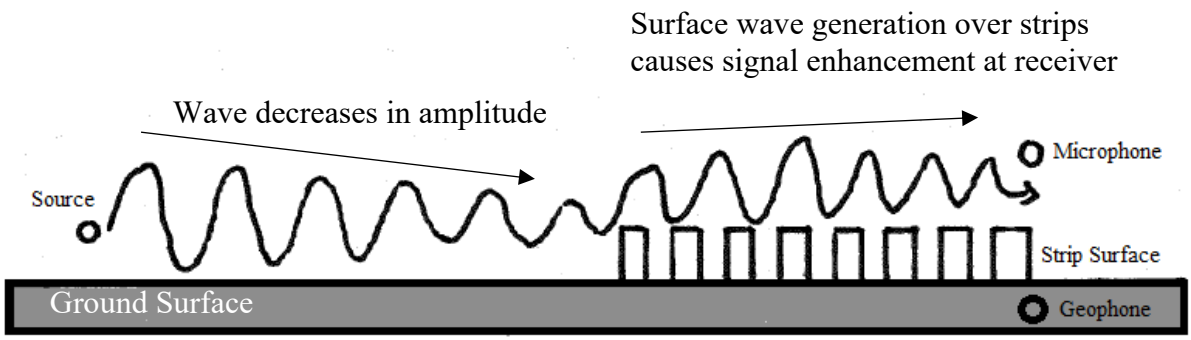

Figure 1. 1 *Simple diagram showing sound propagation over a periodically-rough surface.*

Enhanced acoustic signals are visible in the frequency-domain via measurements of excess attenuation with reference to a hard surface. Excess attenuation is defined as the ratio of the total sound field over a surface and the sound field in the absence of the surface. Signal enhancement is visible in the frequency domain as any feature with a magnitude greater than 6 dB which is the excess attenuation corresponding to a doubling of sound pressure as a result of constructive intereference due to reflection off an acoustically-rigid surface.

Sound propagation at audio-frequencies over model-impedance surfaces and their signal-enhancing properties is well documented in the literature [21 – 38]. Propagation at ultrasonic frequencies and surface wave generation as a result of scattering [39, 40] is also documented. This thesis contains details of the total sound field over a periodically-rough surface at audio frequencies, accounting for the effects of the interactions within the gaps between strips on

the total sound field detected at the receiver. A review of the theoretical basis for surface waves, the experimental evidence for their existence and the interaction of sound with rough surfaces is given in chapter 2. Chapter 3 outlines models for sound propagation over periodically-spaced strips and the numerical and analytical techniques used in this project. Chapter 4 describes the materials and methods used in exploring aspects of sound propagation over finite arrays of periodically-spaced strips. An MLS-driven measurement system has been re-designed for this project in MATLAB, the details for which and the experimental procedure is explained in detail in chapter 4. Data verifying the generation of surface waves over periodically-spaced strips as well as other enhancement features that arise due to the periodicity and finite extents of the strip array are presented in chapter 5. In chapter 6, the Boundary Element Method (BEM) is used to investigate systematically the effects of varying strip height, width and spacing. On the basis of pressure contour maps, it is found that as well as multiple edge diffraction, 'organ pipe' resonances are formed in the gaps between the strips which may interact and are affected by the finite length of the array in contributing to the overall pressure field. The conclusions derived from the previous chapters are summarised in chapter 7 along with suggestions for future work.

Chapter 2

Literature Review

2.1 Introduction

In this chapter, a review of previous work outlining the origin of the surface wave and model surfaces with which to generate them. Section 2,2 gives a historical review of the theoretical formulation of surface waves due to sound propagation incident near grazing over impedance planes. Section 2.3 gives details of the origin of surface waves over rough surfaces. Sections 2.4 and 2.5 reviews previous work in the generation of surface waves over model impedance surfaces at audio and ultrasonic frequencies and the potential for the use of such surfaces for noise mitigation and signal enhancement.

2.2 History & Origin

Lord Rayleigh gave one of the first accounts of surface waves in an elastic medium. Rayleigh [1] presented a theory for waves upon the plane of the free surface of a semi-infinite homogenous isotropic elastic solid where the disturbance is contained within a superficial region whose thickness is comparable to that of the wavelength. He showed that the disturbance motion became negligible at a distance of a few wavelengths from the free surface. He also showed that the motion at the surface is elliptical with the amplitude along the vertical axis being nearly double that along the horizontal axis. Rayleigh waves arise along the surface of elastic solids when the material is disturbed by an impact. Different types of surface waves which are air-borne have been predicted and measured over porous (impedance) surfaces and surfaces composed from lighting diffuser lattices

The existence of air-borne surface waves over an impedance plane has been investigated since the early 20th century. The correct solution to the Helmholtz equation above a complex impedance plane has been the topic of much literature. The Helmholtz equation for the velocity potential $\psi(x,y,z)$ is [2],

$$\left(\nabla^2 + k_0^2\right)\psi = f \tag{0.1}$$

subject to the impedance boundary condition,

$$\frac{\partial \psi}{\partial z} + ik_0\beta\psi = 0 \tag{0.2}$$

in the half space $z > 0$ where β is the admittance and k_0 is the wavenumber. It is well known that if k_0 is real then the solution satisfies the radiation condition $\psi \to 0, R \to \infty$ where $R = \left(x^2 + y^2 + z^2\right)^{1/2}$. However, for an impedance plane it is necessary to add a small imaginary part to the wavenumber which introduces dissipation in the medium therefore $k_0 = k + is_0$. The solution to this has been the topic of much debate in literature which will be reviewed here.

The debate arose since the solution for the plane wave reflection coefficient has a denominator that tends to zero under certain conditions thereby requiring the use of contour integration methods when solving the point-to-point propagation problem to approximate the integral over plane waves.

Sommerfeld [3] treated the electromagnetic problem of wave propagation above a plane surface with extended reaction. In Sommerfeld's solution, a surface wave term appeared as part of the total field. Weyl [4] treated the problem some time later and found no surface wave term in his solution. Ingard [5] studied the acoustic case of the problem, using Weyl's method, over a locally reacting surface and obtained an exact solution for the reflected term

under certain conditions, though he gave no account of a surface wave term. Wenzel [6] used Sommerfeld's approach and found Ingard was in fact missing the surface wave term from his solution. He introduced the surface wave to the total wave field solution and found that the surface wave traps energy close to the surface resulting in an amplitude greater than that due to total reflection at the boundary. Wenzel also deduced that in the far field the surface wave decays cylindrically, with the square-root of distance, from the source. Thomasson [7] corrected Ingard's method and showed that it is possible to rewrite the exact solution of the scalar wavefield produced by a point source over an infinite impedance boundary using a single integral along a steepest-descent contour and a Hankel function.

Thomasson's method starts with the solution deduced by Wenzel [6],

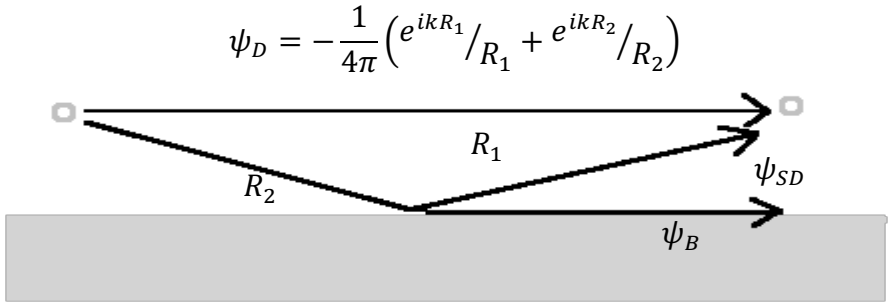

Figure 2. 1 *Sound propagation near grazing over an impedance plane results in contributions from direct, reflected and surface waves.*

$$\psi = -\frac{1}{4\pi}\left(\frac{e^{ikR_1}}{R_1}+\frac{e^{ikR_2}}{R_2}\right)+\psi_R \tag{0.3}$$

where $R_1 = \left[x^2+y^2+\left(z-z_0\right)^2\right]^{1/2}$ and $R_2 = \left[x^2+y^2+\left(z+z_0\right)^2\right]^{1/2}$, the terms in brackets is the sum of direct wave and the image source, and ψ_R is a contribution from reflection at the impedance boundary given by,

$$\psi_R = \frac{ik_0\beta}{2\pi}\int_0^\infty \frac{ke^{-mh}}{m\left(ik_0\beta-m\right)}J_0\left(kr\right)dk, \tag{0.4}$$

$$m = \left(k^2-k_0^2\right)^{1/2} \quad , \quad \mathrm{Re}\left(m\right)>0 \tag{0.5}$$

$$h = z+z_0 \tag{0.6}$$

$$r = \left(x^2+y^2\right)^{1/2} \tag{0.7}$$

Thomasson used the method of steepest descent to approximate the contour in the complex plane. His exact integral solution was,

$$\psi = -\frac{1}{4\pi}\left(\frac{e^{ikR_1}}{R_1}+\frac{e^{ikR_2}}{R_2}\right)+\psi_R \tag{0.8}$$

$$\psi_R = \psi_{SD}+\psi_B, \quad \mathrm{Re}\left(\gamma_0\right), \quad \mathrm{Im}\left(\beta\right)<0 \tag{0.9}$$

$$\psi_R = \psi_{SD}, \quad else \tag{0.10}$$

where,

$$\psi_B = \frac{1}{2}k_0\beta H_0^{(1)}\left[k_0 r\left(1-\beta^2\right)^{1/2}\right]e^{-ik_0h\beta} \tag{0.11}$$

is the surface wave expression and ψ_{SD} can be considered as the 'space wave' (sometimes referred to as the ground wave) travelling separately to the surface wave, ψ_B. $H_0^{(1)}$ is the

Hankel function of zero order and the first kind which for large arguments (i.e. in the far field) provides a solution where the exponential term implies that the surface wave decays exponentially with height above the surface and the Hankel function implies that the surface wave spreads cylindrically along the surface. The term γ_0 in equation 1.5 is the singularity along the steepest-decent contour given by,

$$\gamma_0 - \nu\cos(\theta_0) + \left(1-\nu^2\right)^{1/2}\sin(\theta_0) \tag{0.12}$$

where ν is the surface admittance. Thomasson split his solution into a 'space wave' and a 'surface wave' under the condition that the surface impedance is finite. However, he claimed this a consequence of the mathematics rather than something physical and that any experimental anomalies in literature should be referred to as surface waves with caution. Brekhovskikh [8,9] studied propagation over a comb-like surface with a purely imaginary 'spring-like' elastic impedance as opposed to a mass-like (purely real) impedance. He considered Rayleigh waves as a degenerate case of the reflection of plane waves at a boundary. He found that a liquid or gas does not support surface wave propagation since the mean kinetic energy is greater than the mean potential energy. However, a surface wave can cling to a surface which has an elastic or 'spring-like' impedance. The plane surface wave has an amplitude that deceases exponentially with height above the boundary and a phase velocity which is less than that in free space. He also found that the surface wave is excited when the condition,

$$h > \frac{k_0}{\sin(\theta_0)} \tag{0.13}$$

is satisfied where $h = \sqrt{k_0^2 - \alpha^2}$ and k_0 is the wavenumber and α relates to the attenuation. Brekhovskikh only considers the case in which the impedance is purely imaginary and does not consider the accompanying space wave as in Thomasson's work. Ivanov-Shits and

Rozhin [10] continued Brekhovskikh's work by carrying out measurements over a lattice composed of thin aluminium strips placed on a ridge of plywood. They found good agreement between theoretical and measured values of the phase velocity and the vertical attenuation of the surface waves although this is not conclusive proof of the existence of surface waves since the speaker system used was not a point source. Furthermore, they did not take into account the dispersive nature of the surface wave.

Donato [11] carried out an analysis of the sound field from a point source over a locally reacting complex impedance boundary. He gave a detailed account of the conditions for the existence of surface waves as well as expressions for the vertical attenuation and phase speed of surface wave. Donato claims that if the complex impedance is comparable in magnitude to the incident medium and is mostly reactive, then the surface wave is detectable. The condition under which a surface wave can exist is:

$$\left|\frac{X_N}{R_N}\right| > \left(1+\frac{R_N^2}{\left(R_N^2+X_N^2\right)^2}\right)^{-1/2} \tag{0.14}$$

i.e $\mathrm{Im}\left(Z_N\right) \geq \mathrm{Re}\left(Z_N\right)$ where,

$$\frac{Z_N}{\rho c} = R_N + X_N \tag{0.15}$$

is the normalized characteristic impedance of the locally reacting ground surface composing of a resistive component R_N and a reactive component X_N . In the case of a purely reactive surface, the surface wave speed is given by,

$$v = c\frac{X_N}{\left(1+X_N^2\right)^{1/2}} \tag{0.16}$$

However, there will still be a non-zero real component to the surface impedance and so the complex phase speed is given by,

$$v = \frac{c}{\left(1+\frac{1}{Z^2}\right)^{1/2}} \tag{0.17}$$

The vertical attenuation is given by,

$$\alpha = k_0 \frac{X_N}{X_N^2 + R_N^2} \tag{0.18}$$

and, horizontally, the surface wave attenuates cylindrically with $r^{-1/2}$.

He also compared measured and theoretical values of the pressure at the impedance boundary and found good agreement. Further work by Donato [12] made measurements of the of the exponential attenuation factors for the surface waves both in the direction of propagation along a complex impedance surface and perpendicular to it. He carried out the measurements using a rectangular lattice structure (a lighting diffuser lattice) on a wooden board and found good agreement between the surface impedance calculated from the expressions for vertical attenuation and the impedance measured using an impedance tube.

Attenborough *et al.* [13] give a detailed review of the approaches of Ingard, Donato and Thomasson. They derive an exact solution for the field due to a point source above a homogenous and isotropic porous ground (i.e. with complex impedance). It was found that the surface wave arises mathematically as a consequence of the asymptotic form of a complementary error function for positive and negative arguments. This differs from Donato's solution which does not take account of such a function. Raspet and Baird [14] use Tolstoy's [15] test for a true surface wave to study acoustic surface waves above reactive surfaces. Tolstoy demonstrated that the surface wave over a comb-like surface is indeed a true surface wave by allowing the upper-half-space to become incompressible, corresponding to an infinite sound speed and a constant density in the upper half-space. A true surface wave will propagate independent of the body wave in the upper half space. Raspet and Baird found

that the term derived in previous literature is indeed a true surface wave that propagates separately from the body wave in the upper half-space.

Attenborough and Richards [16] used a modified Biot model of a poroelastic half-space in the context of predicting acoustic-to-seismic coupling. As well as contributions from the direct and ground waves in the air, they found contributions from two surface-wave types; one being a Rayleigh-type wave which is dependent upon the properties of the elastic frame and the other being a surface wave related to the pore structure. In the far-field, however, the dominant surface wave will be the Rayleigh-type wave. This Rayleigh-type surface wave was detected by Allard *et al.* [17] in an air-air saturated porous layer interface. They used a plastic foam, the frame for which has a bulk modulus of the same order of magnitude as air but is much heavier. The wave was frame-borne and is related to a pole of the reflection coefficient in the porous layer, as predicted in previous literature.

2.3 Propgation Over Roughness

Tolstoy [18] studied the coherent scattering of spherical waves by applying a 'small roughness' boundary condition developed by Biot. Coherent scatter is more important than incoherent scatter if the size of the roughness elements, d is much less than the wavelength of the incident sound, λ so that $d/\lambda \ll 1$. Biot replaced the scattering elements with a smooth distribution of dipole and monopole sources under the condition that the centre-to-centre spacing between roughness elements, h is small compared to the wavelength so that $d/\lambda < h/\lambda \ll 1$. Tolstoy's solution, using a simple effective boundary condition, contains two independent arrivals: the body wave and a boundary (surface) wave. This surface wave is similar to that predicted by Brekhovskikh [8, 9] over comb-like surfaces and was found to decrease rapidly with height above the surface and cylindrically with range so that in the far-

field, it is the dominant arrival. Tolstoy also found that for rigid hemispherical bosses under farfield, near-grazing conditions, the normalised spectrum of the scattered wave is given by,

$$P_s = \frac{\varsigma}{2\pi} k^2 \left[\theta^2 + \frac{2\pi}{kr} \exp\left[-2\varsigma k^2 \left(z + z_0 \right) \right] + 2 \left(\frac{2\pi}{kr} \right)^{1/2} \theta \sin\left(kr - \frac{\pi}{4} \right) \exp\left[-\varsigma k^2 \left(z + z_0 \right) \right] \right]^{1/2} \tag{0.19}$$

where k is the wavenumber, r is the range and $\theta = \tan^{-1}\left[\left(z + z_0 \right) / r \right]$ with z and z_0 being the receiver and source heights respectively. The term ς is the scattering parameter which has units of length and is proportional to the volume per unit area of the elements and is a function of the shape and packing density of the roughness elements [18]. At grazing angles, the scattered wave is the boundary or surface wave with amplitude,

$$P_B = \varsigma \left(2\pi r \right)^{-1/2} k^{3/2} \tag{0.20}$$

The above case was studied experimentally by Medwin *et al* [19]. For hemispheres and spherical bosses, the direct wave amplitude in the half-space is $P_D = \left(2\pi r \right)^{-1}$ so that,

$$\frac{P_B}{P_D} = \varsigma \left(2\pi r \right)^{1/2} k^{3/2} \tag{0.21}$$

Short range experiments in which spherical pulses were propagated over hemispherical and spherical bosses show that the spectral slope of the resulting boundary waves did obey the $k^{3/2}$ and $r^{1/2}$ dependence expected from 1.13. However, at longer ranges the results deviated from this relationship. The boundary wave amplitude did not continue to grow as predicted in 1.13 but instead tended towards a constant value. One explanation for this discrepancy is that after a certain range, incoherent scatter dominates. A second explanation suggests that after a certain range, the phase lag between the scattered elements and the direct response results in destructive interference between the two contributions. Similar measurements were carried out over cylinders and assumed to obey the same relationships. However, once again,

discrepancies arose in longer-range measurements as a result of multiple diffraction contributions due to the widely- spaced elements. Finally, measurements were carried out over a variety of contiguous wedges. The ratio of boundary wave amplitude to direct wave amplitude increases linearly with volume/area and increases with increasing slope of the wedge size. For long range measurements, the ratio asymptotically approaches a constant value which supports the idea that the boundary wave 'self-destructs' due to destructive interference with the direct contributions.

Further analysis into coherent sound scatter from different roughness element shapes was carried out by Tolstoy [20] who determined that in a general case, the boundary wave is a result of energy stored between closely packed roughness elements and exchanged with the compressional energy from the source, resulting in horizontally propagating modes.

2.4 Propagation Over Model Impedance Surfaces

Once the existence of surface waves was well established in literature, both theoretically and experimentally, further investigations into their properties were carried out over model impedance surfaces. Daigle [21] used acoustical pulses above the model surface used by Donato [12]. The narrow-band nature of the pulses allowed for separation in the time-domain of the surface wave contribution using Thomasson's model [7]. He successfully separated the surface wave as a later arrival since it travels slower than the speed of sound in air. Attenborough and Hutchinson-Howorth [22] performed measurements over single and double lattice layers using tone bursts. They separated the surface wave contribution of the total field from the main impulse showing that the surface wave does indeed travel slower than the speed of sound in air. Daigle *et al* [23] also carried out measurements over model impedance planes constructed from multiple lattice layers using tone bursts.

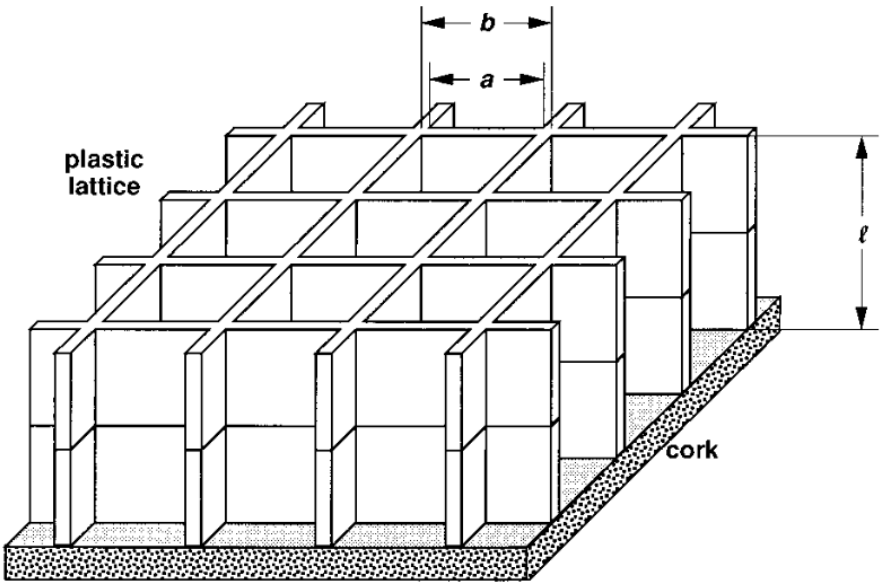

Figure 2. 2 *Model surface construction. Image obtained from [23]*

They achieved good separation of the surface wave from the body wave with the surface wave showing obvious dispersion. However, in order to achieve complete separation, the model surface must be purely reactive which they found was difficult due to leakage between the layers introducing a resistive component to the surface impedance. A modified surface impedance was proposed to be,

$$Z_{eff} = i\rho c \cot\left(\frac{kl}{2}\right)\frac{1-q\tan^2\left(kl/2\right)\sin^2\left(\theta_2\right)}{1+q+\varepsilon\cot\left(kl/2\right)\sin^2\left(\theta_2\right)}\left(1+\delta^2\right) \tag{0.22}$$

$$q = \frac{1+i\rho c\cot\left(kl/2\right)/Z_s}{1-i\rho c\cot\left(kl/2\right)/Z_s} \tag{0.23}$$

$$\varepsilon = \frac{i\rho c b^2}{a^2 Z_L} \tag{0.24}$$

$$Z_L = \frac{-i\omega\rho_s(\omega)(b-a+0.015)}{\eta b} \tag{0.25}$$

$$\rho_s(\omega) = \rho\left[\frac{1-\tanh\left(\sqrt{i}\lambda\right)}{\sqrt{i}\lambda}\right]^{-1} \tag{0.26}$$

$$\lambda = \frac{\eta}{2}\left(\frac{\omega\rho}{\mu}\right)^{1/2} \tag{0.27}$$

The term ε accounts for leakage in between the adjacent lattice elements; q relates to the finite impedance of the underlying surface (cork in this case); and δ accounts for the wall thickness of the plastic that makes up the lattice structure and has a value of 0.141. The term θ_2 is the angle of incidence of the reflected wave from the impedance discontinuity. The terms a and b are the inner and outer dimensions of the lattice elements, respectively and l is the height of the lattice structure. The terms Z_s and Z_L are the specific surface impedance of the cork and the acoustical leakage impedance between cells where η is the dimension of the gap between cells. For an ideal and purely reactive surface, $\varepsilon = 0$, $q = 1$ and $\delta = 0$ giving an effective impedance of,

$$Z_{eff} = i\rho c\cot(kl) \tag{0.28}$$

Stinson *et al* [24] carried out further measurements of surface wave formation at a discontinuity between an acoustically-hard plane and a finite impedance plane. They used the same model surface configuration as Daigle *et al* [20] as the impedance plane. They found good agreement between theory and experiment and also recorded some interference between the direct path and edge-diffracted paths due to the finite width of the lattice.

Zhu *et al* [25] studied surface wave formation due to scattering from comb-like impedance gratings. It was shown that the scattered field consists of plane bulk waves which propagate

away from the grating known as ‘diffraction modes,’ and ‘surface modes’ which propagate in a layer just above the grating. When the grating period is much less than the incident wavelength (i.e. at low frequencies), no surface wave can be excited since the grating structure is equivalent to a plane impedance surface. However, when the incident wavelength is comparable to the grating period, surface waves can form at high frequencies with large amplitudes and resonance phenomena are predicted despite homogeneous plane-wave incidence. It is worth mentioning, however, that localised sound sources can produce surface waves at low frequencies over a grating with an appropriate structure.

Surface waves have been detected outdoors by Albert [26] using pistol shots over a thin layer of snow on frozen ground. Albert confirmed the generation of a surface wave as a later arrival in the time-domain with an exponentially decaying amplitude with increasing receiver height above the surface. The results were compared with a theoretical evaluation of the surface wave pole using residue theory and good agreement was found. However, this is the only time surface waves have been detected under natural outdoor conditions. As described above, it is easier to construct model surfaces with controlled acoustical characteristics than to rely on the required properties being possessed by natural outdoor ground surfaces.

Further work on surface wave formation at ultrasonic frequencies over various roughness element shapes has been carried out. Kelders *et al* [27] used a modal model that was initially developed to model diffraction of electromagnetic waves over rectangular-groove gratings for the same structures in air. They found good agreement between the velocity of the surface wave between the modal model and measurement although the idealised model did not account for damping effects due to viscous and thermal exchanges within the grooves resulted in some discrepancy since losses inside the slits and the air were neglected. Lauriks *et al* [28] carried out measurements over triangular gratings and truncated triangular gratings. Attempts to model the surface using a modal model, Tolstoy model and a Rayleigh model

show that the modal model is the most effective at modelling surface wave generation over such a surface, however there is still discrepancies in the prediction of $\sin\theta$ as a function of frequency where θ is the angle of incidence. No explanation for this discrepancy was reported. Allard *et al* [29] generated ultrasonic surface waves over a layer indented by a doubly periodic set of holes having square-shaped cross sections.

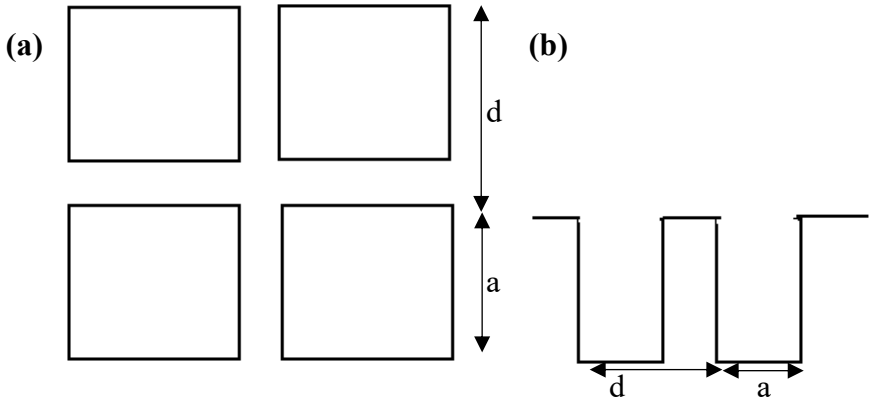

Figure 2. 3 *Doubly periodic grating* ***(a)*** *topside view,* ***(b)*** *side-view*

A modal model was used to model the surface and good agreement was found between measurement and prediction. Moreover, a 'simple model' was developed by taking the first mode and using Tolstoy's effective impedance model but with a modified groove depth. This simple model showed good agreement with the modal model. In all cases, the modal model was found to be yield better results in modelling sound over gratings than Tolstoy's method. Zhu *et al* [30] studied the potential for passive amplification due to the generation of air-borne acoustic surface waves over strips of finite impedance. Measurements were carried out for different strip widths and it was shown that better agreement between theory and experiment is achieved for wider strips due to the minimisation of leakage. Tapered strips and impedance strips with added planar and parabolic reflectors indicate further amplification potential. It also shows that the surface waves generated can be reflected by vertical

structures due to interference between direct and reflected waves. Optimisation of the reactive nature of the surface impedance could lead to greater amplification. Daigle and Stinson [31] continued the work carried out by Zhu but introduced a rigid comb-like surface to achieve passive amplification at lower frequencies. Indeed, passive amplification at low frequencies was achieved – potentially useful in the control of low-frequency noise. However, the structures they designed are rather large and thus potentially impractical. More recently, Bashir *et al* [32] investigated the possibility of using low parallel walls or lattice surfaces for the purpose of traffic noise reduction. Measurements of insertion loss were made over brick lattices on hard ground and showing useful levels of noise reduction due to the diffraction assisted rough ground effect. A by-product of such a surface is the generation of air-borne acoustic surface waves as a result of the effective surface impedance having a greater reactance than resistance. Bashir's aim was to reduce the negative effects of the surface wave on the insertion loss achieved by the lattice structure. It was found that the introduction of absorbent material in between strips in the first 50% of the array significantly reduced the effect of the surface wave without having an effect on the beneficial noise reduction properties of the surface. Bashir [33] carried out further investigation into the surface waves that can be generated over surfaces with periodic roughness using periodically-space rectangular strips placed on an acoustically rigid surface through measurements of excess attenuation and numerical simulations using a 2D Boundary Element Method (BEM). Surface waves were detected that travel slower than the speed of sound in air with an amplitude decreasing exponentially with receiver height above the surface. Bashir also attempted to model the strips [33] and single, double and triple lattice layers [32] as effective impedance surfaces in order to improve computational speed in the modelling of such surfaces. It is difficult to model the 3D lattice layers using a 2D BEM and so an indirect approach was taken by modelling both the lattices and the strips using the Kelders-Allard

modal model [27] and as a hard-backed slit-pore layer. The Kelders-Allard model under-predicts the effective layer depth of the surface which shifts features in the excess attenuation spectra to higher frequencies resulting in poor predictions overall. The slit-pore model gave better agreement and it was found that the strip-surfaces may be regarded as a locally reacting rigid-framed hard-backed slit-pore layer with an effective depth slightly larger than the strip height provided the spacing between the roughness elements was 50% or less than the height of the roughness elements.

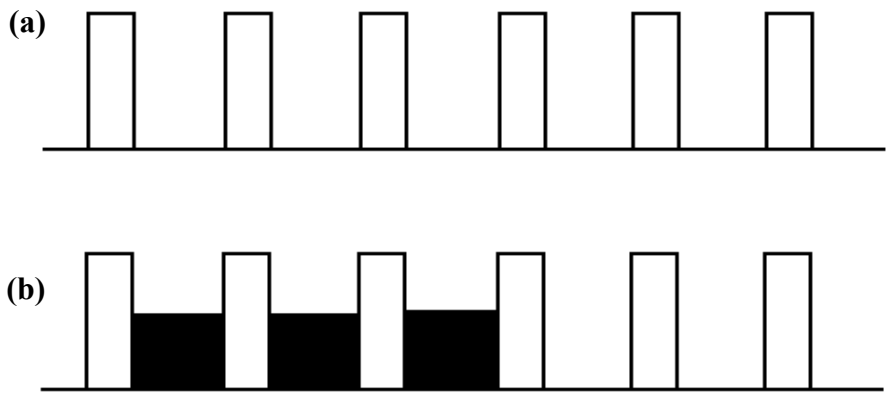

Figure 2. 4 *Periodically-spaced rectangular strips* ***(a)*** *without absorbing material* ***(b)*** *with absorbing material in the first 50% of the array.*

Bougdah *et al* [34] carried out a laboratory investigation of the possible noise-reduction properties of rib-like structures on the ground. They outlined the acoustic behaviour of rib-like structures and also outlined the mechanisms by which attenuation could be achieved. It was found that at lower frequencies, the generation of surface waves negated the attenuation properties of such a surface, as expected although this was not investigated further. It was further outlined that other mechanisms may impact the attenuation properties such as the potential for destructive interference between diffracted waves, interference effects in

between the grooves and effects due to quarter-wavelength resonances in the wells between the grooves. The idea of using quarter-wave resonators for noise attenuation has been investigated by Field and Fricke [35] who outlined the attenuation potential for quarter-wave resonators for ventilation systems. Using the theory of Ingard [36], it was stated that the open end of a quarter-wave resonator can be considered a pressure-release surface relative to the surrounding medium and that for cavities with a low internal resistance, it will act as a sound absorber [37]. Whilst useful for sound absorption, the possibility of the enhancement of signals using quarter-wavelength resonators has not been as thoroughly investigated. Berry *et al* [38] studied pulse propagation over a periodic array of cylinders using Multiple Scattering Theory (MST). The time-domain response exhibited wave-trains that followed the arrival of the main pulse. It was found that, for sufficiently small spacings, the peaks in the frequency spectra of the wave-trains correspond to frequencies associated with quarter-wavelength resonances in between the gaps between the cylinders. Furthermore, he found that as the gap is increased to sufficiently large spacings, the peaks in the spectra corresponded to Bragg frequencies.

2.5 Ultrasonic Propagation Over Roughness

Experiments carried out by Beadle *et al* [39] have explored the generation of Acoustic Surface Waves (ASW) over compound gratings at ultrasonic frequencies. Although at a much higher frequency range than that studied in this project, it was found that ‘end effects’ play a large role in the generation of surface waves over gratings. The cavities are thought to be excited on resonance and end effects occur at the cavity openings. These end effects couple over the surface in the form of an ASW. Their research is more concerned with the development of Surface Acoustic Wave (SAW) devices however it still gives an interesting

insight into the formation of the sound field over corrugated or strip-like surfaces. Tayong *et al* [40] investigated the holes interaction effect (HIE) of air-cavity backed micro perforated plates and the effect on their absorption coefficient. It was shown that for small spacings, the interaction of the sound field in neighbouring holes could not be ignored when determining the acoustical properties of such plates. This implies that for closely packed roughness elements, there will be interaction of the sound field generated in neighbouring cavities.

2.6 Summary

The existence of acoustic surface waves generated over surfaces with a 'spring-like' reactance has been confirmed through careful experimentation and simulation. The fact that the surface wave has a magnitude that decreases exponentially with height above the surface as well as having a phase speed slower than that in air has been widely noted in literature – both theoretically and empirically. Surface waves as a result of point-to-point propagation over reactive surfaces are a nuisance in noise control using porous and rough surfaces and the resulting ground effects, since they provide unwanted amplification at certain frequencies. However, passive amplification of audio-frequencies using surface waves generated over surfaces with periodic roughness is achievable. Further to this, other potential signal-enhancing mechanisms such as finite-width effects and resonances have been reported. However, the design of surfaces to achieve frequency-selective amplification and in-depth study into the total sound field at audio frequencies is not reported in any detail.

This aim of this project is to utilise the generation of surface waves to amplify acoustic signals in order to improve the performance of remote acoustic and seismic sensors. A detailed study of the sound field over surfaces with periodic roughness is carried out in order to determine how surface waves are generated over such surfaces and to look at the evolution of the entire sound field over such surfaces.

Chapter 3

Sound Propagation Models

3.1 Introduction

In this chapter, different ways of modelling sound propagation and surface wave generation over rough surfaces have been studied. Models aid experiments since, first, they allow us to compare experimental data with theoretical predictions based on a given model and, secondly, models validated in this way allow us to expand the parameters for a scaled experiment to a realistic scale which otherwise may be too difficult or time consuming to do. As well as simulating the detailed topography of the rough surface using the Boundary Element Method, this chapter will describe possibilities for modelling the rough surface as an effective impedance plane which can significantly reduce the computational time. The models outlined in this chapter include the Boundary Element Method (BEM), a Time-Domain BEM model, the impedance for a comb-like layer on a hard surface and the slit-pore impedance model.

3.2 Boundary Element Method (BEM)

The Boundary Element Method (BEM) is a numerical computational method derived from discretisation of a boundary integral equation in a way that is mathematically equivalent to the original partial differential equation [41]. The BEM consists of a boundary integral equation that is defined on the boundary of the domain of interest and relates the boundary solution to the solution at points within the specified domain. Through the implementation of

boundary conditions, the boundary integral equation can be solved so that the sound field can be found at any point within a domain.

The BEM has an advantage over more widely used techniques (such as Finite Element Analysis) since it requires only the boundary to be discretised whereas FEA requires the whole domain of the partial differential equation to be discretised. Furthermore, the equation governing an infinite domain can be reduced to an equation over a finite boundary. This reduces the computational time and significantly simplifies the problem.

In the case of a rough surface, the topography of the surface of interest can easily be defined – especially in the case of surfaces with periodic roughness. The BEM allows for simple numerical computation of the sound field over rough surfaces and allows to look at the various effects the surface has on the sound field at a receiver.

3.2.1 Acoustic Boundary Conditions

The acoustic field in any domain is governed by the linear wave equation,

$$\nabla^2 \psi(\mathbf{r},t) = \frac{1}{c^2}\frac{\partial^2}{\partial t^2}\psi(\mathbf{r},t) \tag{0.29}$$

where $\psi(\mathbf{r},t)$ is the scalar time-dependent velocity potential, c is the sound velocity and $\mathbf{r}$ and t are the spatial and time variables respectively. This is related to the time-dependent particle velocity by,

$$V(\mathbf{r},t) = \nabla\psi(\mathbf{r},t) \tag{0.30}$$

Since only the periodic solutions to the wave equation are considered, the velocity potential can be reduced to a sum of the real components of the potential in order to isolate the time-dependence,

$$\psi(\mathbf{r},t) = \mathrm{Re}\,\psi(\mathbf{r})e^{-i\omega t} \tag{0.31}$$

By substituting 3.3 into 3.1, it is possible to reduce the linear wave equation to the form of the Helmholtz equation,

$$\nabla^2\psi(\mathbf{r})+k^2\psi(\mathbf{r})=0 \tag{0.32}$$

where $k^2=\frac{\omega^2}{c^2}$ is the wavenumber. Thus, the sound pressure at a point $\mathbf{r}$ in specified domain is related to the velocity potential by,

$$p(\mathbf{r})=i\omega\rho\psi(\mathbf{r}) \tag{0.33}$$

For a locally-reacting surface, the impedance boundary conditions on the acoustic potential and the velocity potential are given by,

$$\frac{\partial\phi(r)}{\partial n}-ik_0\beta(r)\phi(r)=0 \tag{0.34}$$

$$\frac{\partial p(r)}{\partial n}-ik_0\beta(r)p(r)=0 \tag{0.35}$$

Where $\frac{\partial}{\partial n}$ is the normal derivative denoting the rate of change of the potential in the direction perpendicular to the boundary and β is the surface admittance defined as the inverse of the impedance.

As well as the impedance condition, it is necessary to introduce an external condition so that the scattered and radiated waves are only outgoing and not incoming from infinity. This is known as the Sommerfeld condition and is defined as,

$$\lim_{r\to\infty} r^{\frac{1}{2}}\left(\frac{\partial\psi(\mathbf{r})}{\partial r}-ik_0\psi(\mathbf{r})\right)=0 \tag{0.36}$$

$$\lim_{r\to\infty} r\left(\frac{\partial\psi(\mathbf{r})}{\partial r}-ik_0\psi(\mathbf{r})\right)=0 \tag{0.37}$$

Equation 3.8 is the Sommerfeld radiation condition in two dimensions while equation 3.9 is the condition in three dimensions.

3.2.2 Numerical Derivation

The BEM requires the transformation of the Helmholtz equation into a boundary integral equation and the use of a defined Green's function to obtain a solution. Developed in the 1830s by George Green, Green's functions allow for complicated ordinary differential equations to be solved by imposing a forcing term on the system and summing the individual response solutions. In the acoustic case, the Green's function must satisfy the Helmholtz wave equation. For an infinitely long line source radiating cylindrical waves into a fluid medium, the Green's function for a flat impedance surface (i.e. without roughness) is given by [42] in the x-z plane,

$$G_F\left(\mathbf{r},\mathbf{r}_0\right)=-\frac{i}{4}\left[H_0^{(1)}\left(k\left|\mathbf{r}_0-\mathbf{r}\right|\right)+H_0^{(1)}\left(k\left|\mathbf{r}_0^{'}-\mathbf{r}\right|\right)\right]+P_\beta\left(\mathbf{r},\mathbf{r}_0\right) \tag{0.38}$$

where,

$$P_\beta\left(\mathbf{r},\mathbf{r}_0\right)=\frac{i\beta}{2\pi}\int_{-\infty}^{\infty}\frac{e^{ik\left[\left(z+z_0\right)\sqrt{1-s^2}-\left(x-x_0\right)s\right]}}{\sqrt{1-s}\left(\sqrt{1-s^2}-\beta\right)}ds \qquad \mathrm{Re}\left(\beta\right)>0 \tag{0.39}$$

The function $H_0^{(1)}\left(\ \right)$ is the Hankel function of the first kind. In 3.10, the terms $\mathbf{r}$, $\mathbf{r}_0$ and $\mathbf{r}_0^{'}$ are the receiver, source and image source positions respectively and β is the normalised surface admittance and in 3.11 s is the position on the surface ds. The image source arises as a result of the reflected sound path from the ground surface. The function P_β represents the

contribution from the ground wave. If the source and the receiver positions align (i.e if $\mathbf{r}_0 - \mathbf{r}$ is small), the small argument approximations of the Hankel function may be used in the numerical integration, reducing the boundary integral equation to that of a line integral where the Green's function represents the sound field in the absence of scattering elements [32].

In the case of a line source producing sound above a two dimensional impedance plane bounded by a region D, it is possible to define a Green's function for the sound field at any distance r and height z above the impedance plane. In boundary integral form, the sound field is defined as,

$$\varepsilon\psi\left(r,z\right) = G\left(\mathbf{r},\mathbf{r}_0\right) - \left\{\int_S G\left(\mathbf{r},\mathbf{r}_s\right)\frac{\partial\psi\left(r_s,z_s\right)}{\partial\mathbf{n}\left(\mathbf{r}_s\right)} - \psi\left(r_s,z_s\right)\frac{\partial G\left(\mathbf{r},\mathbf{r}_s\right)}{\partial\mathbf{n}\left(\mathbf{r}_s\right)}\right\} ds \qquad (0.40)$$

In the above expression, ε is a dimensionless parameter that depends on the receiver's position relative to the domain. Table 3.1 shows the values of ε for a given receiver position. The Green's function $G\left(\mathbf{r},\mathbf{r}_0\right)$ is the Green's function solution to the wave equation for the sound field in the domain in the absence of scattering elements. The term $\mathbf{r}_s$ is the position vector of the boundary element ds and $\mathbf{n}$ is the unit normal vector to ds.

Receiver position relative to the domain, D	ε
Inside the medium	1
On the flat boundary	0.5
At the edges	Ω/2*

Table 3. 1 *Values of ε for various receiver positions within the domain. * Ω is the solid angle.*

Equation 3.12 is the boundary integral equation for the acoustic field potential in the presence of a non-uniform impedance boundary in the x-z plane. The integral allows for the calculation of the contribution from scattering elements on the total sound field over the boundary. The BEM then solves the set of integral equations numerically to give the total sound field within the medium.

It is useful to simplify the problem further by introducing the surface admittance to the integral equation. This allows for calculation of the total sound field in the presence of scattering elements with finite impedance or a ground surface with finite impedance. It is obtained by applying the impedance boundary condition, given by equation 3.6, to equation 3.12 to obtain,

$$\varepsilon\psi\left(r,z\right)=G\left(\mathbf{r},\mathbf{r}_0\right)-\int_S\psi\left(r_s,z_s\right)\left[ik_0\beta G\left(\mathbf{r},\mathbf{r}_s\right)-\frac{\partial G\left(\mathbf{r},\mathbf{r}_s\right)}{\partial\mathbf{n}\left(\mathbf{r}_s\right)}\right]ds \tag{0.41}$$

The above equation allows the BEM to calculation the total sound field above ground surfaces with multiple impedance discontinuities.

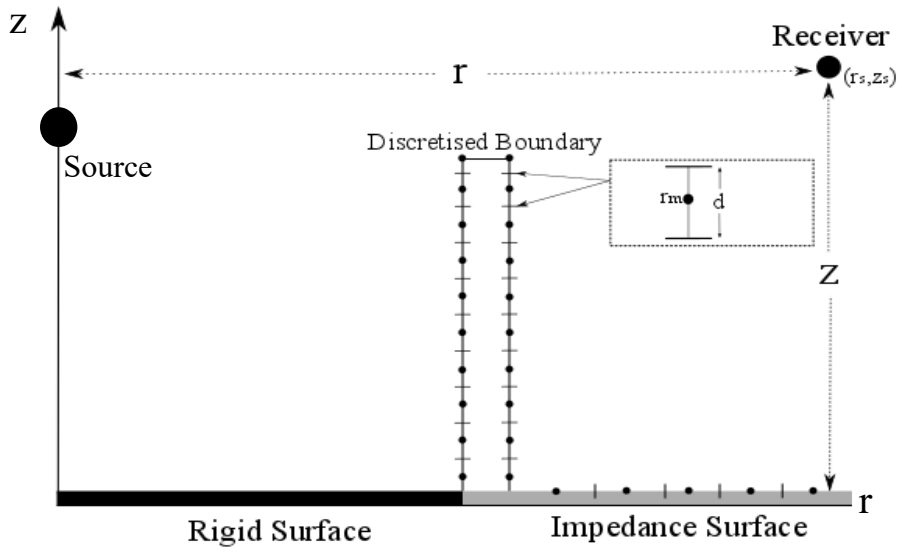

Figure 3. 1 *A 2D schematic of a rectangular roughness element which has been discretised into m elements by a small distance d, on the boundary between a rigid surface and a discretised impedance surface consisting of m elements.*

Consider a line source producing cylindrical waves within a domain D on a ground surface made up of an acoustically rigid surface, i.e $\beta = 0$, and an impedance ground surface with a finite admittance β . Equation 3.13 can be solved numerically for the total sound field over such a surface at an arbitrarily chosen receiver position at a distance r_s from the source and a height z_s from the ground surface. The roughness element and the impedance surface are discretised into m elements so that equation 3.13 will yield a set of M linear equations. This is done numerically using the quadrature method which allows for the discretisation of the boundary integral equation into a set of simpler, linear equations [43].

Each discretised element is separated by a distance d and centred at a point r_m where $m = 1,2,3...$ so that the integration is carried out between the limits of $-d/2$ and $d/2$.

Thus, equation 3.13 may be re-written as,

$$\int_S \psi\left(r_s, z_s\right)\left[ik_0\beta G\left(\mathbf{r},\mathbf{r}_s\right) - \frac{\partial G\left(\mathbf{r},\mathbf{r}_s\right)}{\partial \mathbf{n}\left(\mathbf{r}_s\right)}\right]ds = \sum_{m=1}^{M}\psi\left(r_m, z_m\right)\int_{r_m-d/2}^{r_m+d/2}\left[ik_0\beta G\left(\mathbf{r},\mathbf{r}_s\right) - \frac{\partial G\left(\mathbf{r},\mathbf{r}_s\right)}{\partial \mathbf{n}\left(\mathbf{r}_s\right)}\right]ds$$

(0.42)

This equation can be simplified by letting,

$$\Lambda\left(\mathbf{r},\mathbf{r}_s\right) = \int_{r_m-d/2}^{r_m+d/2}\left[ik_0\beta G\left(\mathbf{r},\mathbf{r}_s\right) - \frac{\partial G\left(\mathbf{r},\mathbf{r}_s\right)}{\partial \mathbf{n}\left(\mathbf{r}_s\right)}\right]ds \tag{0.43}$$

So that,

$$\varepsilon\psi\left(\mathbf{r}\right) = G\left(\mathbf{r},\mathbf{r}_0\right) - \sum_{m=1}^{M}\psi\left(\mathbf{r}_m\right)\Lambda\left(\mathbf{r},\mathbf{r}_m\right) \tag{0.44}$$

Equation 3.16 is the expression to be solved numerically. This allows us to calculate the sound field at every point along a boundary and integrate over all the contributions to obtain a total field solution over a given surface.

The BEM used throughout this research has been developed by Taherzadeh *et al* [42]. This program, written in FORTRAN, has the benefit of not requiring discretisation of the surface since it is possible to simply define the impedance parameters of that surface instead and account for the ground reflection in the Greens function. As a result, the computational time required is significantly reduced. BEM assumes that the roughness is small compared to the wavelength of the incident sound, at a lower limit of around 0.01λ [30]. It fails, however, to take into account viscous and thermal interactions at the boundary walls when the gap between strips is small. This means it is useful for studying the effects of topography on surface wave generation and the total sound field detected at the receiver.

3.2.3 BEM Simulation Procedure

The program reads in the input parameters as a text file. This process has been automated via a MATLAB script which allows for easy generation of the necessary input file.
First, the impedance model is defined by a number corresponding to the impedance model required. Throughout this project, the hard-backed slit-pore layer impedance model has been used (corresponding to a number 3).

The roughness elements are defined by outlining the x-y-coordinates of each node and meshing the necessary nodes together. In the input file, a 1 meshes two nodes together whilst a 0 leaves them unmeshed. The meshing of each node allows for the edges of the roughness elements to be defined. For long strip arrays, this process can become laborious and time-consuming and so a for-loop has been set up within the MATLAB script. The thickness, gap and height of each strip element is defined prior to the loop. The number of strips to be

generated is the variable input parameter in the for-loop. The series of nodes and meshing parameters can then be defined within the for-loop as:

$$\begin{aligned} &x(j) = start; y(j) = 0.0; z(j) = 1; \\ &x(j+1) = start; y(j+1) = height; z(j+1) = 1; \\ &x(j+2) = start + thick; y(j+2) = height; z(j+2) = 1; \\ &x(j+3) = start + thick; y(j+3) = 0.0; z(j+3) = 0; \end{aligned} \tag{0.45}$$

In 3.17, the term $start$ is the x-coordinate of the first node. The argument j is the element within the array of nodes and so once each loop is complete for each strip, the script moves onto the next. The term $z(\ )$ is the meshing parameter. The above will output an array of nodes for which the slit-pore impedance parameters can be defined for each strip. For the case of aluminium strips, a flow resistivity of 5,000,000 Pa s m^4 and a porosity of 0.01 have been chosen so the strips are simulated as acoustically rigid.

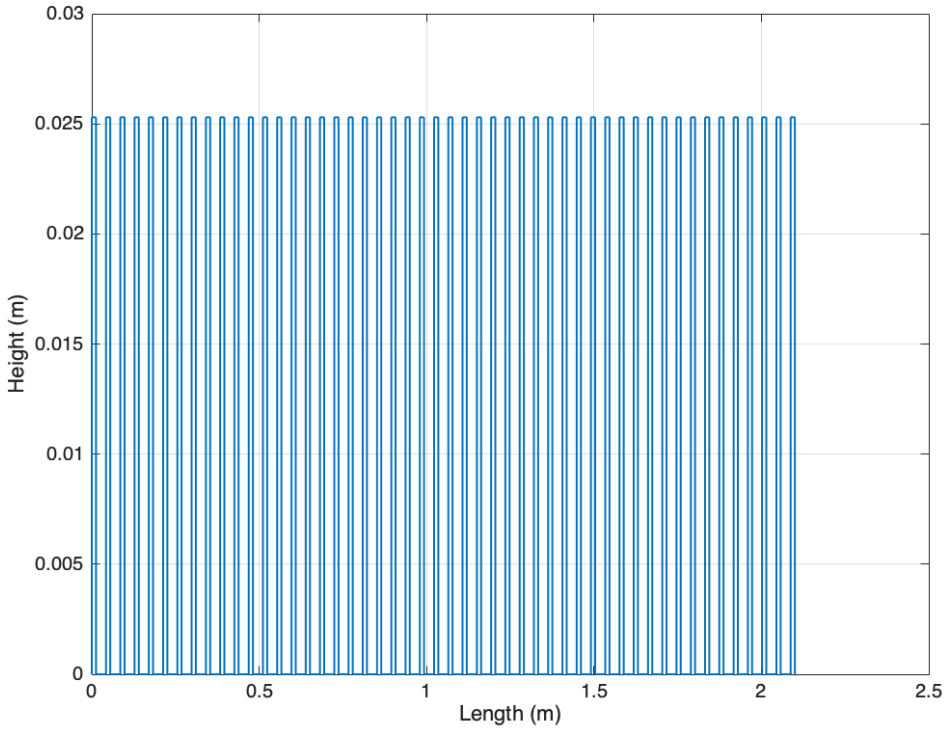

Figure 3. 2 *An example of the topography output file from the MATLAB script.*

The x-y coordinates of the source and receiver can then be defined. If necessary, up 10 sources and receivers can be input per simulation.

As mentioned, this version of the BEM is preferable since it does not require the discretisation of the ground surface on which the strips are situated; it simply requires the definition of slit-pore impedance parameters. Again, a flow resistivity of 5,000,000 Pa s m^4 and a porosity of 0.01 are chosen since the strips are placed on an acoustically rigid surface. The discretisation of the edges of the strips in the meshing process introduces potential error associated with the size of each meshed element. It has been found by multiple practitioners [30] that a minimum mesh size of 1/10 of the maximum wavelength of the free-field sound is required for sufficiently accurate results.

Finally, the frequency range of interest must be defined, and the numerical calculation must be carried out for at least 6 frequency points per third-octave-band between the minimum and maximum frequency. This is chosen to give a mean third-octave band and is preferable to using centre frequency values since these values can introduce numerical instabilities at some frequencies. The resulting outputs of this BEM is text files containing excess attenuation and the complex pressure of the total sound field over the surface.

3.2.4 Contour Boundary Element Method (ContourBEM)

As mentioned in the previous section, the BEM used throughout this project outputs excess attenuation and complex pressure as a function of frequency for a frequency ranged defined in the input file. A second, similar version of this BEM program has been designed to output the total sound field and the excess attenuation for a single frequency over a surface of

interest. This allows for the visualisation of the sound field at any frequency of interest through the generation of contour plots or pressure maps.

A grid of receivers is generated as a text file which are equally spaced in both the x-direction and y-direction. The script allows for up to 10,000 receivers. The BEM program then calculates the sound pressure at every receiver position at any specified frequency. This allows for the visualisation of the sound field at the surface wave frequency and any other frequency of interest.

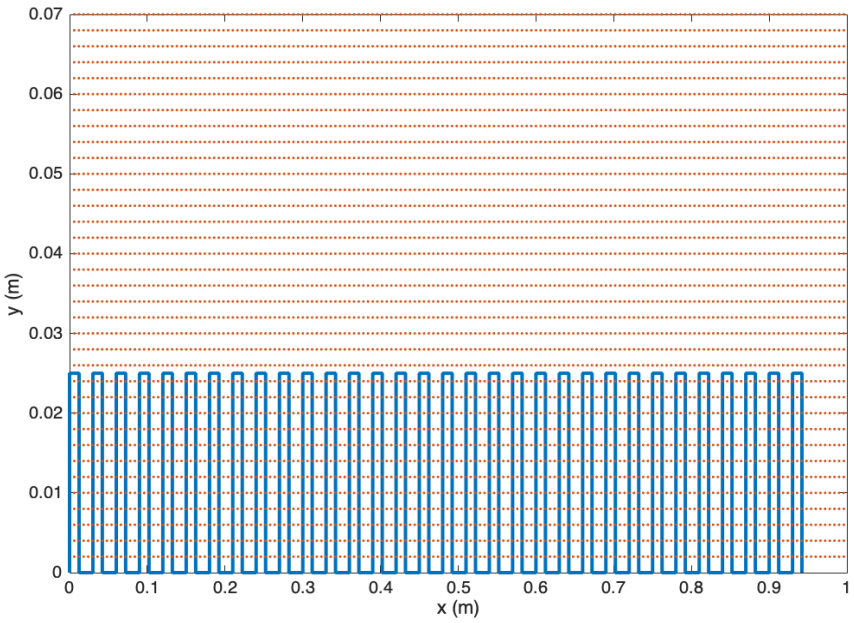

Figure 3. 3 *An example of the input geometry for ContourBEM with a grid of receivers indicated by the red dots.*

3.3 Time-Domain Boundary Element Method (TDBEM)

A surface wave generated over a rough surface has a phase speed slower than that of sound in air so if the source – receiver separation is large enough will appear as a separate arrival from the direct and reflected contributions in the time domain. Therefore, it is convenient to study

them in the time-domain as well as the frequency-domain and a Time-Domain BEM Method (TDBEM) has been developed.

3.3.1 The Fast Fourier Transform (FFT)

The source spectrum is obtained by calculating the Fast Fourier Transform (FFT) of a given source signal. This method has a long history but was popularised by Cooley and Tukey [44]. The Discrete Fourier Transform (DFT) provides a way of computing the Fourier transform for finite sets of data such as signals whose *N* points known at instants separated by a time, *T* [43]. The Fourier transform of the original signal will be,

$$F\left(i\omega\right)=\int_{-\infty}^{\infty}f\left(t\right)e^{-i\omega t}dt \tag{0.46}$$

where $F\left(i\omega\right)$ is the Fourier transform. The argument has been chosen as such since the DFT is a complex-valued function of frequency. The function $f\left(t\right)$ is the input time signal containing *N* samples denoted by $f\left[0\right],f\left[1\right],f\left[2\right],...,f\left[k\right],...,f\left[N-1\right]$. It is convenient in this case to regard each sample, denoted by $f\left[k\right]$, as an impulse having an area given by $f\left[k\right]$. Thus, the integrand becomes,

$$\begin{aligned}F\left(i\omega\right)&=\int_{0}^{\left(N-1\right)T}f\left(t\right)e^{-i\omega t}dt\\&=f\left[0\right]+f\left[1\right]e^{-i\omega T}+...+f\left[k\right]e^{-i\omega kT}+...+f\left(N-1\right)e^{-i\omega\left(N-1\right)T}\end{aligned} \tag{0.47}$$

$$F\left(i\omega\right)=\sum_{k=0}^{N-1}f\left[k\right]e^{-i\omega kT}$$

Like the continuous Fourier transform (see 3.1), the DFT treats the input signal as if it were periodic, hence the choice of limits in the integral in 3.2. As a result of this, the DFT is evaluated for the fundamental frequency of the signal as well as its harmonics corresponding

to the set of frequencies given by $\omega = 0, \frac{2\pi}{NT}, \frac{4\pi}{NT}, ..., \frac{2\pi}{NT} n, ..., \frac{2\pi}{NT}\left(N-1\right)$, which in general is,

$$F\left[n\right] = \sum_{k=0}^{N-1} f\left[k\right] e^{-i\frac{2\pi}{N}nk} \qquad (0.48)$$
$$n = 0 : N-1$$

Equation 3.3 is the DFT of a sequence $f\left[k\right]$ between $n = 0$ and $n = N-1$.

Discretisation of signals is necessary when digital analysis techniques are used to analyse continuous signals. The FFT takes advantage of the fact that the calculations of the coefficients of the DFT can be conducted iteratively. If the time series, obtained through discretisation of the continuous waveform, consists of $N = 2^n$ samples then the number of arithmetic operations required to evaluate the N DFT coefficients will be $2nN = 2N\log_2\left(N\right)$ [45]. This is significantly quicker than calculation of DFT coefficients by the usual DFT method detailed above. The FFT has been used throughout this research to digitally obtain the frequency spectra of discretised time-domain data.

3.3.2 Blackman-Harris Window

The periodic and finite nature of the FFT results in the assumption that the time-series and its resulting spectrum have endpoints that are connected together in a circular mathematical topology. When the time-series has an integer number of periods then this assumption is valid. However, when this is not the case, when the number of periods is not an integer, the endpoints of the signal become discontinuous and can result in high frequency contributions that aren't present in the original signal. This is known as spectral leakage and can appear as energy at one frequency leaking into another.

Windowing a signal reduces this unwanted contribution by multiplying the time-series by a finite-length window function with an amplitude that varies smoothly and gradually towards zero at the endpoints. This reduces any spectral leakage between frequencies.

There are many types of window functions. The simplest is the rectangular window defined by,

$$w(n) = \begin{cases} 1 & 0 \le n \le N-1 \\ 0 & otherwise \end{cases} \tag{0.49}$$

This allows for the signal to be zero except for a given interval where the signal is multiplied by one. There are less windows with less abrupt truncation available. The window used throughout this project is the Blackman-Harris window. This tapers the window smoothly to zero at each end of the windowed portion of the signal. The definition of the 4-term Blackman-Harris window is,

$$\begin{aligned} &w(n) = a_0 - a_1 \cos\left(\frac{2\pi n}{N-1}\right) + a_2 \cos\left(\frac{4\pi n}{N-1}\right) - a_3 \cos\left(\frac{6\pi n}{N-1}\right), 0 \le n \le N-1 \\ &a_0 = 0.35875 \\ &a_2 = 0.48829 \\ &a_3 = 0.14128 \end{aligned} \tag{0.50}$$

This choice of window throughout is justified since it provides a significant reduction in the side lobes in the FFT of a time-signal, although this is at the expense of a wider main lobe and thus a wider transition at the discontinuity [46]. For many pulse signals, it is useful to use a half Blackman-Harris window which starts at a maximum of 1 and tapers down gradually to zero. This means less of the signal is lost through the windowing process.

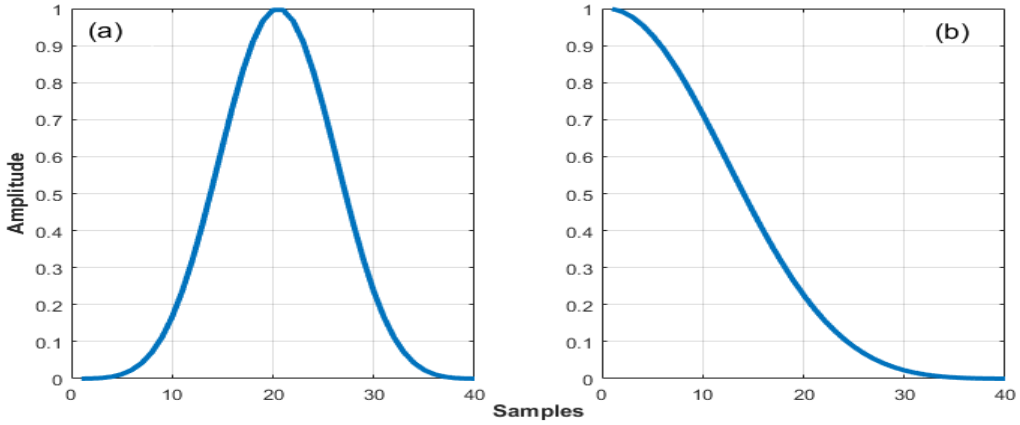

Figure 3. 4 (a) *A 40-point Blackman-Harris window* ***(b)*** *A 40-point half Blackman-Harris window.*

3.3.3 Time-Domain Boundary Element Method Program (TDBEM)

This program starts with a pulse as the source signal. If data is being used as opposed to a digitally generated mathematical pulse then the signal is windowed using a half Blackman-Harris window. The source spectrum is generated through the calculation of the FFT of the source signal. A high-pass and low-pass infinite impulse response (IIR) filter is applied to the signal so that the FFT is contained between the frequencies of interest arising from the geometry.

The response in the time domain $p(r,z,t)$ will be the Fourier integral of the product of the source function $S(\omega)$ and the transfer function $p(r,z,\omega)$. The transfer function is obtained from the output of the BEM simulation of the sound field generated over a rough surface or an impedance layer with rigid backing. The Fourier integral is given by,

$$p(r,z,t)=\frac{1}{2\pi}\int_{-f_{nyq}}^{f_{nyq}} S(\omega)p(r,z,\omega)e^{-i\omega t}d\omega \qquad (0.51)$$

where the maximum frequency f_{nyq} is half the sampling frequency, also known as the Nyquist frequency. The solution to the Helmholtz equation is conjugate symmetric. This means that the time-series satisfies the condition,

$$x(t) = \overline{x(-t)} \tag{0.52}$$

where $\overline{x(-t)}$ is the complex conjugate of the time-reversal of the signal $x(t)$. For the solution to the Helmholtz equation [47],

$$p(r,z,\omega) = \overline{p(r,z,-\omega)} \tag{0.53}$$

Since the source spectrum is obtained from zero frequency to half the sampling frequency, this allows for a full spectrum to be obtained since the complex conjugate can be added to the source spectrum to obtain the spectrum for the full frequency range from 0 to the sampling frequency. The details of this are presented in figure 3.5 below.

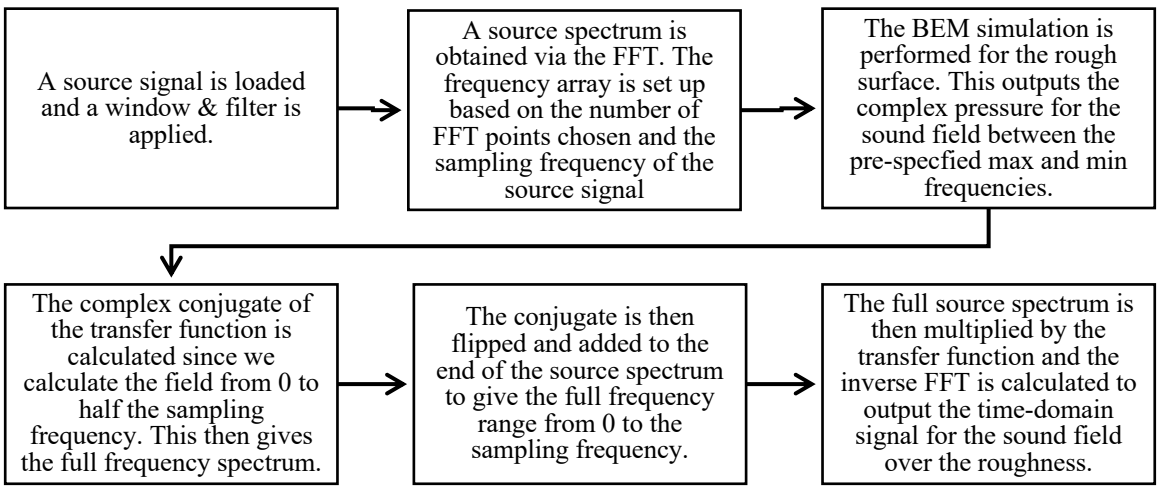

Figure 3. 5 *A flow diagram outlining the process of TDBEM.*

3.4 Impedance of a Hard-Backed Comb-Like Surface

In his 1958 paper [8], Brekhovskikh outlined the theoretical basis for a surface wave generated over a comb-like surface.

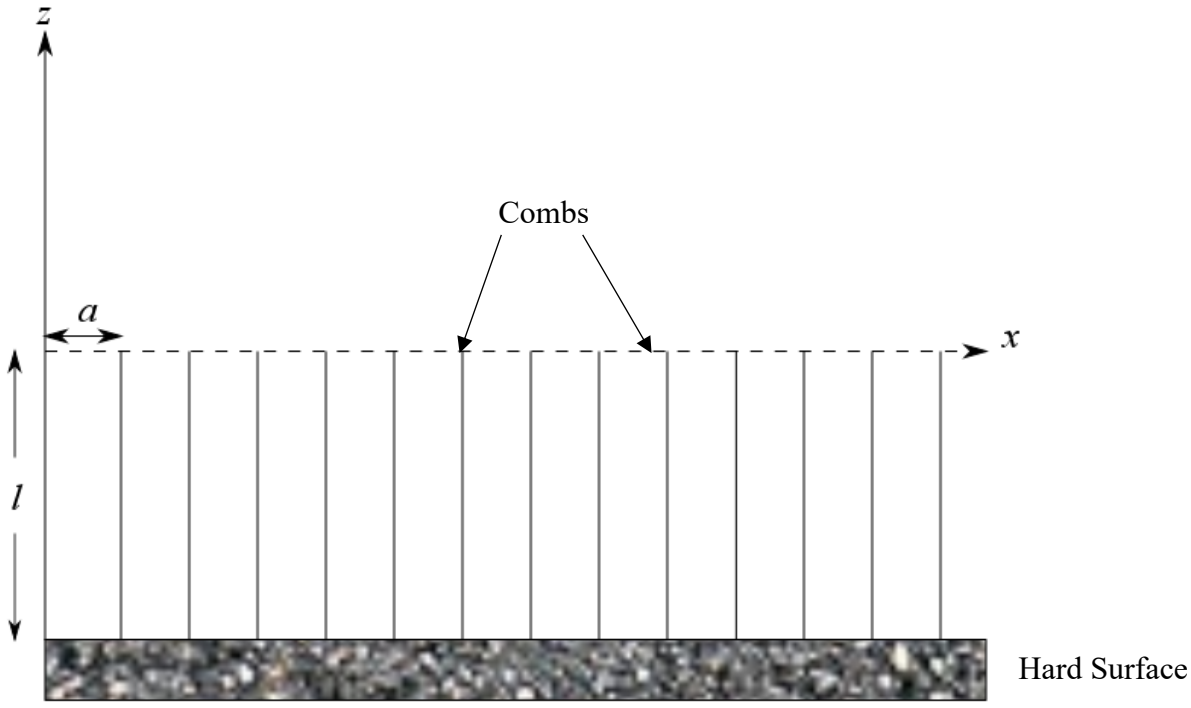

Figure 3. 6 *A comb-like surface on a hard surface where a is the gap between elements and l is the height of the elements from the ground layer.*

The surface wave equation can be written simply as,

$$p = p_0 e^{-\alpha z} e^{ihx} \tag{0.54}$$

where,

$$h = \sqrt{k^2 + \alpha^2} \tag{0.55}$$

In the above expression, k is the wavenumber and α is related to the attenuation. The first exponential factor in 3.26 indicates that the surface wave amplitude reduces exponentially with height above the surface z . For the surface, above it is assumed that,

$$a < l \tag{0.56}$$

$$ah < 1 \tag{0.57}$$

The condition in 3.29 states that the gap between the comb-like elements is significantly less than the wavelength of the sound travelling over it. In between the elements, there will be a standing wave generated with pressure p_1 at a point x' given by,

$$p_1 = \frac{\cos k\left(z + l\right)}{\cos kl} e^{ihx'} \tag{0.58}$$

At the ground layer $z = 0$, continuity of pressure and the normal component of velocity has been assumed,

$$p = p_1 \tag{0.59}$$

$$\frac{\partial p}{\partial z} = \frac{\partial p_1}{\partial z} \tag{0.60}$$

Furthermore, it is assumed that at $z = -l$,

$$\frac{\partial p}{\partial z} = 0 \tag{0.61}$$

From equations 3.26 and 3.29 and applying the condition 3.31, it can be shown that for comb-like surface on a hard backed layer,

$$\alpha = k \tanh kl \tag{0.62}$$

Now consider a surface where the boundary has a ‘spring-like’, elastic impedance given by,

$$Z = \frac{i\rho c}{\varsigma} \tag{0.63}$$

In the above expression, the term ς signifies a dimensionless elasticity factor or ‘pliability.’ If the impedance condition

$$Z = \frac{p}{u_z} \tag{0.64}$$

is satisfied at the ground layer $z = 0$, where u_z is the vertical particle velocity at the boundary given by,

$$u_z = -\frac{1}{i\omega\rho}\frac{\partial p}{\partial z} \tag{0.65}$$

From substitution of equation 3.27 into 3.37 and substitution of the result into 3.35, it is possible to show that,

$$\alpha = k\varsigma \tag{0.66}$$

where,

$$\varsigma = \tanh(kl) \tag{0.67}$$

Substitution of 3.39 into 3.35 yields,

$$Z = \rho c\left[i\coth(kl)\right] \tag{0.68}$$

The expression given by 3.40 is the purely reactive impedance of a comb-like surface on a hard-backed layer This signifies that the thin, comb-like surface can be represented as a thin layer of air with rigid backing but does not take into account the finite resistive component associated with such surfaces. The same expression will hold for the surface impedance of a thin hard-backed porous layer but ρc and k will be replaced by the characteristic impedance Z_c and the complex propagation constant k_c respectively,

$$Z = Z_c\left[i\coth(k_c L)\right] \tag{0.69}$$

The above provides further historical insight into the sound field above comb-like surfaces. However, as mentioned, these surfaces have a finite resistive component to the surface impedance which results in a more complex sound field above the surface.

3.5 Slit-Pore Model

Many impedance models have attempted to characterise the acoustic nature of outdoor ground surfaces. Initially, the nature of outdoor ground surfaces was over-simplified by the assumption that any ground of low porosity could be thought of as acoustically rigid and any higher porosity ground surfaces could be considered acoustically soft [48]. In actuality, the ground effect due to an outdoor ground surface is affected by many different variables and so a more accurate model that takes these into account was required. Many impedance models take into account parameters such as pore shape factors, characteristic lengths and pore size distributions which are not easily determined for outdoor ground surfaces [49]. It is therefore desirable to simplify these models to contain variables that are more readily determined for outdoor ground surfaces.

A pore-based microstructural model has been developed which gives a simple impedance model based primarily on the porosity, Ω, and flow resistivity, R_s of the medium [2]. The porosity is defined as the ratio between the empty space within a material to its total volume and the flow resistivity is a measure of the resistance per unit length experience by the air particles within the material.

The two parameters which characterise such a medium are a complex density given by,

$$\rho(\omega) = \frac{\rho_0}{G(\lambda)} \tag{0.70}$$

and a complex compressibility given by,

$$C(\omega) = (\gamma P_0)^{-1}\left[\gamma - (\gamma - 1)G\left(\lambda\sqrt{N_{PR}}\right)\right] \tag{0.71}$$

where $(\gamma P_0)^{-1} = (\rho_0 c_0^2)^{-1}$ is the adiabatic compressibility of the air within the pores, γ is the ratio of specific heat capacities of air at constant pressure and volume and N_{PR} is the Prandtl

number defined as the ratio of the viscous and thermal diffusion rates. The complex density in 3.1 characterises the viscous effects within the pores whilst the complex compressibility contains the thermal effects. For slit-like pores,

$$G(\lambda) = 1 - \tanh\left(\lambda\sqrt{i}\right) / \left(\lambda\sqrt{i}\right) \tag{0.72}$$

The parameter λ is dimensionless and can be calculated for different pore shapes. For parallel slit-like pores,

$$\lambda = s_B \left(\frac{3\rho_0 \omega T}{hR_s} \right)^{1/2} \tag{0.73}$$

where, T is the tortuosity defined as the square of the increase in path length per unit thickness of a material due to deviations of the steady-flow path from a straight line. If the frequency of the sound wave is high enough, the velocity of the sound through the pores becomes non-dispersive due to the effect of viscous drag within the pores becoming negligible.

Once the complex compressibility and complex density are known, it is possible to calculate the complex propagation constant,

$$k(\omega) = \omega\left[T\rho(\omega)C(\omega)\right]^{1/2} \tag{0.74}$$

The characteristic impedance of the bulk material is given by,

$$Z_c(\omega) = (\rho_0 c_0)^{-1}\left[\left(\frac{T}{\Omega^2}\right)\frac{\rho(\omega)}{C(\omega)}\right]^{1/2} \tag{0.75}$$

It has been shown [33] that the dependence of the properties of a rigid-porous medium are affected very little by the assumed pore shape. The hyperbolic cotangent permits easier computation since it is required in calculation of the impedance of a hard-backed layer. In 3.47, the term s_B is a frequency-independent pore shape parameter which has a value of 1 for

slits. The choice of a specific pore shape simplifies the model since calculation of varying pore shape factors is no longer required.

The slit-pore model is useful since a rough comb-like surface can be modelled simply as a rigid slit-pore layer of a certain depth with a porosity dictated by the thickness, w of the roughness elements and the gap, a between them, and a flow resistivity, R_s which depends on the porosity, Ω and the gap between elements. These can be calculated using,

$$\Omega = \frac{a}{a+w} \tag{0.76}$$

$$R_s = \frac{12\mu}{\Omega a^2} \tag{0.77}$$

where μ is the dynamic viscosity of air which has a value of 1.81×10^{-5} Pa s $^{-4}$.

The limitations of modelling the rough surface as a rigid slit-pore layer are exposed as the gap between roughness elements is increased. The slit-pore model breaks down when the spacing between roughness elements approaches 50% of the layer depth [32] since the effects of viscous and thermal dissipation within the gaps is reduced. Roughness with larger spacing tends to behave as a rough surface after this limit. However, below this limit, losses occur within the pores due to viscous and thermal boundary layers. Thermal losses arise since heat is transferred into the walls due to temperature gradients within the air in the pores. A thin boundary layer occurs at the pore walls since a velocity gradient arises due to the fact that the air within the pore has zero velocity relative to the boundary. This results in viscous losses within the pores.

The models detailed above provide useful means of modelling sound propagation over periodically-rough surfaces. Brekhovskikh's method gives an idealised case for a purely reactive surface but fails to account for the finite resistive component that contributes to the total field generated over the surface.

The Boundary Element Method and slit-pore model are both effective for this purpose. The BEM allows for the modelling of the topographical nature of the surface and for the modelling of the effects of scattering on the total sound field over the surface. However, it fails to take into account the viscous and thermal interactions at the boundary walls when the gap between strips is small. The slit-pore model accounts for this and so can be used to investigate surface wave generation over the surface by modelling the strips as an effective impedance surface. It is these models that will be used alongside measurement as predicitons of results in chapters 5 and 6.

Chapter 4

Measurement Methods and Materials

4.1 Introduction

In this chapter, the data acquisition and processing methods as well as materials used will be discussed. The measurements undertaken include laboratory measurements under anechoic conditions.

Acoustic measurements require the conversion of a computer-generated digital signal into an analogue signal that can be output from the sound source. The input signals used under anechoic conditions include a Maximum Length Sequence impulse for measurements of excess attenuation and a Ricker pulse in order to view the response in the time-domain. The Maximum Length Sequence (MLS) pulse was chosen since it has pulse-like characteristics in the time-domain with a broadband frequency spectrum. Measurements were carried out with white noise as the source signal, however, it was found that there were significant reflected contributions from apparatus in the anechoic chamber which interfered with measurement results.

The response can then be measured at a receiver and converted back to a digital signal for processing and analysis. The conversion from digital to analogue and back involves a digital to analogue converter.

4.2 Input Signals

4.2.1 Maximum Length Sequence (MLS) Pulse

The MLS was developed by Schroeder [50] in 1979. It is a pseudo-random binary sequence consisting of an apparently random sequence of +1 and -1 and has a flat frequency spectrum for all frequencies up to the Nyquist frequency with the exception of the near-zero DC term. This makes it a computationally efficient method for extracting the impulse response of linear systems.

The most important feature of MLS signals is that the FFT has the same magnitude for all frequency components meaning the power spectrum is like that of a single, frequency-independent impulse. MLS signals are generated using linear feedback shift registers.

The quality and number of samples in one period, L , of MLS signals is dependent upon its period m and is given by,

$$L = 2^m - 1 \tag{0.78}$$

The higher the order, the greater the quality of the signal as a result of a better signal to noise ratio. However, a higher order signal produces a longer output signal and increases measurement time. Bashir [32] found that that, under anechoic conditions, an MLS sequence of order 16 offers a good compromise between measurement time and signal-to-noise ratio. Schroeder [50] found that for room-acoustical measurements below 10 kHz, a minimum sampling rate of 20 kHz is required. The sampling rate used throughout this study is 75 kHz which is the sampling rate of associated with the MLS signal extracted from the Maximum Length Sequence System Analyser (MLSSA). The operations of the MLSSA system were re-

written as a MATLAB script as an updated data acquisition system. This is described in section 4.3.

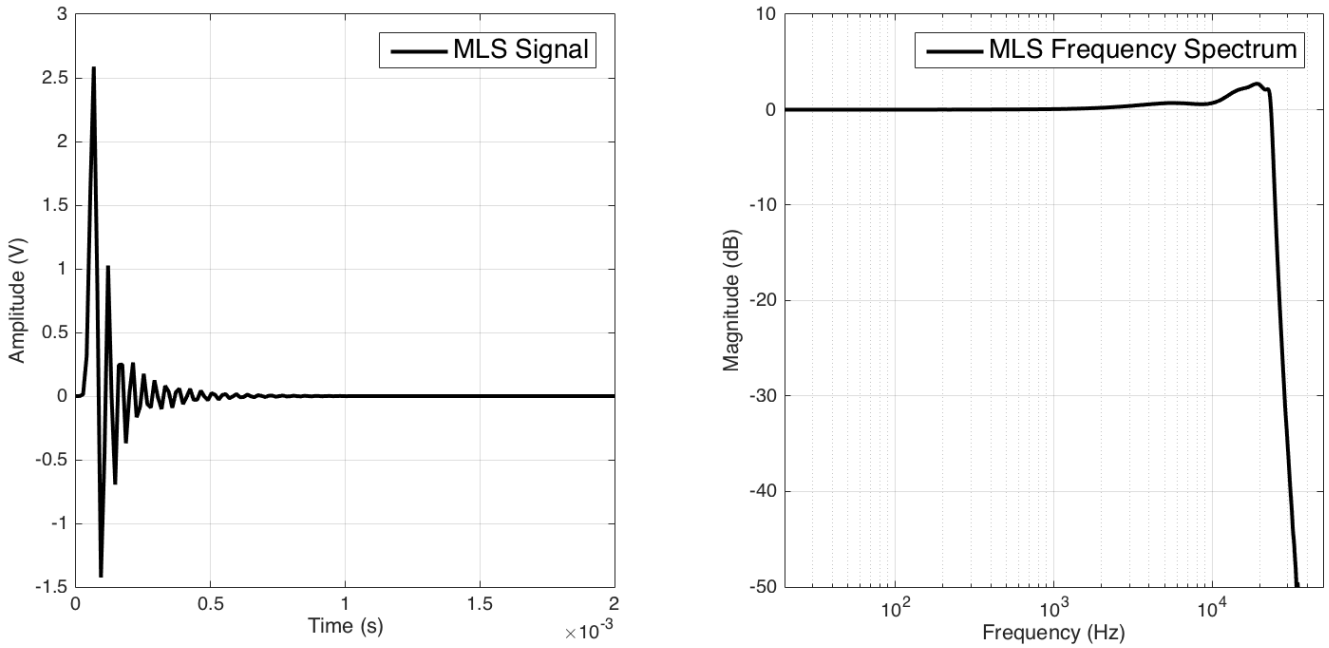

Figure 4. 1 *A MLS signal in the time-domain and its corresponding frequency spectrum.*

4.2.2 Ricker Pulse

Surface waves travel slower than sound in air. In order to study surface waves as later arrivals in the time-domain, a Ricker pulse is used. This is because the diaphragm of the speaker cannot support the generation of a narrow pulse and the MLS signal has a broad frequency spectrum. The Ricker pulse provides a good compromise where the centre frequency is centred somewhere around the surface wave maximum in the excess attenuation spectrum deduced from analysing the MLS signal.

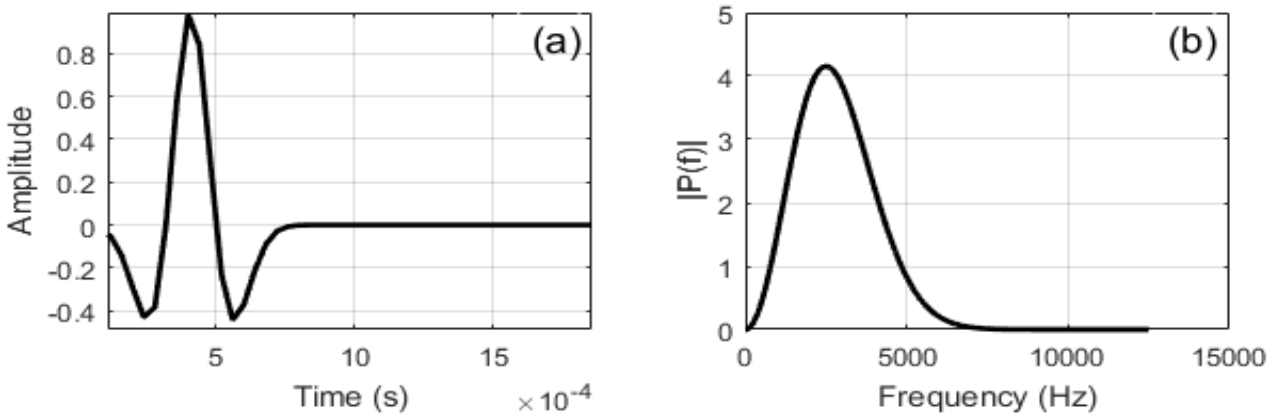

Figure 4. 2 (a) *A Ricker pulse centred at 2500 Hz.* ***(b)*** *Corresponding frequency spectrum calculated from a 4096-point FFT.*

Mathematically, the Ricker wavelet is defined as the negative normalised second derivative of a Gaussian function and is given by,

$$\psi(t) = \frac{2}{\sqrt{3\sigma}\pi^{1/4}}\left[1-\left(\frac{t}{\sigma}\right)^2\right]e^{-\frac{t^2}{2\sigma^2}} \tag{0.79}$$

4.3 Laboratory Measurement Setup

The measurements carried out throughout this project have been undertaken under anechoic conditions. The walls and floor are lined with polyurethane foam cones in order to minimise reflections. The anechoic chamber at The Open University has dimensions of 4.3 m x 4.3 m x 4.3 m and is designed to absorb any sound waves above 125 Hz. However, a grid floor is used as a supporting mechanism which could possibly introduce some unwanted reflections. The door to the chamber is a heavy-set and contains a rubber sealing around the perimeter which provides further acoustic insulation.

The roughness elements used throughout this project include periodically-spaced rectangular aluminium strips of dimensions 0.0126m x 0.0253m..

To minimise reflective contributions from the grid flooring, measurements are conducted over periodically rough surface placed on an acoustically rigid sheet of Medium Density Fibreboard (MDF). This allows for measurements of excess attenuation to be taken with respect to an acoustically rigid surface as opposed to the more traditional, yet slightly less practical, free field. Excess attenuation is defined as the spectrum of the ratio of the sound field over a given surface and the sound field in the absence of a ground surface, the free field. It can also be defined as extra attenuation introduced by factors other than the attenuation due to spherical spreading. Mathematically, excess attenuation, EA , can be calculated using,

$$EA = 20\log_{10}\left(\frac{P_{Total}}{P_{Free}}\right) \tag{0.80}$$

where P_{Total} is the total sound field over the surface of interest and P_{Free} is the free field. For the measurements taken over a surface with periodic roughness on an acoustically rigid surface,

$$EA = 20\log_{10}\left(\frac{P_{Total}}{P_{Rigid}}\right) \tag{0.81}$$

where P_{Rigid} is the sound field over the MDF in the absence of the rough surface.

For measurements of excess attenuation, a digital MLS signal was obtained from an older Maximum Length Sequence System Analyser (MLSSA) which was used to generate and process MLS signals. These signals were then read into a MATLAB script and converted to analogue signals via an NIDAQ-USB 6259 data acquisition system which allows for easy digital to analogue conversion. For measurements of time response, a Ricker pulse was

generated using a MATLAB function which uses the spread, σ of the pulse, related to the centre frequency f by,

$$\sigma = \frac{\sqrt{2}}{2\pi f} \tag{0.82}$$

and the time interval as an input. It was found that the sampling rate must be at least ten times the centre frequency for adequate sampling of the pulse. From the data acquisition system, the signal is fed through a Cambridge audio stereo amplifier. The gain was set high enough so that the microphone is able to pick up the signal but not so high so that the source enters non-linear region of acoustic generation. The amplifier was connected via Bayonet Neill-Concelmann (BNC) cables to an acoustic source. All the BNC cables are wrapped with foam so as to eradicate any noise introduced through the contact between the metal flooring and the metal BNC connectors.

The source used in the anechoic measurements is a Tannoy driver fitted with a 2m Perspex tube. The end of the tube acts as an impedance discontinuity and thus contributes reflections which can interfere with the arrival of the main pulse. The 2m tube used throughout the anechoic experiments ensures that any later arrivals are separated in time from the internal reflection contributions and thus any surface wave contribution can be easily distinguished. The Tannoy driver's output has a frequency range between 300Hz and 20,000Hz which is a suitable range for the audio frequency measurements of interest in this project.

The receiver used in the anechoic measurements was a Bruel & Kjaer (B&K) Type 4189-B-001 ½ -inch microphone. This is connected via a BNC cable to a B&K Type 5935 power supply and pre-amplifier. The gain on the amplifier was set to 30 dB which allowed for

clearer analysis. The signal was then re-routed back to the analogue to digital converter to be converted to a digital signal ready for analysis.

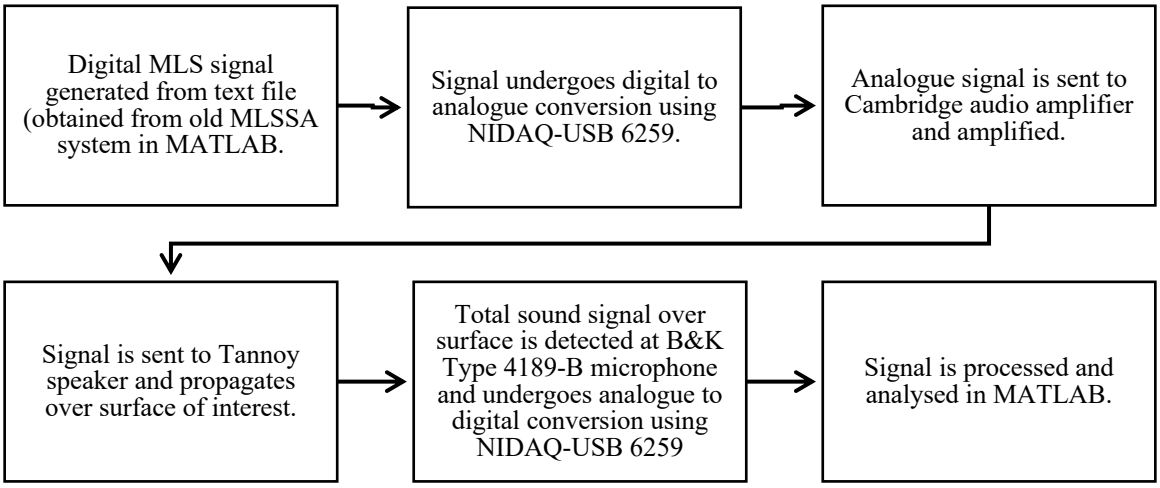

Figure 4. 3 *A flow diagram outlining the measurement process.*

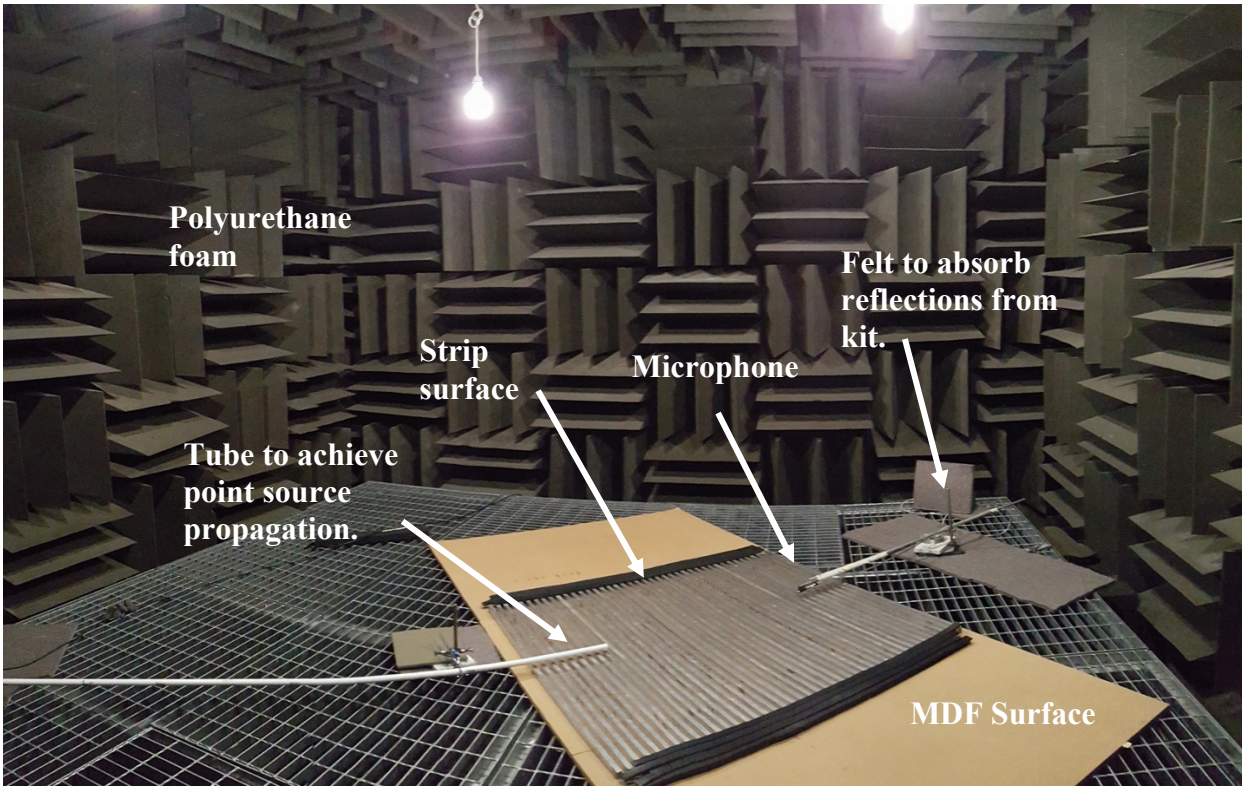

Figure 4. 4 *Measurement setup in the anechoic chamber*

4.4 Experimental Procedure

4.4.1 Measurements of Excess Attenuation

As mentioned in section 4.2, measurements of excess attenuation are obtained using an MLS signal and time-domain measurements are obtained using a Ricker pulse. A signal is digitally generated and passed through the digital to analogue converter to be output by the speaker.

First, the source and receiver are separated and raised to a desired height above the MDF board. For measurements of excess attenuation, a series of 10 pulses each 4000 points in length is input 15 times and the average is taken as the output. This was found to produce an adequate output whilst keeping the measurement time to a minimum. It also significantly reduced the signal-to-noise ratio.

Ideally, a free field measurement would be taken by removing all of the grids in the anechoic chamber and hanging a source and receiver high off the ground at the separation of interest. However as mentioned in section 4.3, this is time-consuming and impractical when varying source-receiver separations, Throughout this study, it is assumed that the incident sound is near grazing and so the ground effect minimum associated with reflection off the ground surface is at a much higher frequency than those of interest in this study, It is possible, therefore, to simply perform a measurement over an acoustically-rigid surface as a reference measurement. This data is then stored before the periodically-spaced roughness elements are then carefully placed on the board and a measurement taken of the total field over that surface. Once the reference measurement and total field are obtained, Equation 4.4 is used to calculate the excess attenuation spectrum. Ricker pulse measurements require the same procedure except only the time-domain data is used since the narrow-band nature of the Ricker pulse means it is unsuitable for measurements of excess attenuation. Once the surface

wave frequency is obtained from the excess attenuation spectrum, this is input as the centre frequency for the pulse. An average of 15 repetitions, each containing 5 pulses, produced a clear time response.

As mentioned previously, it is important that the gain is adjusted to a suitable level in order to ensure that the signal is detectable. It is also important not to overload the power supply.

Temperature readings are taken regularly in order to ensure stability within the chamber. A change in temperature results in a change in the sound speed which may introduce problems when trying to window the signal of interest. Moreover, the condition in the chamber can be considered stable since results do not differ depending on the time of day

4.4.2 Phase Gradient Method

Measurements of some surface wave properties are relatively simple. For example, the exponential decrease in amplitude with receiver height above the surface simply involves multiple measurements of excess attenuation at various receiver heights. As mentioned, one important property of surface waves is that they have a lower phase speed than that of sound in air. Thus, an important process in the identification of surface waves is measurements of phase speed over the surface.

The phase gradient method allows for determination of the surface wave phase speed over the surface. The height of the source and receiver is kept constant above the strip surface. The receiver is placed close to the source and moved away in small increments. This is done using a motorised tracker (originally designed for the precise movement of lasers) with a

microphone carefully attached to an extendable arm. This allows for precise movement of the laser to within with an error of ±1 mm.

Careful measurements of complex pressure are taken at every interval, via the calculation of the FFT, and saved. It is from this data that the unwrapped phase angle can be determined using the 'unwrap' function in MATLAB.

The unwrapped phase angle at a given frequency, varies linearly with receiver distance from the source with the gradient being the wavenumber, k at that frequency, f. From this, it is possible to determine the phase speed of the wave, v at any frequency of interest by simply using,

$$v = \frac{\omega}{k} \tag{0.83}$$

It is also possible to use this procedure in numerical calculations using BEM by simulating multiple receiver positions over the strip array and following the procedure outlined above using the output of complex pressure.

4.5 Analysis Procedure

First, it is important to remove any extraneous reflections. These occur due to reflection of the main pulse from the end of the tube and reflection from nearby surfaces, such as the power supply, for example. It is possible to remove some of these reflections by covering the reflective surfaces with sound absorbing material. When this is not possible, it is necessary to multiply the time-domain output by a windowing function. One challenge, however, is removing any interference from reflections without reducing the amplitude of any of the later

arrivals of interest, such as the surface wave. Therefore, the choice of window varies depending on the signal. A commonly used window is the rectangular window. However, according to the Fourier principle, a signal that is limited in the time-domain is unlimited in the frequency domain and vice versa. The abruptness of the rectangular window in the time-domain gives rise to the Gibbs' phenomenon in the frequency domain which means energy can appear as another feature or 'spike' in the frequency domain. Thus, a tapered window is preferable. For MLS input signals, a half Blackman-Harris window is sufficient in removing any reflections since it is fairly broadband. For the Ricker pulse, it is necessary to use a rectangular window that has been tapered at the end. This is because the frequency content of the Ricker pulse is much narrower and thus too small a window will reduce any interesting features that arise through the interaction of the total sound field with the surface.

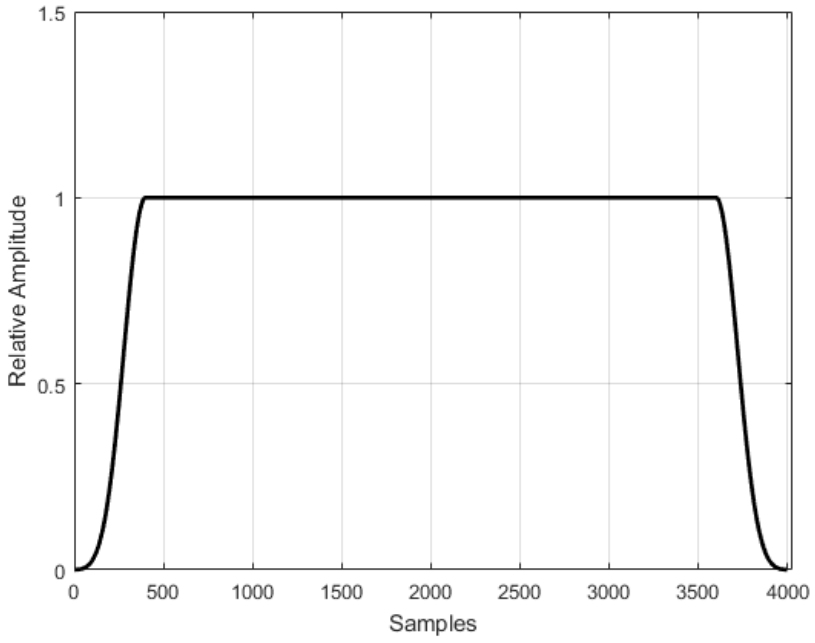

Figure 4. 5 *A 4000-point tapered Blackman-Harris window.*

The result of windowing is a cleaner excess attenuation spectrum. This allows for features in the excess attenuation spectrum to be more easily distinguished from any noise. For an

acoustically rigid surface, the enhancement due to constructive interference between the direct and reflected wave is 6 dB when a free-field measurement is taken. This corresponds to a doubling in the sound pressure and is the maximum enhancement achievable due to reflection off a hard surface. A surface wave is distinguishable in excess attenuation spectra as any feature above 6 dB. When a reference measurement is taken over a hard surface, the surface wave is distinguishable as any feature above 0 dB since the reference measurement is taken over the hard surface and total field measurement is taken following the insertion of the strips. The logarithm of the ratio of the two sound fields yields only effect of the strip surface which is any enhancement feature above 0 dB and any sound absorption below 0 dB. For convenience and consistency in comparison with results from simulation, 6 dB is added to the excess attenuation data since BEM outputs excess attenuation with respect to the free field.

Initially, the length of the signal is determined and an appropriate FFT size is chosen for the calculation of the frequency spectrum. The choice of FFT size is determined by the length of the output signal. Due to the mathematical nature of the FFT, it is computationally preferable to choose a power of 2 close to the length of the output time response. For the calculation of the excess attenuation spectrum, an FFT size of 4096 points is sufficient since the length of the output signal is 4000 samples.

4.6 Terminology

This section will define the terminology used throughout the thesis to describe the features observed in the spectra of excess attenuation.

4.6.1 Surface Wave Magnitude

The exact magnitude of the surface wave is difficult to determine, as explained later in section 5.2.3. Throughout this thesis, the magnitude of the enhancement achieved through the introduction of surface roughness is taken to be the peak excess attenuation value minus the 6 dB associated with the maximum enhancement as a result of constructive interference due to reflection off an acoustically rigid surface.

4.6.2 Surface Wave Frequency

As in section 4.6.1, the surface wave frequency is assumed to be the frequency of the peak in the excess attenuation spectrum.

Chapter 5

Surface Wave Properties

5.1 Introduction

In this chapter, data is presented from measurements of the sound field generated over periodically spaced strips placed on an acoustically rigid surface. These measurements are conducted under anechoic conditions over surfaces made from periodically-spaced strips. The purpose of these measurements is to investigate the evolution and resulting properties of surface waves and how these are affected by varying the source-receiver geometry and the topography of the strips. The main surface wave properties have been outlined in chapters 2 and 3. They include an exponential decrease in amplitude with receiver height above the surface and a lower phase speed than that of sound in air. It is these properties that allow for the identification of surface waves, along with an excess attenuation value that exceeds the 6 dB associated with the maximum enhancement from constructive interference due to total reflection off an acoustically rigid surface. The measurements presented are compared with theoretical numerical calculations of the sound field using BEM, analytical calculations using the slit-pore model, as well as time-domain outputs from TDBEM and contour pressure maps obtained using ContourBEM.

5.2 Surface Wave Properties over Rectangular Strips

5.2.1 Surface Wave Speed

As mentioned in section 4.4.2 and above, the surface wave travels with a phase speed less than that of sound in air. It can be seen as a later arrival in the time domain. Section 4.4.2 outlines the phase gradient method for measuring the phase speed of the surface wave. Measurements were carried out using the motorised tracker covered in felt to reduce any extraneous reflections. The rough surface was composed of 30 periodically-spaced rectangular strips spaced by 0.01874 m with a source-receiver separation of 0.80 m. The source was placed at 0.05 m above the MDF and 0.01 m away from the edge of the strip array to ensure the receiver wasn't in contact with the source for the first measurement above the first strip. Then the receiver was moved away from the source, using the motorised tracker, at a height of 0.05 m in 0.01 m increments to obtain as many results as possible.

Figure 5.2 shows the resulting excess attenuation spectra from measurement and BEM. At low-frequencies between 0 Hz and 800 Hz, the sound is totally reflected from the surface resulting in an excess attenuation of 6 dB. Between 800 Hz and 2000 Hz, the effects of the strip surface on the total sound field are visible as enhancement features above 6 dB. Beyond 2000 Hz, the absorptive nature of the surface is visible as a negative peak in the spectrum. There reasonable agreement at low frequency and high frequency due to the ability of BEM to predict reflection and scattering effects, respectively. Between 800 Hz and 2000 Hz there is reasonable agreement however, as mentioned, BEM does not account for viscous and thermal interactions contributing to the sound field when the gap is small. It also doesn't account for the effects of finite width in the direction transverse to the propagation direction (see section 5.3.3).

Figure 5.3 shows that the BEM prediction is in reasonable agreement with measurement in showing that the surface wave peak near 2000 Hz. Figure 5.3 shows the phase speed as a function of frequency. At lower frequencies, the received signal is dominated by the direct arrival and so the phase speed is approximately that for the speed of sound at 334 ms^{-1}. At 1992 Hz, the phase speed is 302.7 ms^{-1} in agreement with theory. It should be noted that, although the measured and predicted surface wave speeds continue to decrease above 2000 Hz, this frequency range corresponds to destructive interference between direct and coherently reflected waves where the surface wave contribution is small.

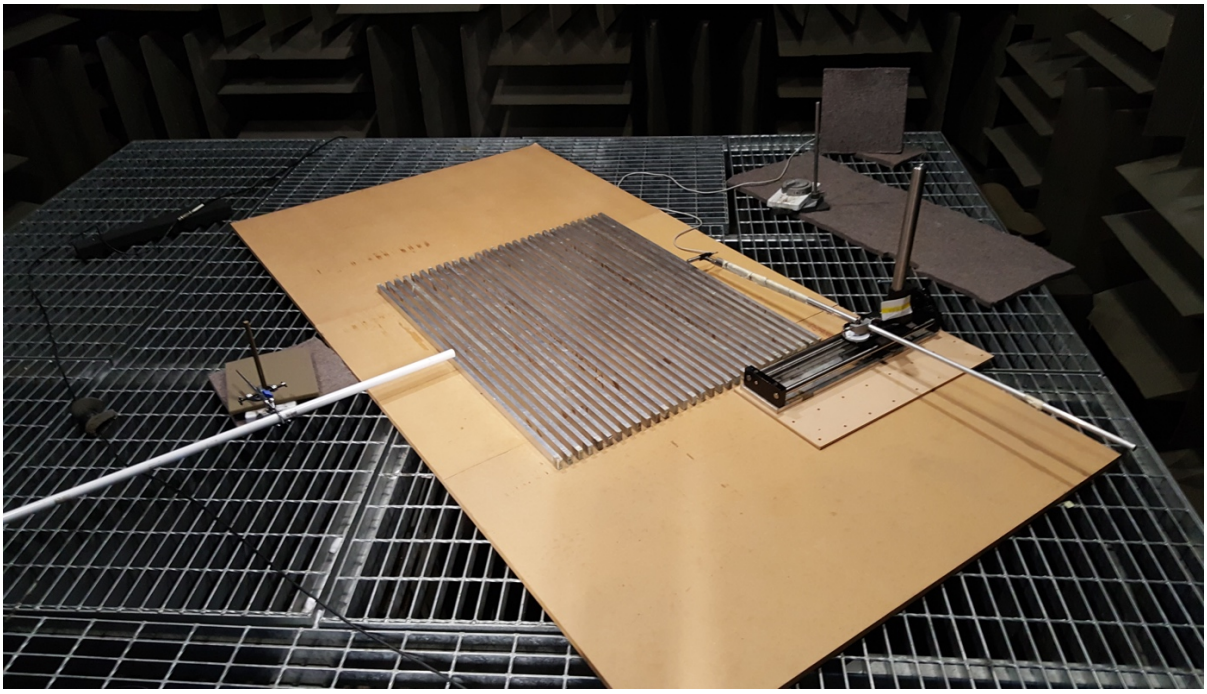

Figure 5. 1 *Photograph of motorised tracker and strip setup.*

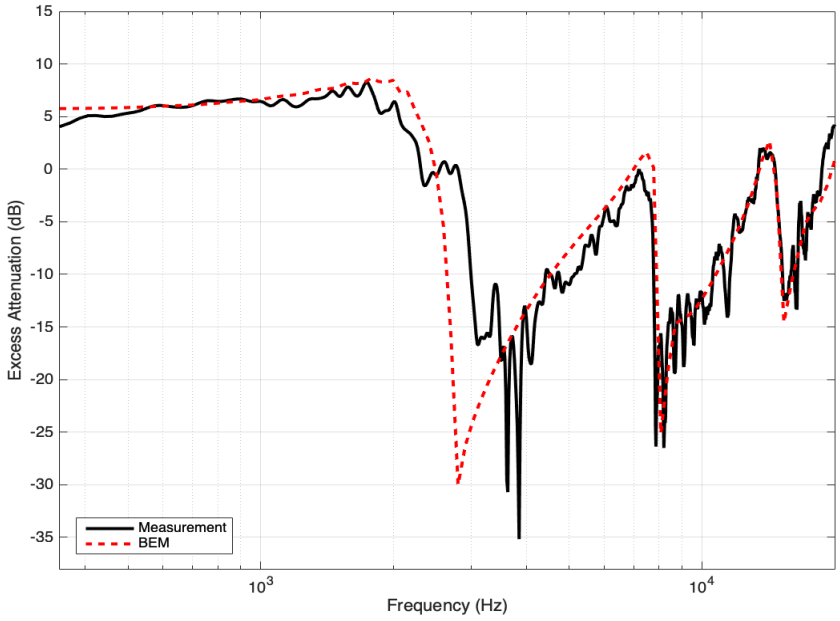

Figure 5. 2 *Excess attenuation spectrum and corresponding BEM result for 30 strips separated by 0.1874 m and a source-receiver separation of 0.80 m.*

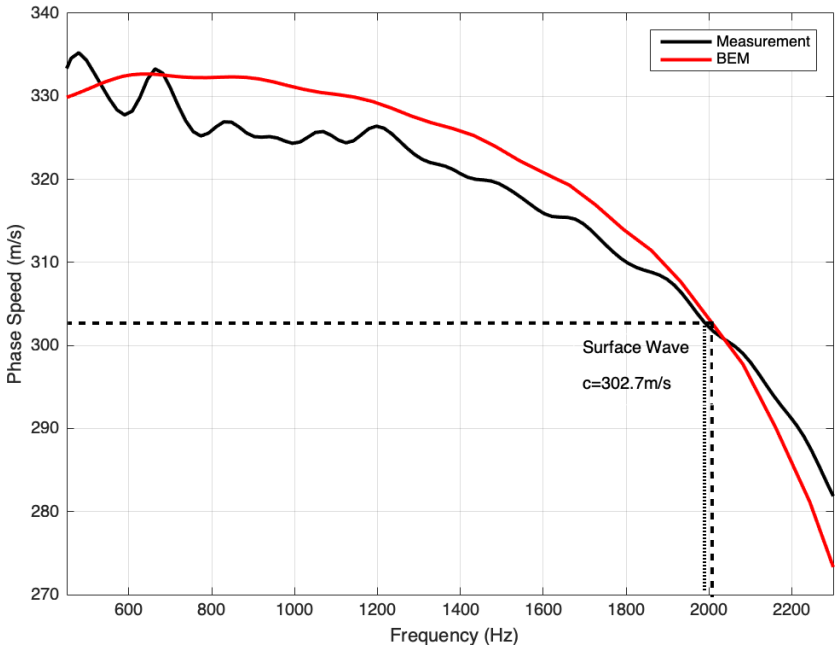

Figure 5. 3 *Phase speed as a function of frequency from measurements using a motorised tracker compared with the output from BEM simulations.*

Using the phase gradient method in BEM simulations of the same geometry yields a speed of 302.7 ms^{-1} at 2006 Hz as indicated by the dotted vertical line, in reasonable agreement with data.

Daigle and Stinson [22] investigated acoustical pulses over a lighting lattice used as a model impedance surface which was designed to have an extremely low resistive component. The reduced phase speed of surface waves allows them to be studied as later arrivals in the time-domain. The predicted phase speed of pulses over this surface, determined using Thomasson's method [6], beyond the surface wave frequency was significantly lower than that of the body wave, in agreement with the above results. This is due to the large imaginary component of the surface impedance. However, using Thomasson's formulation (equation 2.10), it appears that for larger source-receiver separations, the frequency of the surface wave decreases which, as can be seen from figure 5.3, results in an increase in surface wave speed until, eventually, it approaches the speed of sound. Moreover, Bashir [32] carried out similar measurements over lattice layers, which have an almost purely imaginary impedance. The phase speed predicted at the surface wave frequency of 1.5 kHz was 255 ms^{-1}. This is significantly lower than the phase speed observed in figure 5.3 and can be attributed to the lattice layers offering an effective impedance with a much larger reactance than the strip surface. It is possible to show this by modelling the surface as a rigid-backed slit-pore impedance layer with an effective porosity dependent on the thickness and the separation between the strips. The strips have a height of 0.0253 m (corresponding to the layer depth of the impedance surface) and a thickness of 0.0126 m. The effective porosity was calculated by using the thickness and the gap which was varied between 0.005 m and 0.100 m. The source-receiver separation was 1.00 m and the source and receiver heights were set at 0.04 m. Figure 5.3 shows the reactance as a function of the edge-to-edge separation between the strips. The reactance can be shown to quickly decrease with increasing effective porosity. This also

suggests that as the spacing between strips is increased, the surface becomes less like a slit-pore impedance layer. This is investigated in detail in chapter 6.

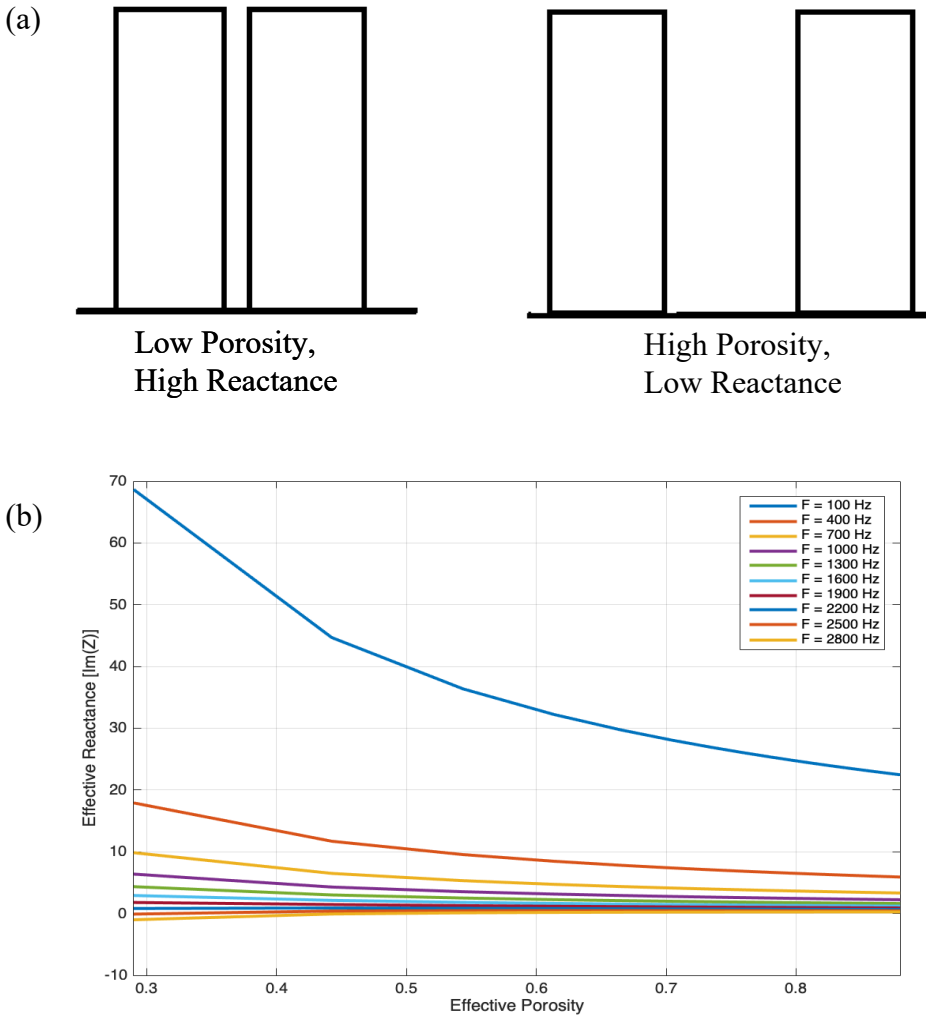

Figure 5. 4 (a) *Increasing gap resulting in decreased reactance.* ***(b)*** *Effective reactance of a strip surface at various frequencies as a function of effective porosity. The strips have a height of 0.0253 m (layer depth) and a thickness of 0.0126 m.*

The phase speed determined for the surface wave generated over a lighting lattice is lower than that for the surface wave generated over strips due to the effect of complex interactions between the incident sound field and the strip structure. This is investigated further in chapter 6.

5.2.2 Variation of Surface Wave Amplitude with Receiver Height

For these measurements, 30 periodically-spaced rectangular strips with a height of 0.0253 m and a thickness of 0.0126 m were placed on a piece of Medium Density Fibreboard (MDF) of dimensions 1.20 m x 2.40 m. The source and receiver were separated by 0.70 m and placed 0.04 m above the MDF. The gap between strips was 0.015 m. The close spacing of the strips means the surface will act as a slit-pore impedance layer. The measurement process is outlined in section 4.4.1. The receiver was gradually increased in 0.01 m increments above the strip surface and the sound pressure at the excess attenuation maximum was determined by re-arranging equation 4.5 and plotting against receiver height.

Figure 5.5 shows the resulting excess attenuation spectrum. For low receiver heights, there is a broad surface wave maximum above 6 dB which peaks at 1898 Hz. The broadness of the area of the excess attenuation spectrum above 6 dB is due to the fact that there exists visco-thermal dissipation within the slits. This means the surface wave is dispersive with its phase velocity dependent on the frequency. Furthermore, the extra peaks in the excess attenuation spectrum imply that the interactions between the incident sound field and the strip surface are contributing to enhancement at a wider range of frequencies. This is evident in the time-domain as a wave train that follows the main arrival at 0.01 s in figure 5.6. The later arrival of this wave-train is in agreement with the nature of the surface wave speed determined in section 5.3.1. However, it resembles a beat-like pattern which implies the interference of two or more waves which are similar in their frequency content. Plotting the logarithm of the maximum amplitude against receiver height yields the expected linear relationship and so it can safely be assumed that the surface wave frequency is indeed that where the excess attenuation and the amplitude is greatest.

At higher frequencies above 3000 Hz, the effect on the sound field is dominated by scattering as can be seen in figure 5.2 by the improved agreement at high frequency between measurement and BEM which, as mentioned, takes into account scattering.

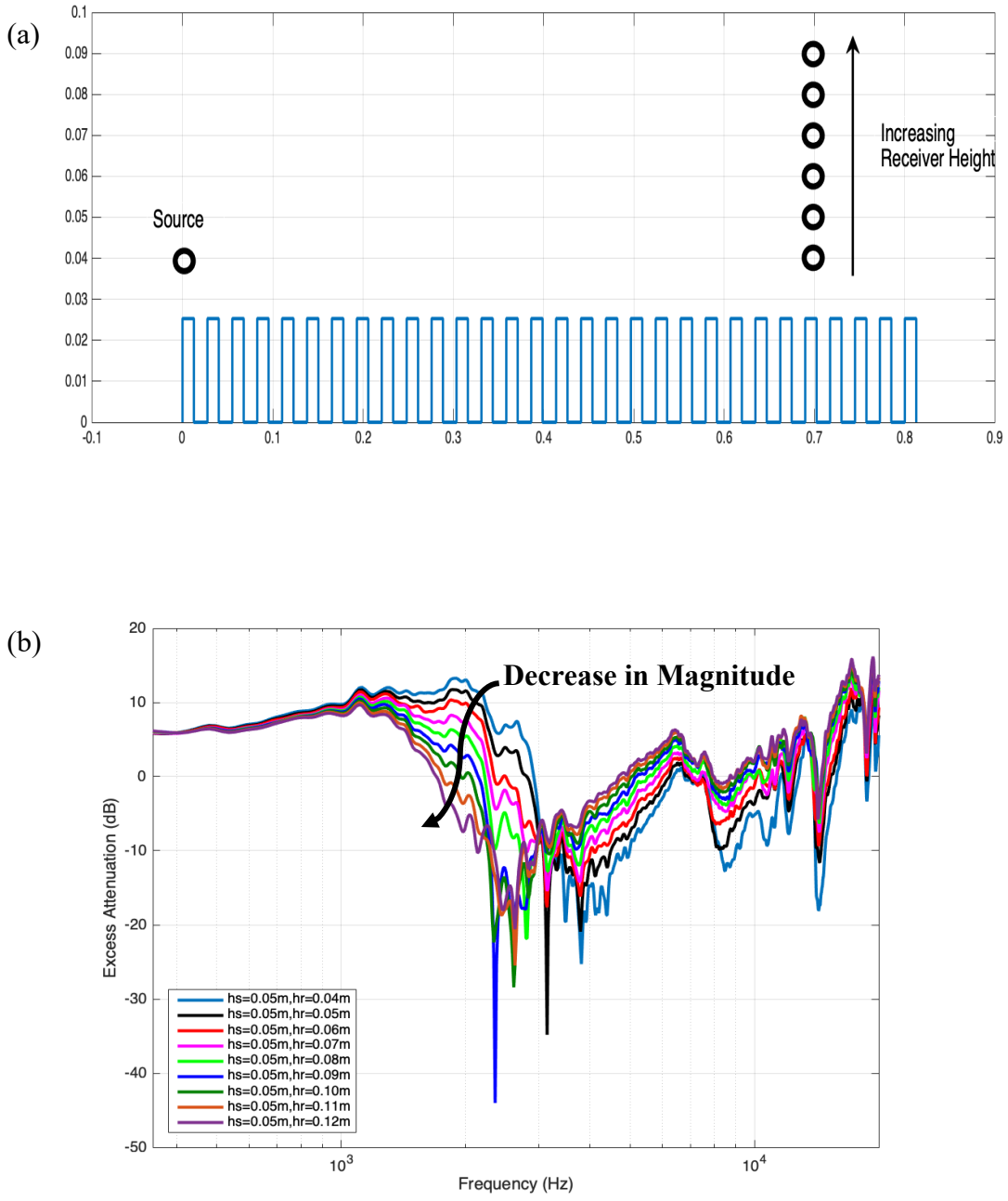

Figure 5. 5 (a) *Diagram showing increasing receiver height above surface.* ***(b)*** *Measured excess attenuation spectra for increasing receiver heights between 0.04 m and 0.12 m above 30 x 0.0253 m-high aluminium strips regularly spaced at 0.015 m on MDF.*

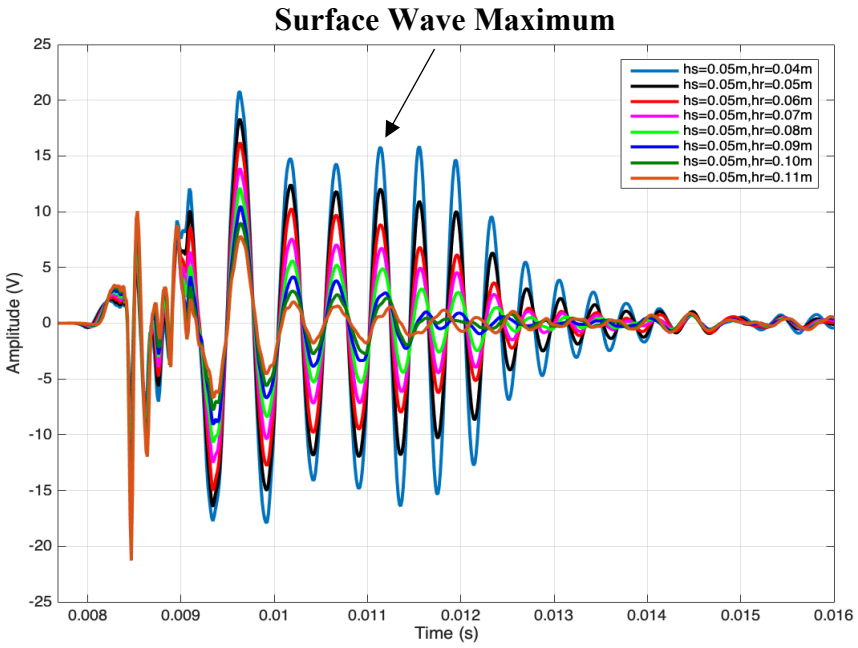

Figure 5. 6 *Time-domain plots for increasing receiver heights between 0.04 m and 0.12 m above 30 x 0.0253 m high aluminium strips regularly spaced at 0.015 m on MDF.*

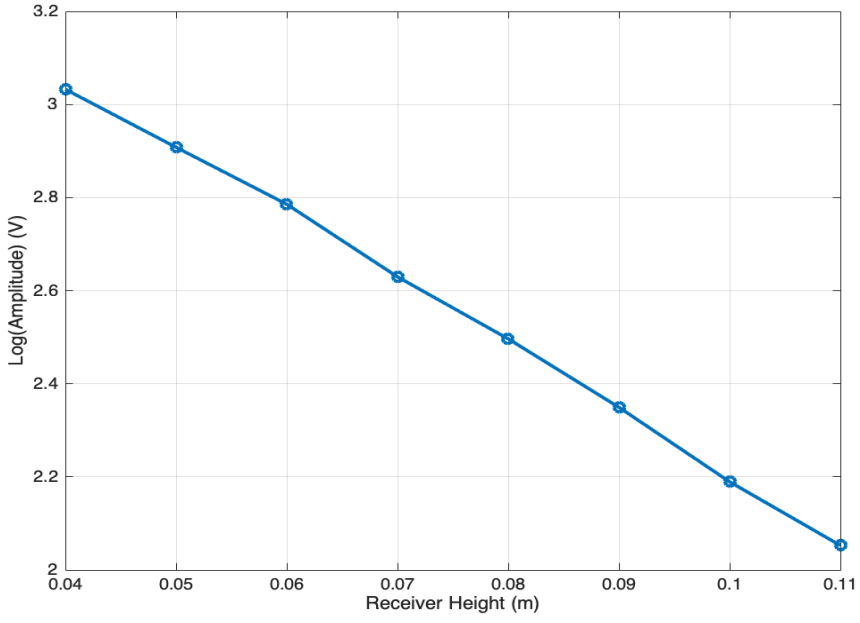

Figure 5. 7 *Log(Amplitude) at the peak of the wave-trains following the arrival of the main pulse in figure 5.6 as a function of receiver height.*

5.2.3 Surface Wave Magnitude Using BEM

The absolute surface wave magnitude is difficult to determine since it requires the total separation of the surface wave in the time-domain which has proven difficult due to experimental constraints applied by the size of the anechoic chamber and by computational constraints due to the time taken to calculate the sound field over much larger arrays. Furthermore, the excess attenuation spectra in figure 5.5 exhibit several peaks which implies that there are other interactions between the sound field and the strip surface which contribute to the signal enhancement from which the surface wave contribution must be separated.

A BEM simulation was set up to calculate the total sound field over a 3 m array composed of 93 strips spaced at 0.02 m and with a thickness and height of 0.0126 m and 0.0253 m respectively. The frequency of the peak in the excess attenuation spectrum is then input as the centre frequency of the Ricker pulse used in the TDBEM simulation. The frequency content of the later arrival is determined by taking a 4096-point FFT of the wave-train that follows the arrival of the main pulse.

Figure 5.8 shows the outputs from the BEM and TDBEM simulation. The wave-train following the arrival of the main pulse at 0.01 s exhibits a similar broad frequency spectrum and thus it is possible that the surface wave and the other enhancing mechanisms are a result of the finite extents of the strip array. This is also exhibited in the excess attenuation spectrum in figure 5.8 (a). As mentioned, the broadness of the peaks implies that the surface is acting like a slit-pore impedance layer. However, there is a second peak exhibited in the spectrum of the wave-train in figure 5.8 (c) which arises due to more complex interactions arising between the incident sound and the strip surface. These interactions depend on the geometry and topography of the strip surface and are investigated in more detail in chapter 6.

This implies that the interactions between the sound field and the strip surface has potential to enhance signals for a wider range of frequencies than just that of the surface wave.

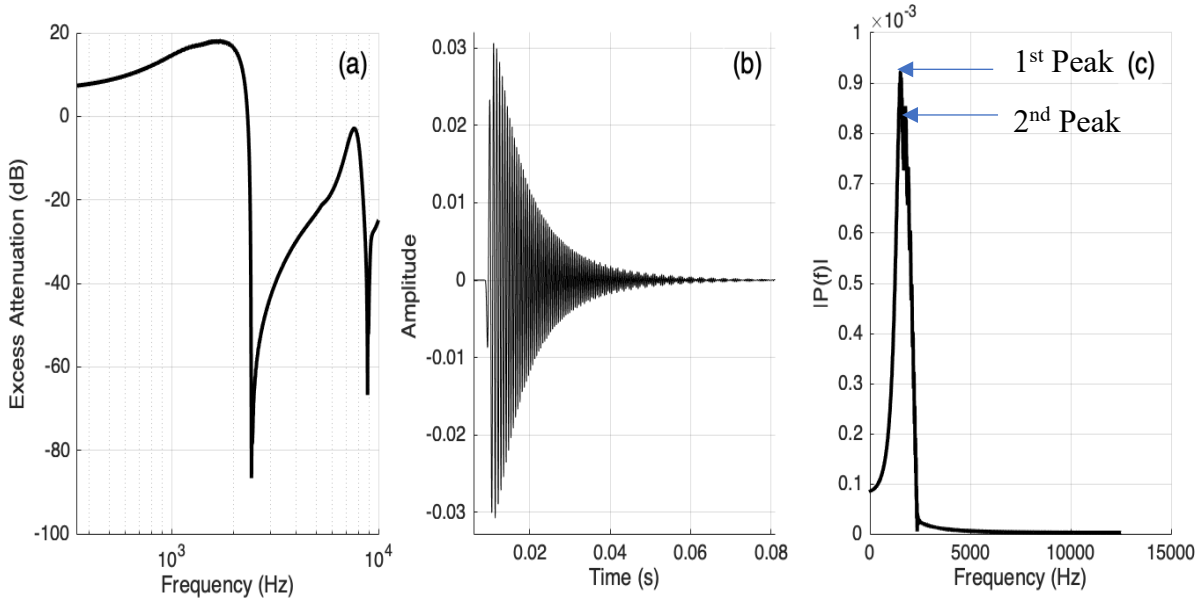

Figure 5. 8 (a) *BEM-predicted excess attenuation spectrum for 93 strips with thickness 0.0126 m and height 0.0253 m and spaced at 0.02 m. The source and receiver are separated by 3.00 m.* ***(b)*** *Corresponding time-domain result.* ***(c)*** *Frequency content of the wave-train following the arrival of the main pulse. .*

5.3.3 Finite Array Width Effect

An enhancement feature of note corresponds to the extra peaks near 2653 Hz in the measured excess attenuation spectra shown in figure 5.5. Figure 5.9 shows the excess attenuation spectrum for the strip geometry in figure 5.5 with the source and receiver placed at 0.05 m and 0.04 m respectively. This feature is not simulated in the output of the BEM simulation corresponding to the same geometry also shown in Fig. 5.9 since the BEM output is the result of a 2D simulation, and so is thought to be a result of the finite width of the strip array in the direction transverse to the propagation direction.

This enhancement feature arises as a result of constructive interference due to reflection from the edges of the strips and is therefore termed the 'finite array width effect.' The reflections arise at the boundary between the aluminium strip and the air beyond due to the impedance discontinuity. As shown in the setup in figure 5.11, it is possible to reduce this effect by introducing sound-absorbing material, felt in this case, to the ends of the strip array as shown in figures 5.9 and 5.10. On the other hand, these enhancement effects offer further potential for amplifying frequencies other than that of the surface wave which further highlights the signal-enhancing potential of periodic-roughness arrays.

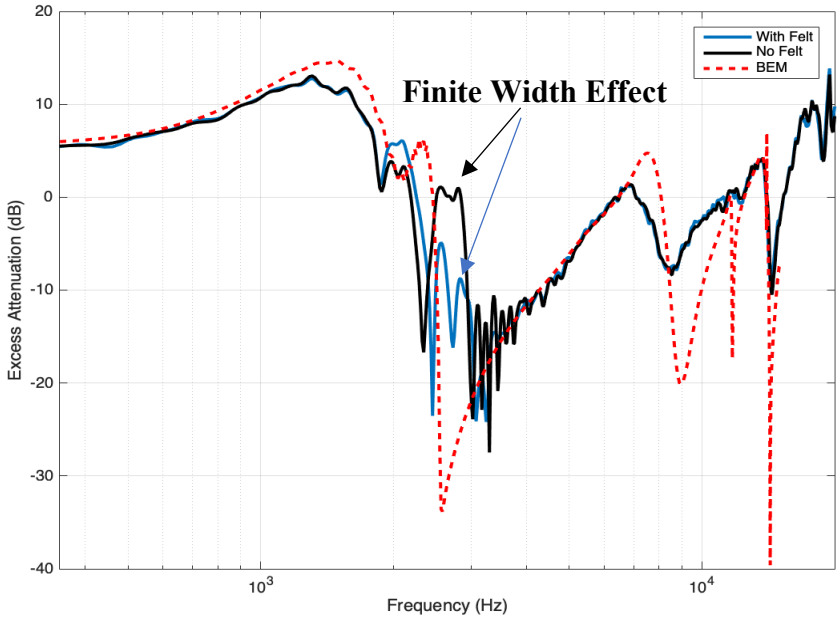

Figure 5. 9 *Excess attenuation spectrum from measurement and corresponding BEM simulation output for 30 periodically-spaced strips spaced by 0.015 m placed on MDF with and without felt placed at the ends of the strip array.*

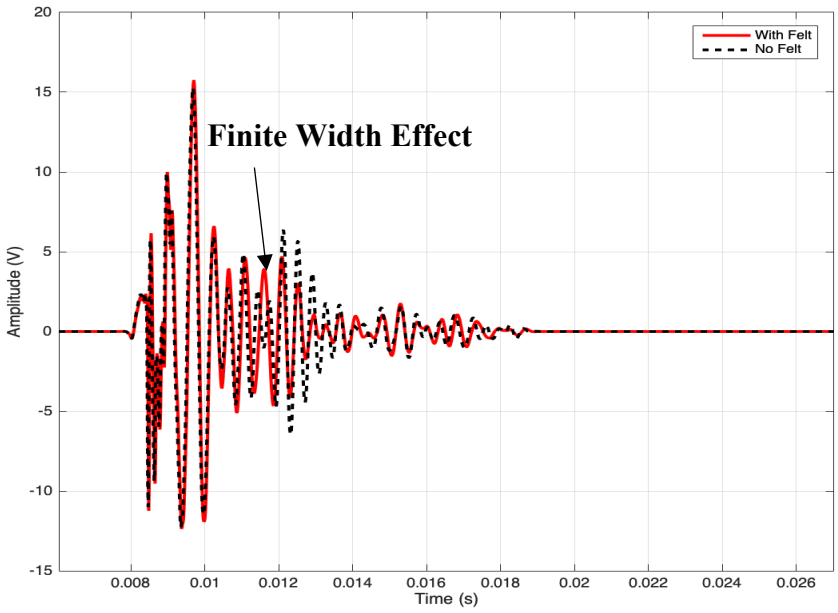

Figure 5. 10 *Corresponding time-domain plot.*

Figure 5. 11 *Experimental setup for strips with felt placed at each end of the strip array.*

The reduced peak at 0.012 s in figure 5.10 corresponds to the finite array width effect in the time-domain.

Figure 5.9 also shows another enhancement feature very close to the surface wave frequency at 2064 Hz. This feature is predicted by the 2D BEM and thus cannot be a result of finite width of the array.

It was first thought that this enhancement feature could be a result of reflections from strips beyond the source and receiver in the direction of propagation. This could possibly explain why the feature appears in the 2D BEM calculation.

Calculations of the path length difference and the associated frequency of constructive interference showed that this is not the case since it appears there is not much change between the frequency of this feature with increasing path length.

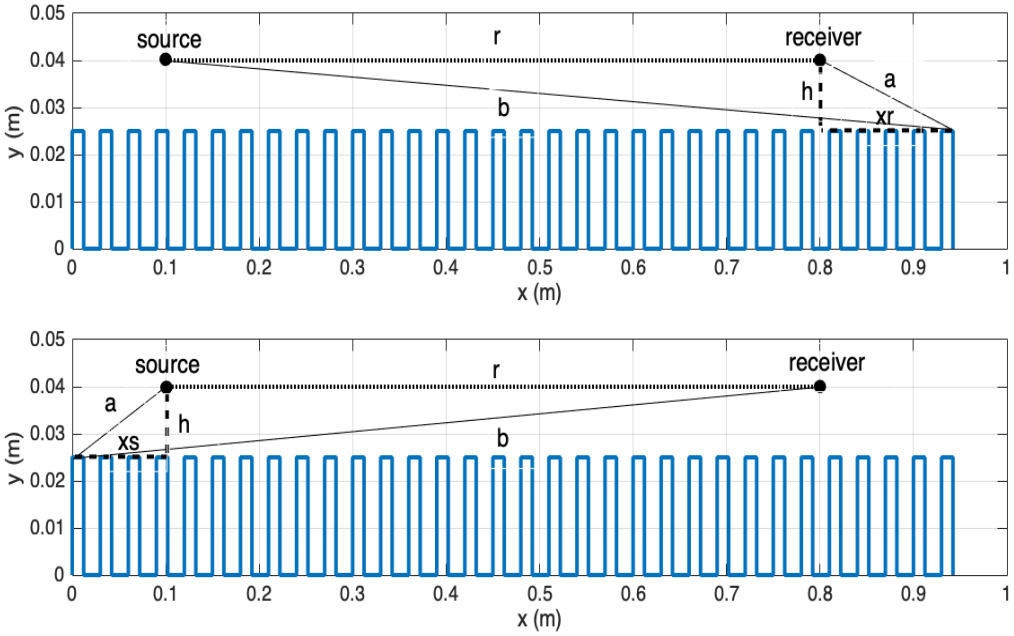

Figure 5. 12 *Direct and reflected paths from the receiver (top) and source (bottom).*

From figure 5.12, the path length difference Δx can be determined from,

$$\Delta x = \left(a + b\right) - r = n\lambda$$
$$a = \left(h^2 + x_{r,s}^2\right)^{1/2} \quad , \quad b = \left[h^2 + \left(r + x_{r,s}^2\right)\right]^{1/2} \tag{0.84}$$

where $\Delta x = n\lambda$ is the condition for constructive interference. For the excess attenuation spectra corresponding to the source-receiver geometry outlined in figure 5.9, the path length differences between the main arrival and the reflected contributions from the source and receiver ends of the array is displayed in table 5.1 alongside the associated measured values. The source-receiver geometry was fixed with a separation of 0.70 m and strips were added to each end of the strip array in order to increase the path length for the reflected wave. The wave speed used was that determined in section 5.2.1 of 302.7 ms^{-1}.

The measured data show no appreciable change in the frequency of this second enhancement feature and the constructive interference frequencies calculated from path length difference

show no agreement whatsoever and, therefore, this feature is not a result of interference between any reflected contributions and the main pulse.

To examine the extent to which the extra enhancement is a result of the structure of the array it is necessary to investigate the sound field generated above and between the strips by varying the strip properties and geometry. Various methods for investigating this experimentally have been considered.

The introduction of probe microphones between the strips could measure the sound pressure in between the gaps. However, these would introduce unwanted reflections and interfere with the sound field. Another possibility is to use Particle Image Velocimetry (PIV). This method requires encasing a strip array and seeding the area with tracer particles. The sound then disturbs the particles and allows for visualisation of the motion of the air particles the resultant velocity field. However, this method is time-consuming, and the encasement would affect the sound field.

Given the difficulties of relevant experiments, numerical investigations have been carried out in chapter 6.

Reflection from Receiver Side of Array			
Number of Strips	**Path Length Difference (m)**	**Frequency from Path Length Difference (Hz)**	**Frequency of Feature in EA Spectrum (Hz)**
30	0.0972	3115	1824
32	0.1516	1997	2008
36	0.2614	1518	2027
40	0.3715	815	1935
Reflection from Source Side of Array			
Number of Strips	**Path Length Difference(m)**	**Frequency from Path Length Difference (Hz)**	**Frequency of Feature in EA Spectrum (Hz)**
30	0.1330	2277	1824
32	0.1877	1612	2008
36	0.2977	1017	2027
40	0.4078	742	1935

Table 5. 1 *Path length difference and associated frequency content of constructive interference for varying number of strips with a fixed source-receiver geometry.*

5.3 Measurements Using a Geophone in Sand

It has been shown that periodically-spaced strips placed on an acoustically hard surface can enhance acoustic signals through the generation of air-borne acoustic surface waves as well as extra enhancement features that arise due to the structure of the array. In this section, a Mark Products Inc HZ510 geophone is used alongside a microphone to investigate whether the enhancements in the sound field affect the geophone signal as a result of acoustic-seismic coupling.

5.3.1 Acoustic-Seismic Coupling

Loud sources of noise can create low-frequency sound waves which can travel long distances and cause disruption in public environments. One source of disruption arises through discomfort experienced by the public and another is the fact that the natural frequency of many buildings lies between 1 – 10 Hz [2] and so the disturbance caused by such sources of noise need to be accounted for in the plan for architectural projects.

It has been determined [51, 52, 53] that simple ground-impedance models based on plane waves, non-elastic porous layer resonances and rigid-porous ground models do not accurately predict the acoustic-seismic coupling of loud impulsive noise sources at the receiver, and instead the ground must be modelled as a porous-elastic medium.

Theories for porous-elastic media predict the existence of three waves in the propagating in the air-filled porous ground [54]. There are two dilatational waves and one rotational wave. The Type-1 dilatational wave is also termed the ‘fast’ wave. It is highly attenuated as a result of viscous forces in the fluid within the pores acting on the pore walls. The attenuation of the Type-1 wave is proportional to the square of the frequency. This interaction at the pore walls means some of the energy is transmitted into the pore fluid as the Type-2 dilatational wave.

This wave has negligible dispersion since the phase velocity is primarily dependent on the mechanical parameters as opposed to the frequency.

Type-2 dilatational waves have lower velocities than Type-1 waves, are termed ‘slow waves’ and are highly attenuated as a result of viscous and thermal exchanges between the pore fluid and the pore walls. Below a critical frequency the slow wave is diffusive and is similar in nature to the diffusion processes associated with heat conduction. It is for this reason that Biot describes the Type-1 wave as the ‘true’ wave propagating in the pores.

The rotational wave propagates in the solid-frame and attenuates also with the square of the frequency. There is some attenuation due to viscous forces associated with relative movement between the solid and the pore fluid however the fluid is unable to support the propagation of rotational waves.

This section explores the potential for the detection of the enhanced acoustic signals using a geophone as the primary receiver. The results are compared with those obtained using a microphone.

5.3.2 Geophone & Microphone Results

The measurements were taken in a 1.2 m x 1 m x 0.5 m sandpit built using recycled chip-board. The sand was wetted slightly on the surface to reduce any potential scattering and nonlinear effects from the sand grains at the surface. It is important to fill the box to the rim and place the source and receivers well away from the edge of the box to ensure any reflections are minimised. The source is placed above the first strip at 0.035 m. The receivers are placed 0.95 m away from the source with the microphone at 0.05 m and the geophone carefully placed directly below it.

Initially, the number of strips used was 20. This was then increased to 30 and 36 to see if the number of strips had any effect on the signal enhancing potential of the surface. The strips were placed carefully onto the sand surface without creating small mounds which could introduce unwanted scattering.

BEM calculations corresponding to the geometries above were carried out for strips over both hard ground and the sand. The slit-pore model was found to be suitable for the wet sand with impedance parameters [55] of $\Omega = 0.37$ and $R_s = 479 Pasm^{-4}$. The layer depth was assumed to be 0.50 m, equal to the height of the box.

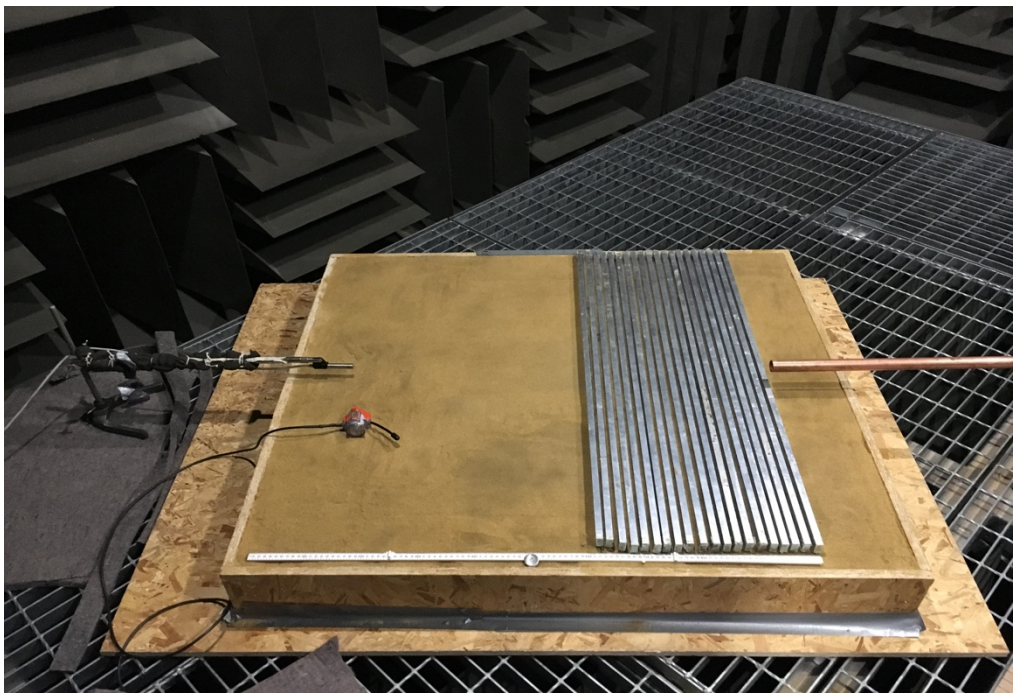

Figure 5. 13 *A photograph of the sandpit with the geophone placed just underneath the microphone.*

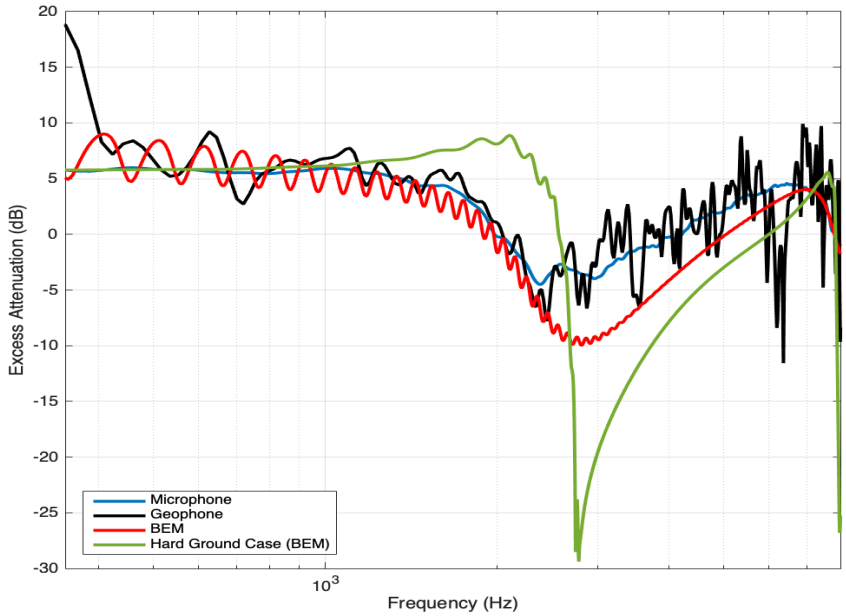

Figure 5. 14 *Excess attenuation spectra for 20 periodically spaced strips placed in sand with centre-to-centre spacing of 0.02 m and a source-receiver separation of 0.95 m.*

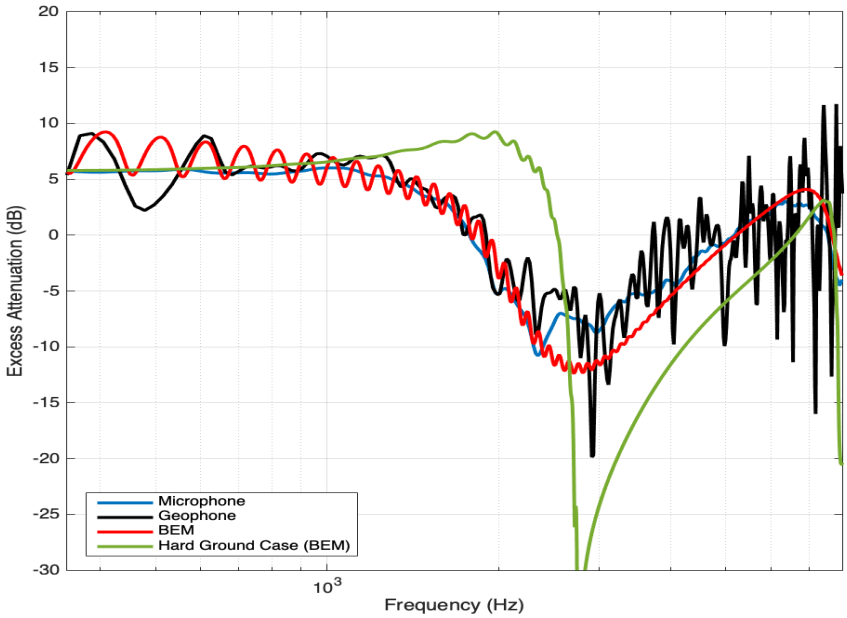

Figure 5. 15 *Excess attenuation spectra for 30 periodically-spaced strips placed in sand with centre-to-centre spacing of 0.02 m and a source-receiver separation of 0.95 m.*

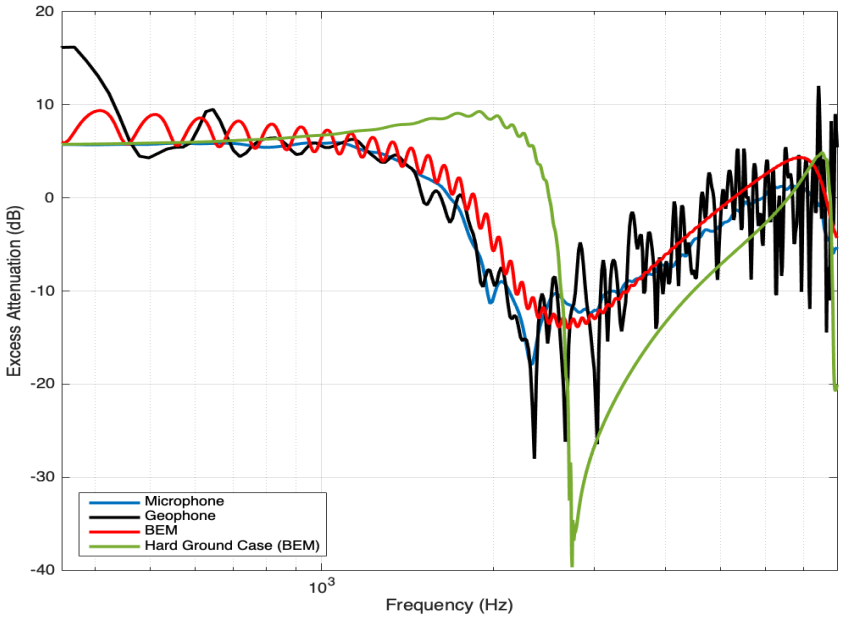

Figure 5. 16 *Excess attenuation spectra for 36 periodically-spaced strips placed in sand with centre-to-centre spacing of 0.02 m and a source-receiver separation of 0.95 m.*

Figures 5.14 – 5.16 show that the geophone and the microphone are detecting the same signal generated from the source.

Enhancement around 2000 Hz due to a surface wave is predicted if the strips are placed on an acoustically-rigid surface. However, the introduction of a ground surface with a finite impedance reduces the surface wave and hence any associated seismic signal enhancement due to transmission into the surface, even with a large number of strips. The sand surface is sufficiently absorbing so as to reduce the surface wave completely.

Calculations of the total field above the strip surfaces have been carried out using the ContourBEM outlined in section 3.2.4. The geometry for the 30-strip setup in figure A2 is altered slightly to improve the resolution of the pressure map. The strips are separated by 0.0178 m with a thickness of 0.0122 m and a height of 0.025m. In order to simulate the ground conditions associated with the wetted sand, the ground surface below the strips was

modelled as a slit-pore impedance surface with a layer depth of 0.50 m, a porosity of $\Omega = 0.37$ and a flow resistivity of $R_s = 479 Pasm^{-4}$ [55]. The contour pressure map is generated at the excess attenuation maximum of 1639 Hz associated with the sound field maximum above strips placed on hard ground.

These pressure maps further confirm that there are no enhancement features generated when the strips are placed on soft ground and so a collocated geophone cannot detect any enhanced signals.

Figure 5.17(a) exhibits strong high-pressure regions above the strips associated with the enhancement features observed above 6 dB in the excess attenuation spectra. They arise as a result of quarter wavelength resonances forming in the gaps between strips due to the fact that gap is acting like a pipe closed at one end. These features are explored in detail in chapter 6. However, they are completely damped by the presence of a porous ground surface. The sound field in figure 5.17 (b) shows only spherical spreading of the wave between source and receiver.

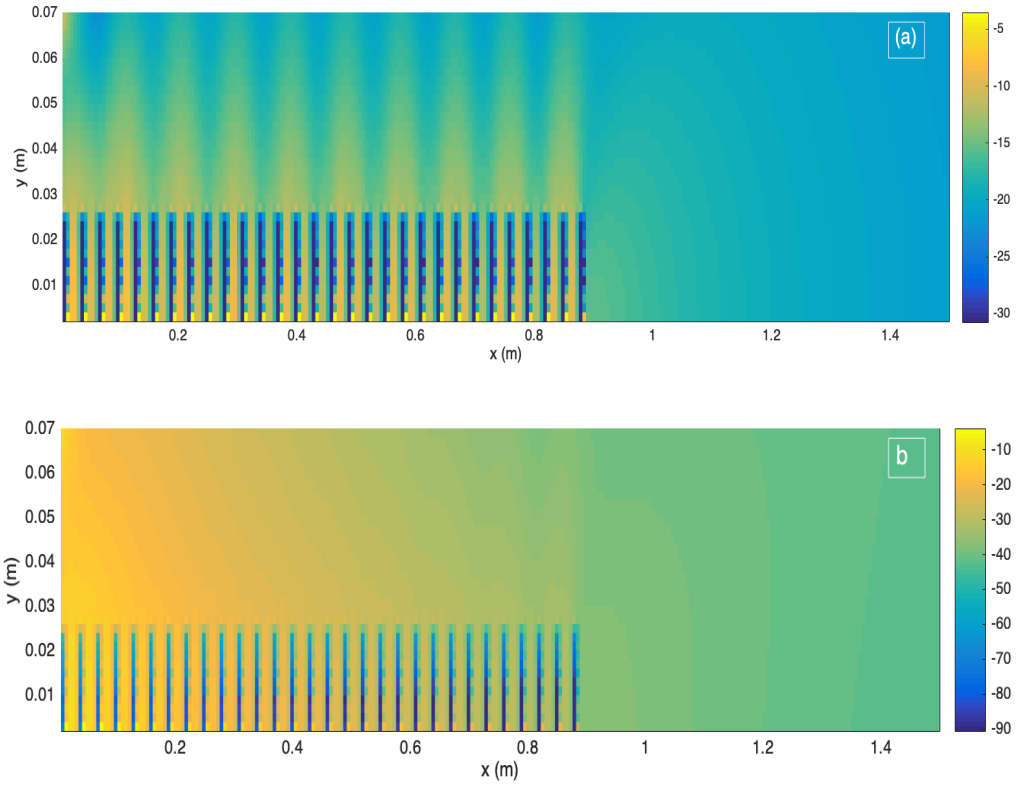

Figure 5. 17 *Total sound field over 30 periodically-spaced rectangular strips at 1639 Hz over* ***(a)*** *acoustically rigid ground* ***(b)*** *wetted sand.*

Chapter 6

Investigating the Total Sound Field.

6.1 Introduction

In the previous section, it has been shown that it is possible to enhance acoustic signals via the introduction of periodically-spaced strips via the generation of air-borne acoustic surface waves. Further to this, measured and predicted excess attenuation spectra exhibit extra enhancement features just beyond the surface wave frequency that arise as a result of the strip structure. These features could not be explained by constructive interference between reflected contributions from the edges of the array transverse to the propagation direction and the main arrival. These features appear in contour plots as high-pressure regions above the strip array which appear to be generated by quarter-wavelength resonances in between the gaps.

Since experimental investigation of these features is difficult, it is preferable to use numerical methods. In this chapter, BEM, the use of which has been validated previously, is used to investigate features seen in the excess attenuation spectra in chapter 5. A series of simulations has been carried out to investigate how varying the geometry of the strip arrays affects the total sound field generated over the strips. Excess attenuation spectra and pressure contour maps are presented as well as calculations of parameters associated with the observed features.

In the first section, the extra enhancement features observed in the previous chapter are investigated further. The theory of quarter-wavelength resonators is introduced and the associated resonant frequencies are calculated for each gap. In the following sections, the

strip height, thickness and spacing is varied in turn to investigate the effect of varying the surface geometry on the enhancement potential of the surface.

6.2 Investigation of Extra Enhancement Feature

The enhancement features observed in chapter 5 seem to be a result of high-pressure regions above the strip array which are generated between the gaps. To investigate the extra enhancement in the excess attenuation spectrum shown in Fig.5.9, the ContourBEM program, outlined in section 3.2.4, has been used to generate pressure contour maps of the total sound field over the strips at the frequencies of interest.

The receiver-grid generated for these simulations contains a total of 8750 receivers, 250 in the x-direction and 35 in the y-direction. In the x-direction, each receiver is separated by 0.006 m and the receiver locations extend to a distance of 1.5 m and in the y-direction, each receiver is separated by 0.002 m and the receiver locations extend to a height of 0.07 m which is 0.045 m above the top of the strip array. Two strip separations are considered. The first simulation contains 40 strips with a thickness of 0.0122 m, a height of 0.025 m and each separated by 0.0178 m. The second consists of 23 strips with the separation increased to 0.0534 m.

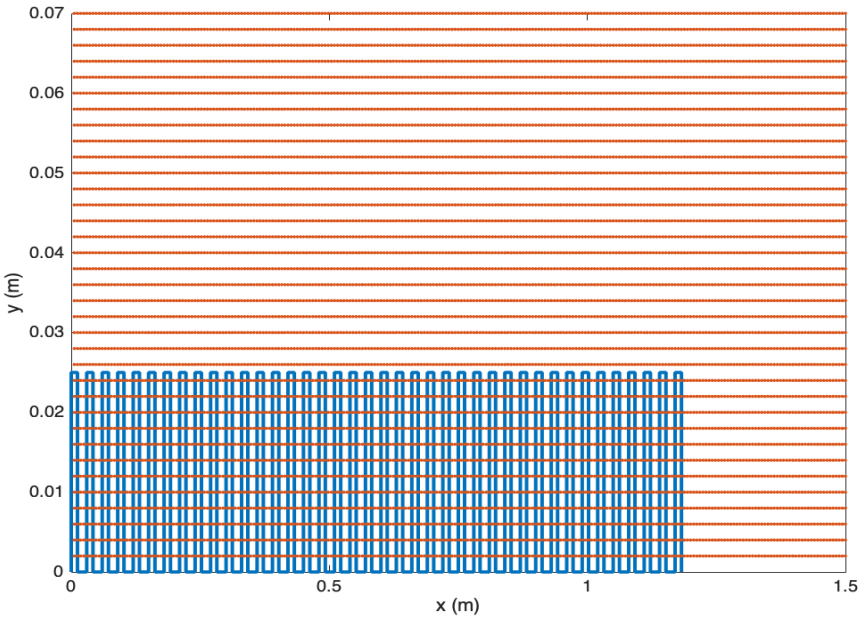

Figure 6. 1 *40 strips with a height of 0.025 m and a thickness of 0.0122 m separated by 0.0178 m (blue). A grid of receivers separated by 0.006 m in the x-direction, 0.002 m in the y-direction.*

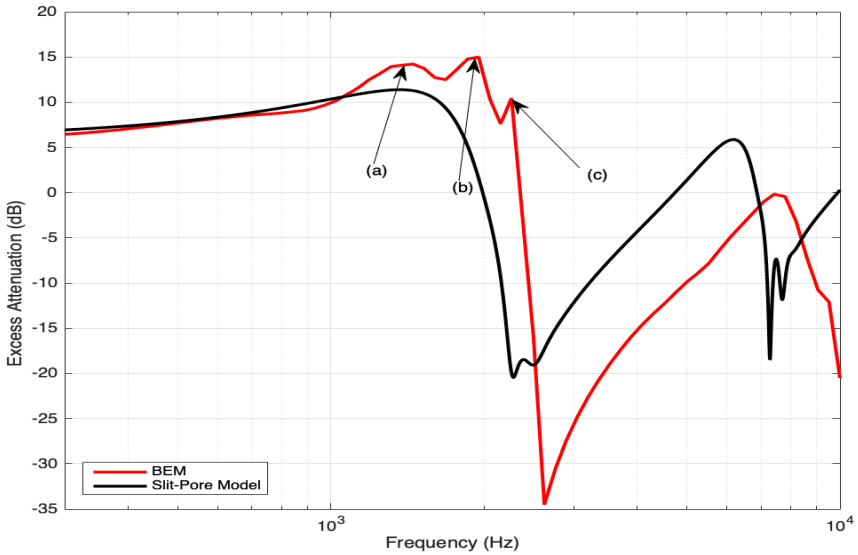

Figure 6. 2 *Excess attenuation spectrum obtained from a BEM simulation of 40 strips of height 0.025 m and thickness 0.0122 m separated by 0.0178 m compared to the excess attenuation for the equivalent slit-pore layer.*

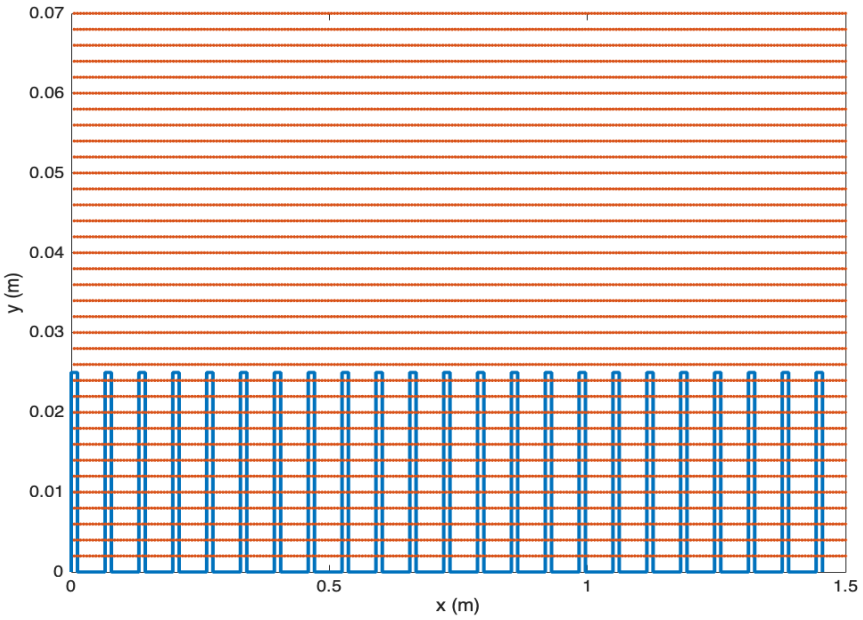

Figure 6. 3 *23 strips of height 0.025 m and thickness 0.0122 m separated by 0.0534 m (blue). A grid of 8750 receivers separated by 0.006 m in the x-direction, 0.002 m in the y-direction.*

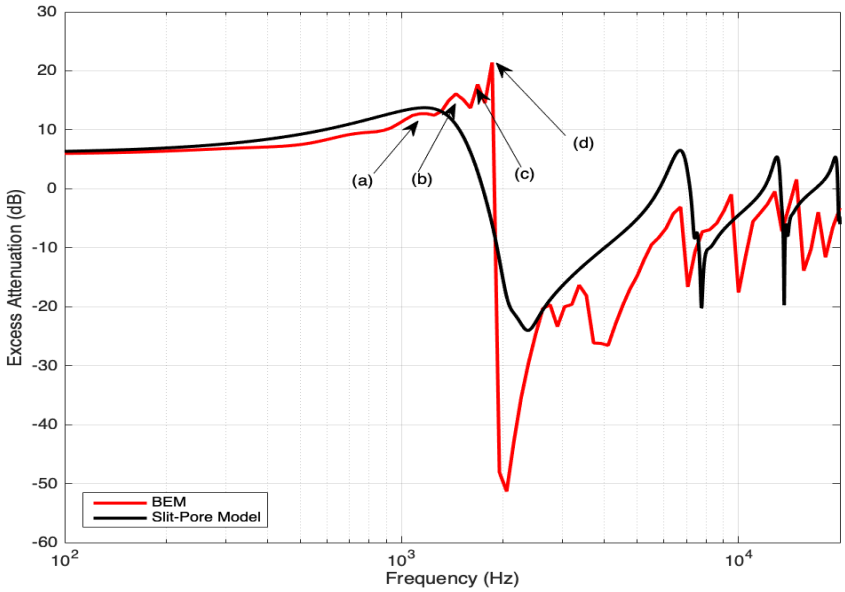

Figure 6. 4 *Excess attenuation spectrum obtained from a BEM simulation of 23 strips of height 0.025 m and thickness 0.0122 m separated by 0.0534 m compared to the excess attenuation for the equivalent slit-pore layer.*

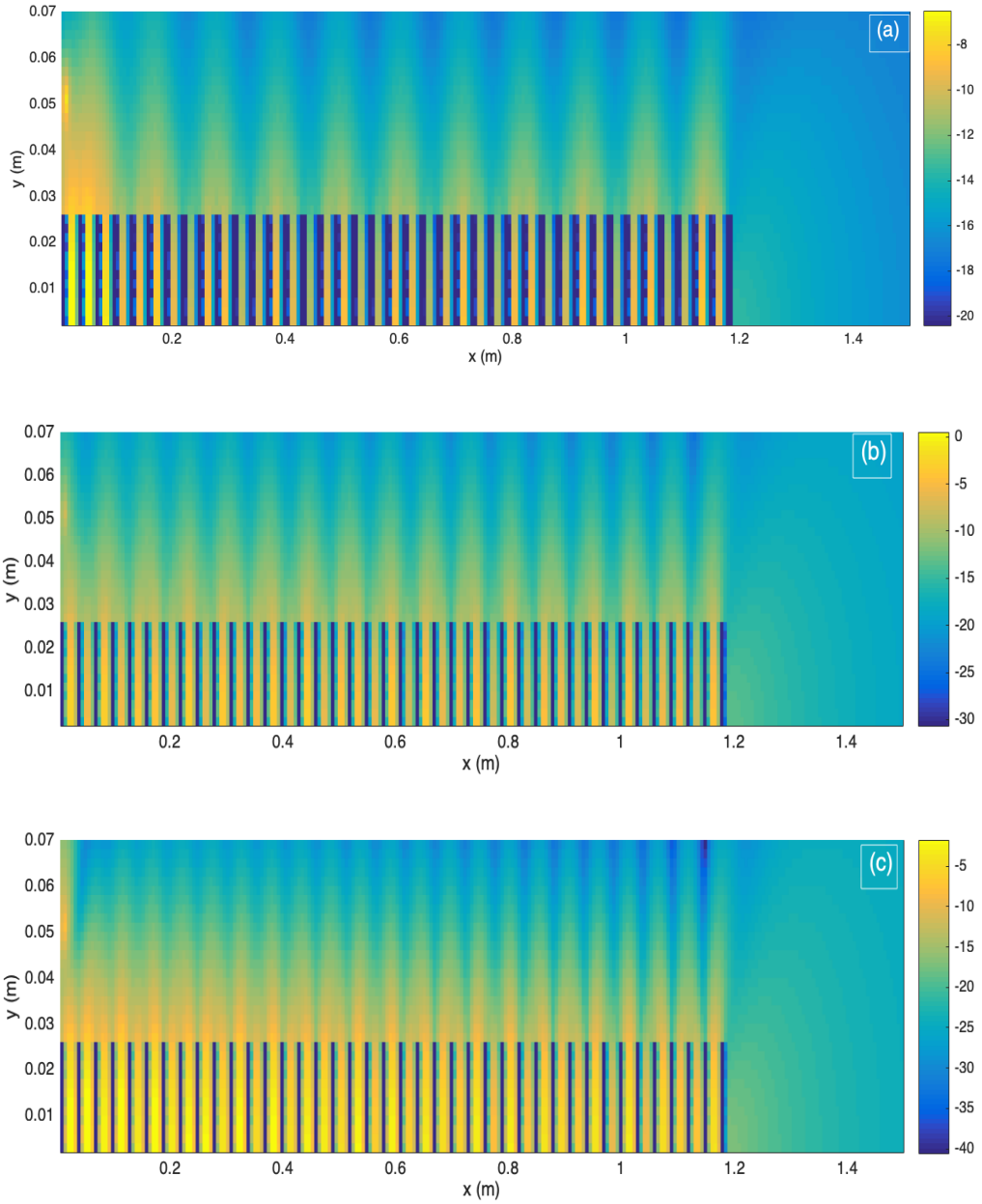

Figure 6. 5 *Total pressure field over 40 periodically-spaced strips at* ***(a)*** *1450 Hz,* ***(b)*** *1951 (Hz) and* ***(c)*** *2264 Hz.*

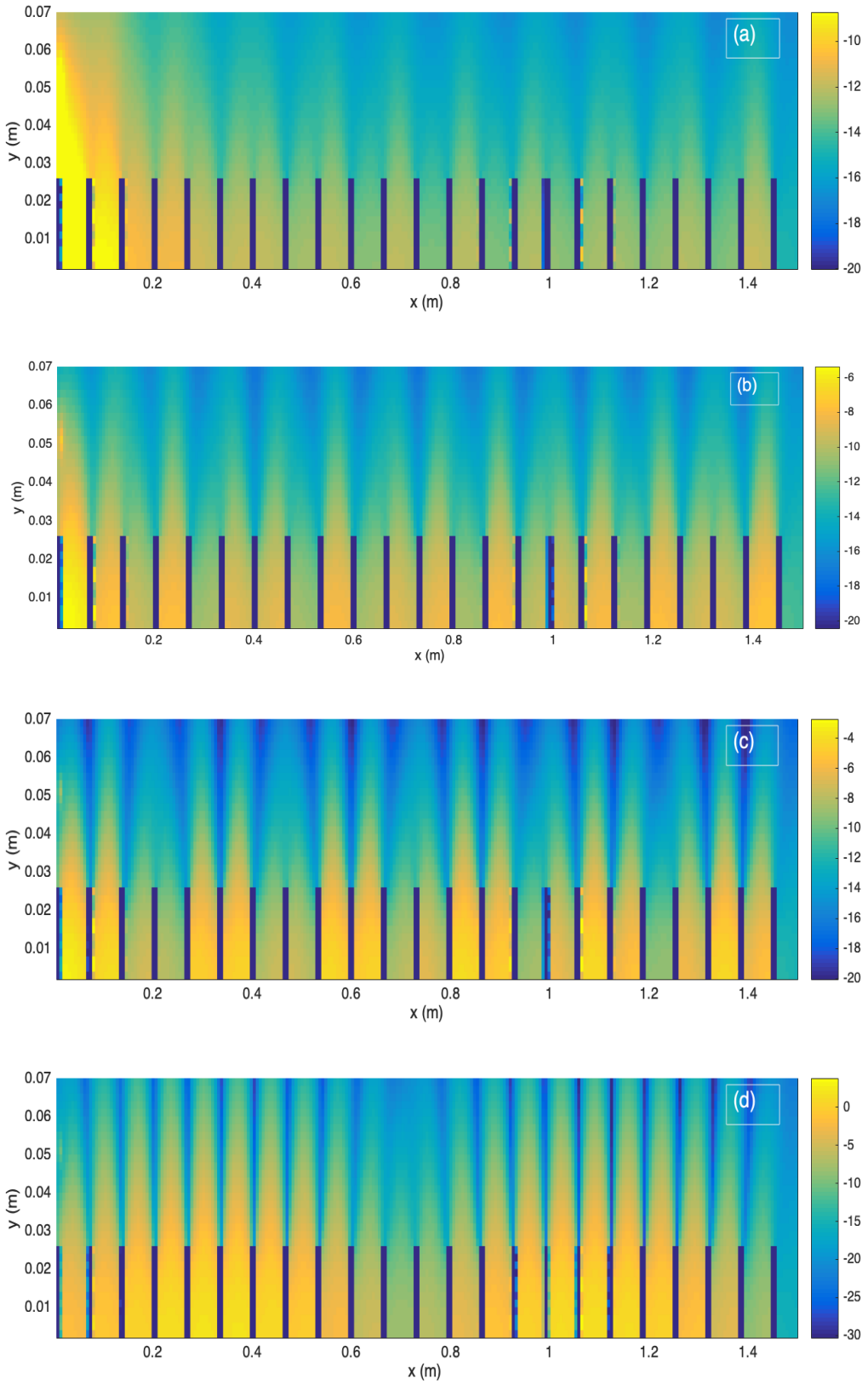

Figure 6. 6 *Total pressure field over 23 periodically-spaced strips at* ***(a)*** *1132 Hz,* ***(b)*** *1450 Hz,* ***(c)*** *1682 Hz and* ***(d)*** *1857 Hz.*

The geometry in figures 6.1 and 6.3 is chosen to ensure an even distribution of receivers over the strip array. This greatly improves the clarity and resolution of the pressure map. Figure 6.2 shows the simulated EA spectrum over 40 strips. There are 3 distinct peaks with magnitudes greater than 6 dB at 1450 Hz, 1951 Hz and 2264 Hz and thus 3 frequencies where the signal is enhanced. The pressure maps for the total sound field over the strips at these frequencies are displayed in figure 6.5. They show periodically-spaced regions of higher pressure above the tops of the strips associated with high-pressure regions in the gaps between the strips.

In the simulated EA spectrum (figure 6.4) for 23 strips, there are 4 distinct peaks with magnitudes greater than 6 dB at 1132 Hz, 1450 Hz and 1682 Hz and 1857 Hz, denoted as (a), (b) and (c), respectively. At these frequencies, the pressure contour maps (figure 6.6), again show periodically-spaced regions of higher pressure above the tops of the strip array associated with high pressure regions in the gaps between the strips. These high-pressure regions are thought to originate in quarter-wavelength resonances in the gaps between strips which then interact above the strip tops. It is possible to calculate the quarter-wavelength resonant frequencies associated with each strip gap by assuming that the gap is acting as an ‘organ pipe’ closed at one end. This detailed in the following section. It can safely be assumed that the surface wave frequency is 1450 Hz since this enhancement feature does not depend on the gap between strips. The reduction in magnitude of the surface wave for a larger gap is a result of a reduction in the imaginary component of the effective impedance.

6.3 Quarter Wavelength Resonators

Quarter-wavelength resonators, such as organ pipes, have different resonant frequencies depending whether they have one end closed end or are open at both ends. At an open end,

the air particles have a velocity antinode (pressure node) and at a closed end, there is no particle displacement which corresponds to a velocity node (pressure antinode). Assumptions made to obtain standing wave solutions for such a pipe-resonator, are that the walls of the resonator are rigid, the air-particle motion is parallel with the length of the resonator edges and that the cross-sectional area of the resonator is small compared to the wavelength of the sound travelling within the pipe [34]. The one-dimensional wave equation can be written as,

$$\cdot \frac{\partial^2 \varphi}{\partial x^2} = \frac{1}{c^2} \frac{\partial^2 \varphi}{\partial t^2} \cdot \tag{0.85}$$

The solutions for the potential φ of the incident and reflected waves, φ_1 and φ_2 respectively, from each end are,

$$\varphi_1 = a \sin\left[2\pi \left(kx - ft \right) + \alpha \right] \tag{0.86}$$

$$\varphi_2 = b \sin\left[2\pi \left(kx + ft \right) + \beta \right] \tag{0.87}$$

Where a and b are constants, k is the wave number, f is the frequency and α and β are phase constants. A standing wave is generated within the pipe due to the superposition between the incident and reflected waves given by,

$$\varphi = \varphi_1 + \varphi_2 = \left(a + b \right) \sin\left[2\pi kx + \frac{\alpha + \beta}{2} \right] \cos\left[2\pi ft + \frac{\alpha + \beta}{2} \right] \tag{0.88}$$

Two boundary conditions are imposed in order to account for the closed and open ends. There is no displacement of the particles at the closed end so and there is no pressure differential at the open end. These are given by,

$$x = 0 \quad , \quad \varphi = 0 \tag{0.89}$$

$$x = L \quad , \quad \frac{\partial \varphi}{\partial x} = 0 \tag{0.90}$$

Applying 6.5 to 6.4 yields,

$$\sin\left(\frac{\alpha+\beta}{2}\right)\cos\left(\frac{\alpha+\beta}{2}\right)=0 \tag{0.91}$$

$$\frac{\alpha+\beta}{2}=0 \quad , \quad \frac{\alpha-\beta}{2}=\alpha \tag{0.92}$$

The solution and its derivative then become,

$$\varphi=(a+b)\sin(2\pi kx)\cos(2\pi ft+\alpha) \tag{0.93}$$

$$\frac{\partial\varphi}{\partial x}=2\pi(a+b)k\cos(2\pi kx)\cos[2\pi ft+\alpha] \tag{0.94}$$

Applying 6.6 to 6.10 yields the following result,

$$\cos(2\pi kL)=0 \tag{0.95}$$

Since the cosine is an odd function, only the odd harmonics arise in in the pipe,

$$2\pi kL=(2n-1)\frac{\pi}{2} \tag{0.96}$$

Re-arranging yields the final result,

$$L=\frac{(2n-1)\lambda}{4} \tag{0.97}$$

Quarter-wavelength-resonances arise when a pipe length corresponds to odd multiples of the quarter wavelength (λ_{qwr}) of the vibrating source. It is simple to calculate the resonant frequency of a given pipe length,

$$f_{qwr}=\frac{v}{4L} \tag{0.98}$$

However, the measured resonant frequency is often lower than this and thus we must apply an end correction since the pipe appears to be longer than it actually is due to interactions with the air particles beyond the ends of the cavity. Equation 6.14 can be modified to become,

$$f_{qwr} = \frac{v}{4(h+E)} \text{ or } \lambda_{qwr} = 4(h+E) \tag{0.99}$$

where, in this case, v is the sound velocity, $L = h$ is the height of the roughness elements and E is the end correction which depends on the diameter of the pipe. Approximate calculations have been carried out for cylindrical resonators by Lord Rayleigh [56] and Bosquanet [57]. These and other authors [58] state the end correction to be between 0.3d and πd/4 where d is the diameter of the pipe. For the strip setup, the diameter is assumed to be equivalent to the edge-to-edge spacing, a between the strips. The end corrections deduced from the pressure maps above are displayed in table 6.1.

The calculated end correction has been adjusted to fit the observed enhancement frequencies. These results are then compared to the accepted range of end corrections defined above. For the 40 strip array, 0.00534 m < E < 0.0140 m and for the 23 strip array, 0.0190 m < E < 0.0419 m.

From the above, it is possible to calculate the end correction associated with each gap and compare the calculated wavelength in equation 6.15 with that associated with the enhancement features in figures 6.2 and 6.4.

For the 23 strip array, it can be argued that the peak at 1682 Hz corresponds to the lowest 'organ-pipe' resonance since the corresponding end correction is in good agreement with the expected range. For the 40 strip array, the peak at 1951 Hz has an end correction that also agrees with the calculated end correction.

The wavelength of the sound wave at the frequency of interest is compared to the denominator (= λ_{qwr}) in 6.15 in Table 6.1. There is good agreement between the two values

which further indicates that the enhancement features at the frequencies specified above are indeed a result of quarter wavelength resonances arising within the gaps between strips. This is investigated further as a function of the geometry in section 6.3.

40 Strips				23 Strips			
Frequency of EA Peaks (Hz)	**End Correction (E) (m)**	**Wavelength (m)**	**4(h+E) (m)**	**Frequency of EA Peaks (Hz)**	**End Correction**	**Wavelength (m)**	**4(h+E)**
1450	**0.0272**	**0.2228**	**0.2088**	**1450**	**0.0272**	**0.2228**	**0.2088**
1951	**0.0138**	**0.1656**	**0.1552**	**1682**	**0.0200**	**0.1920**	**0.1800**
2264	**0.0084**	**0.1427**	**0.1336**	**1857**	**0.0158**	**0.1739**	**0.1632**

Table 6. 1 *Frequency of EA peaks in BEM-predicted spectra and corresponding end corrections calculated from equation 6.15.*

An interesting feature is the variation of the extent of the high-pressure region above the strips as the gap between them is increased. From figure 6.5, it appears that as the gap is reduced, the high-pressure regions interfere above the strips. This can be seen as a region of increased sound pressure every 3 strips. As the gap is increased for a fixed source-receiver distance, as in figure 6.6, the high-pressure region exists in every gap since there is now less interaction. This is similar to an effect observed in perforated plates where the resonances generated in the holes on the plate interact with each other known as the holes interaction effect (HIE) [39]. This could explain the higher end correction apparent from the pressure maps when the number of edges per wavelength is large.

Furthermore, the pressure maps in figure 6.6 appear to exhibit periodic sequences of higher- and lower-pressure regions within the gaps suggesting that there are two resonances that exist

as a result of the presence of the strip array. The first is the quarter-wavelength resonance within the gaps and the second is thought to be a result either of the finite extent of the array or interference between the surface wave and the direct wave.

6.3.1 Introducing Absorbing Material to the Ends of the Array

To investigate this further, a series of numerical simulations using BEM have been carried out with alterations to the ends of the array in the propagation direction which could possibly reduce this effect through the introduction of absorbing material at the ends of the array. The high- and low-pressure regions exhibit features similar to that of a standing wave envelope modulating itself onto the gap resonances.

If this is the case, it can be reduced or eradicated through the introduction of absorbing material to the ends of the strip array. This is investigated by placing absorbing material in the gaps at the ends of the array, by making the first and last strip totally absorbing, and by introducing a large absorbing wall at the ends of the array. The material simulated at each end is 0.10 m thick fibreglass with a flow resistivity of 50,000 $Pasm^{-4}$ and a porosity of 0.99. This material is known to have good absorption properties over a broadband of frequencies. The geometry used is the same as the case for 23 strips above separated by 0.0534 m with a thickness of 0.0122 m.

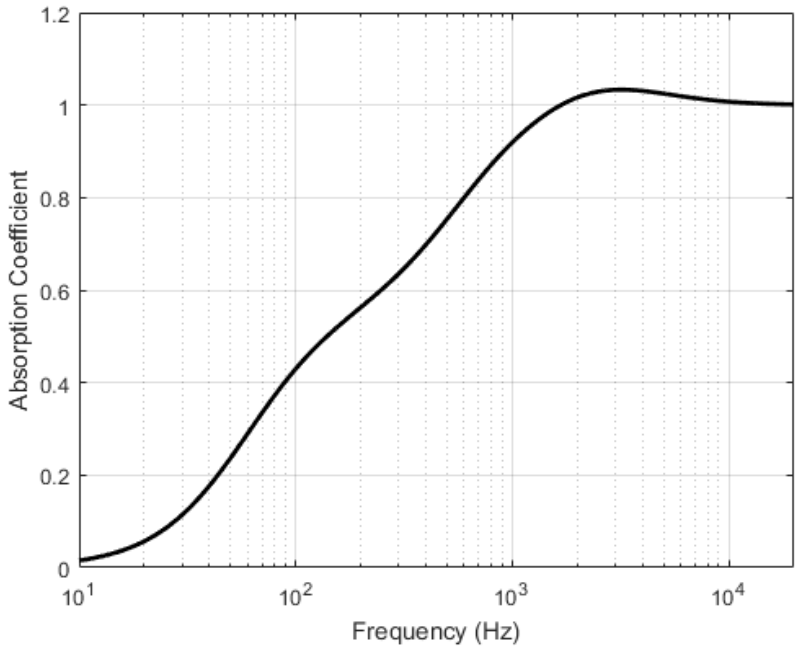

Figure 6. *7 Absorption coefficient for 0.10 m thick fibreglass with a porosity of 0.99 and a flow resistivity of 50000 Pa s* m^{-4}

Firstly, absorbing material was placed in between the gaps at the ends of the array. The geometry was set up so that 50% of the gap was filled with absorbing material since Bashir [32] found that inserting any more than this reduced surface wave generation and, thereby, signal enhancement. In the second case, the last strips at each end were made absorbing and in the final case, the strip height and thickness are both increased to 0.10 m and made absorbing at both ends in order to account for the extent of high-pressure region above the array.

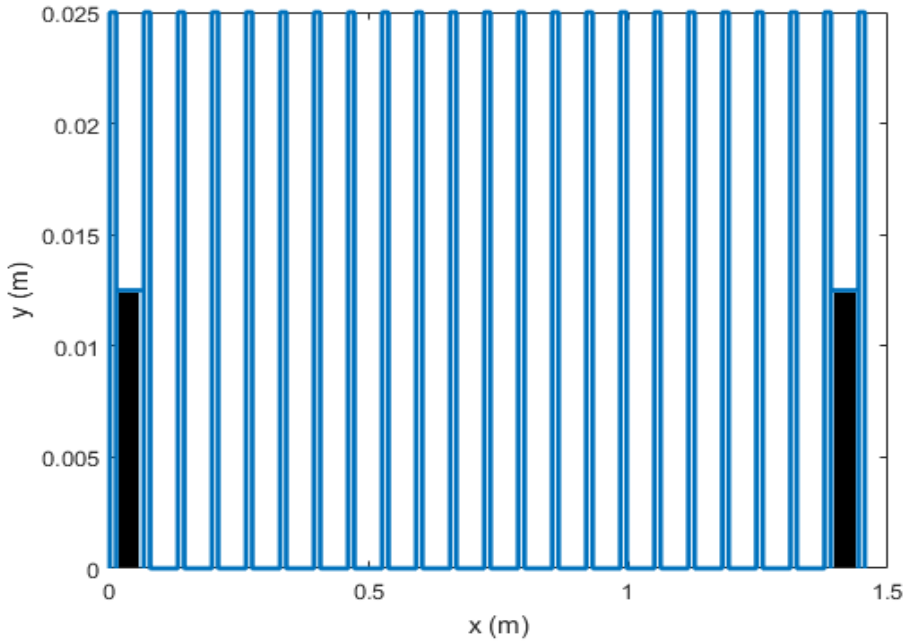

Figure 6. 8 *23 strips of height 0.025 m and thickness 0.0122 m separated by 0.0534 m (blue) with absorbing material placed in between the first and last gap..*

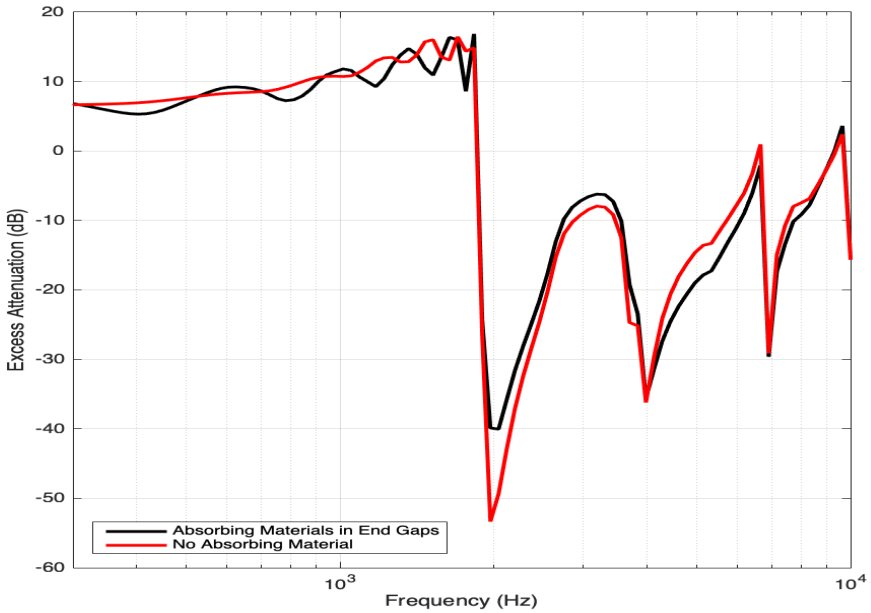

Figure 6. 9 *Excess attenuation spectrum obtained from a BEM simulation of 23 strips of height 0.025 m and thickness 0.0122 m separated by 0.0534 m with absorbing material placed in the first and last gap.*

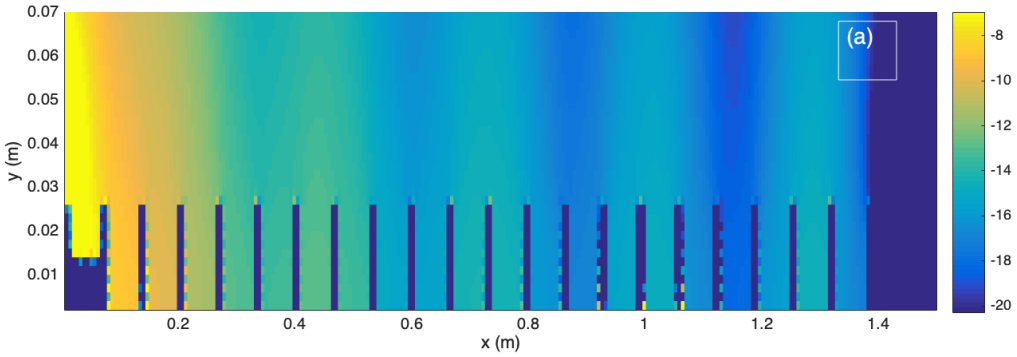
(a)
y (m)
x (m)
0.07
0.06
0.05
0.04
0.03
0.02
0.01
0.2
0.4
0.6
0.8
1
1.2
1.4
-8
-10
-12
-14
-16
-18
-20

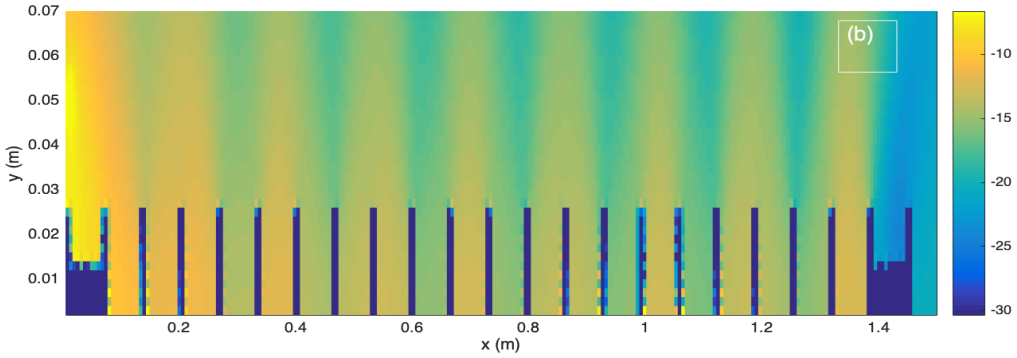
(b)
y (m)
x (m)
0.07
0.06
0.05
0.04
0.03
0.02
0.01
0.2
0.4
0.6
0.8
1
1.2
1.4
-10
-15
-20
-25
-30

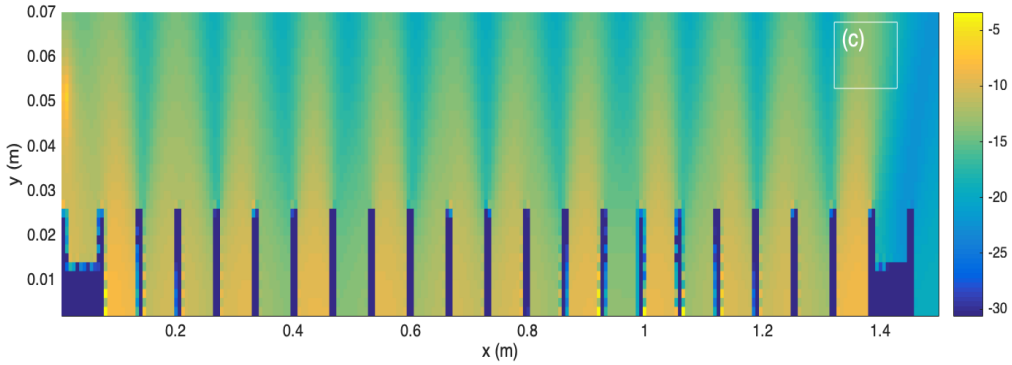
(c)
y (m)
x (m)
0.07
0.06
0.05
0.04
0.03
0.02
0.01
0.2
0.4
0.6
0.8
1
1.2
1.4
-5
-10
-15
-20
-25
-30

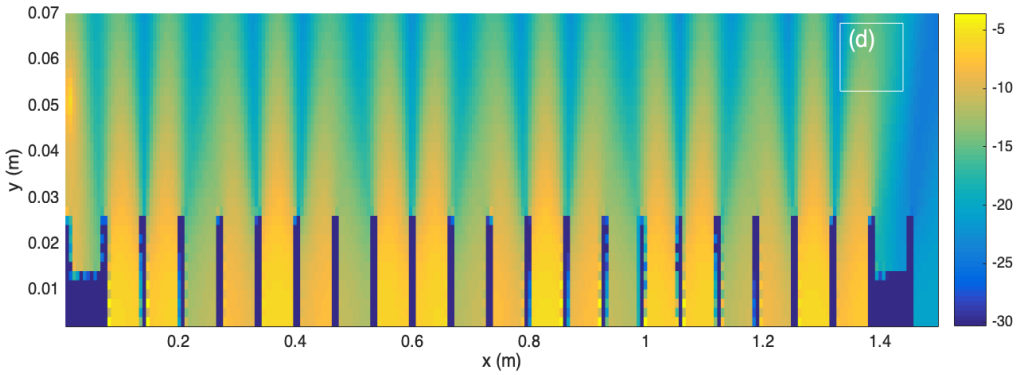
(d)
y (m)
x (m)
0.07
0.06
0.05
0.04
0.03
0.02
0.01
0.2
0.4
0.6
0.8
1
1.2
1.4
-5
-10
-15
-20
-25
-30

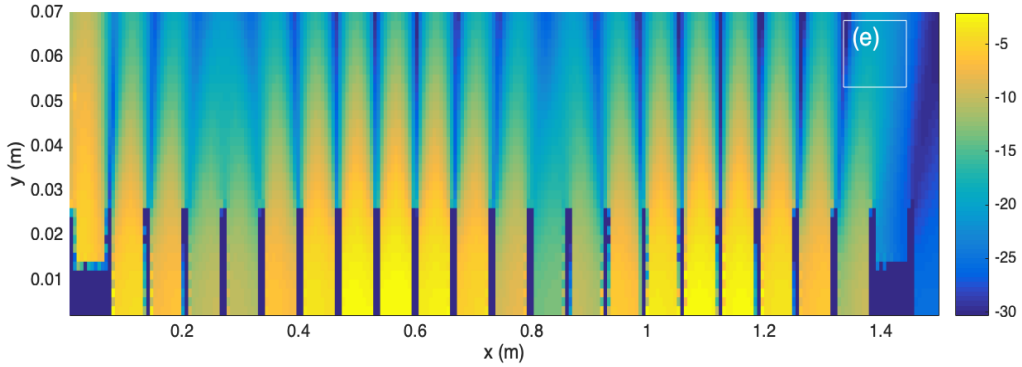

Figure 6. 10 *Total pressure field generated over 30 periodically-spaced rectangular strips with absorbing material in the first and last gaps at* ***(a)*** *605 Hz,* ***(b)*** *1014 Hz,* ***(c)*** *1363 Hz,* ***(d)*** *1639 Hz and (e) 1831 Hz.*

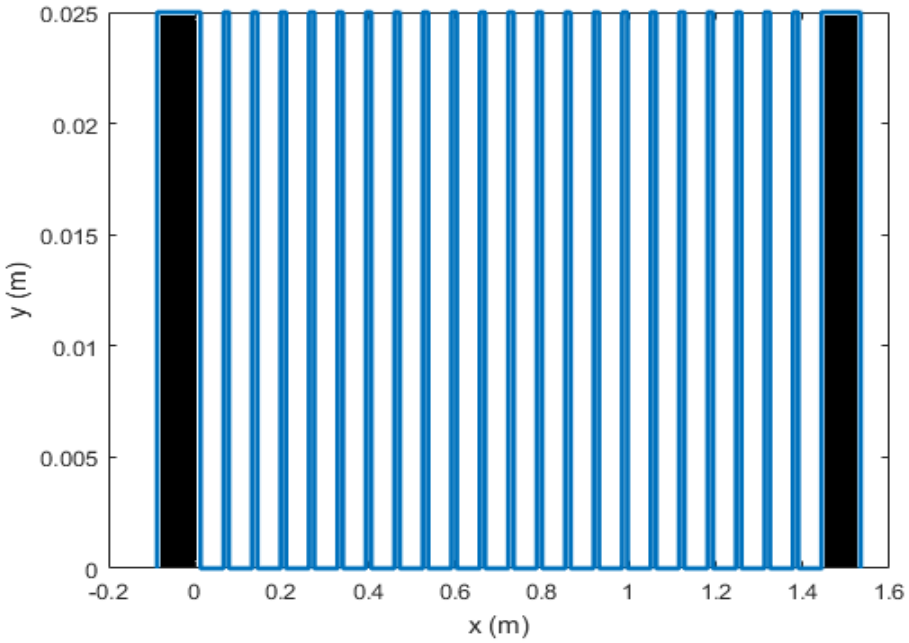

Figure 6. 11 *23 strips of height 0.025 m and thickness 0.0122 m separated by 0.0534 m (blue) with the first and last strips made absorbing with increased thickness of 0.100 m.*

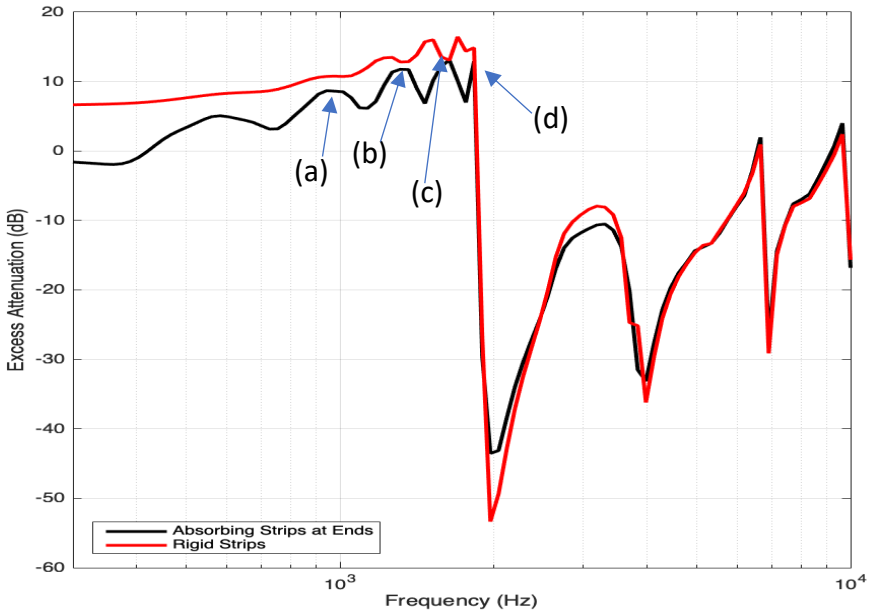

Figure 6. 12 *Excess attenuation spectrum obtained from a BEM simulation of 23 strips of height 0.025 m and thickness 0.0122 m separated by 0.0534 m with the first and last strips made absorbing.*

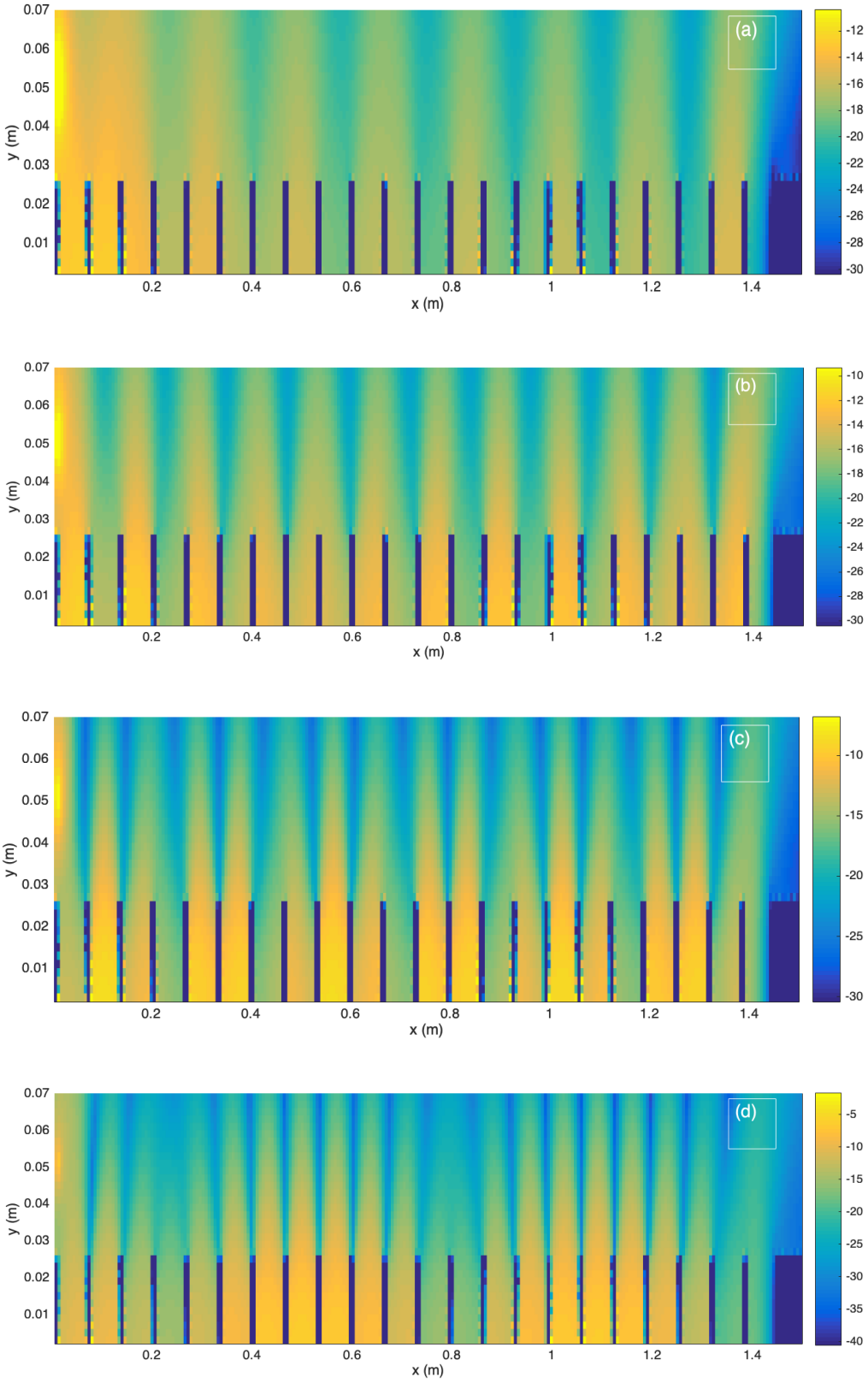

Figure 6. 13 *Total pressure field over 23 periodically-spaced strips with the first and last strip made absorbing at* ***(a)*** *942 Hz,* ***(b)*** *1313 Hz,* ***(c)*** *1639 Hz and* ***(d)*** *1831 Hz.*

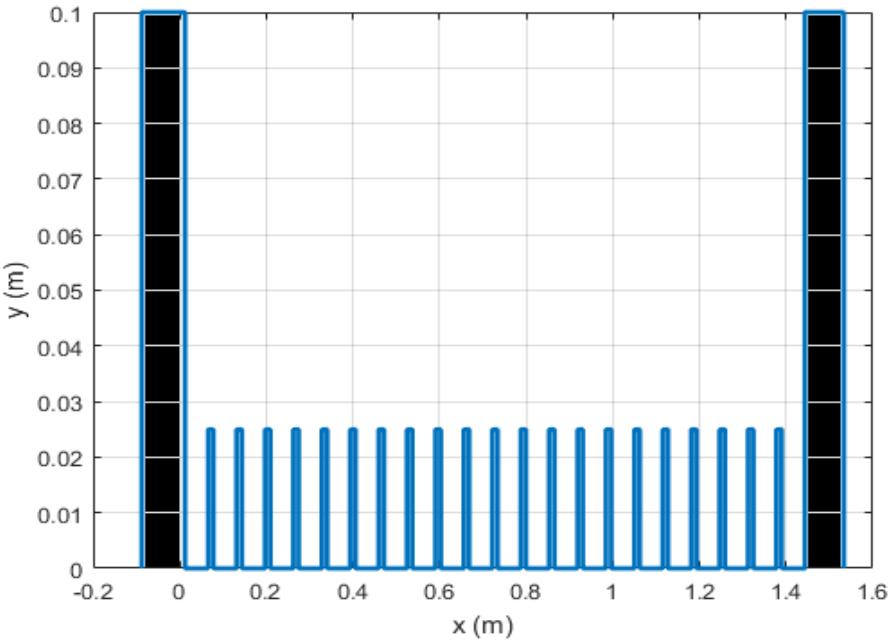

Figure 6. 14 *21 strips of height 0.025 m and thickness 0.0122m separated by 0.0534 m (blue) and the first and last strips made absorbing with increased thickness and height of 0.100 m.*

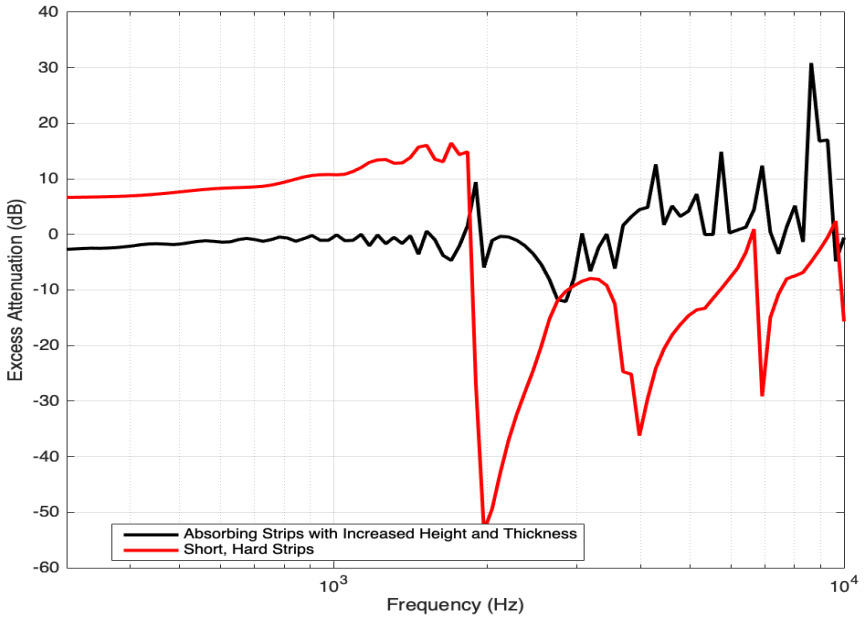

Figure 6. 15 *Excess attenuation spectrum obtained from a BEM simulation of 23 strips of height 0.025 m and thickness 0.0122 m separated by 0.0534 m with the first and last strips made absorbing with increased height and thickness.*

The introduction of absorbing material filling 50% of the gaps at the ends of the array has little effect on the reduction of the enhancement features and the complex pattern observed in the contour pressure maps in figures 6.10. The absorbing material introduces reflections between 300 Hz and 1000 Hz which can be seen as extra peaks in the spectrum in figure 6.9. The same is true for the absorbing strips at the end of the strip array with increased thickness. There is a reduction in the magnitude of the enhancement features and reflections are introduced at lower frequencies. The pressure map in both cases at the peak frequency of 1831 Hz shows strongly coupled resonances in the middle of the strip array but near the receiver, these resonances are reduced as a result of absorption at the ends of the array.
The introduction of a large absorbing wall of height and thickness 0.1 m destroys the signal completely. As seen in figure 6.7, fibreglass is absorbing after 2 kHz which means that the lack of signal observed is due to losses from reflections.
This shows that even with absorbing material at the ends of the array, the patterns of high- and low-pressure regions are still present. In fact, they are made more complex. In figure 6.6 (d), the pattern is a simpler one. Assuming the wavelength associated with this pattern equal to the length of the array in this case of 1.45 m, at a frequency of 1857 Hz, the sound speed is equal to 2692 ms^{-1}. This is highly unrealistic and so the high- and low-pressure regions visible in the pressure maps are not a result of a standing wave generated as a result of the finite length of the array.

6.3.2 Varying Array Periodicity

In this section, the extent to which these effects are a result of periodicity is explored. It has been found in previous work by Bashir [31] that periodically-spaced roughness elements produce stronger surface waves than randomly spaced roughness elements. Thus, it is

expected that randomising the strips will still produce a surface wave but reduce any other enhancement features. Furthermore, the pattern modulated onto the gap resonances has been shown to become more complex when the ends of the array are altered with absorbing material.

BEM simulations have been carried out for a series of 30 strips of thickness 0.0126 m and height of 0.0253 m placed on a rigid surface. The source and receiver were separated by 0.70 m and both placed at a height of 0.04 m above the ground surface. The strips are spaced initially at 0.01 m and shifted to vary the spacings.

Figure 6.17 shows that the surface wave generated over periodic roughness is indeed slightly stronger than that generated by random roughness spacings. There are two distinct peaks beyond the excess attenuation maximum at 2088 Hz and 2293 Hz that are significantly reduced by the variation of the gap between strips. They are not reduced entirely since it is difficult to completely randomise the array. The strip locations have been perturbed but the separation between source and receiver and the small spacing between the strips make complete randomisation difficult. The frequency and frequency range of the excess attenuation maxima are reduced slightly when the strips are randomised suggesting that periodicity affects surface wave magnitude and frequency content.

To check on the expected surface wave frequency content, it is possible to model a periodically-spaced rough surface as a slit-pore impedance layer with rigid backing providing the spacing between roughness elements is within 50% of the height of the roughness elements (or layer depth) [32]. The porosity and flow resistivity associated with the periodic array are calculated using equations 3.48 and 3.49 and have values of $\Omega = 0.44$ and $R_s = 4.9 \times 10^{-8} Pasm^{-4}$ From figure 6.17, it appears that the feature around 1600 Hz is indeed the surface wave frequency since it is predicted over aperiodic strips and above a slit-pore layer with depth equal to the strip height. This supports the idea that the enhancement

features at frequencies above the surface wave frequency range result from the periodic nature of the array.

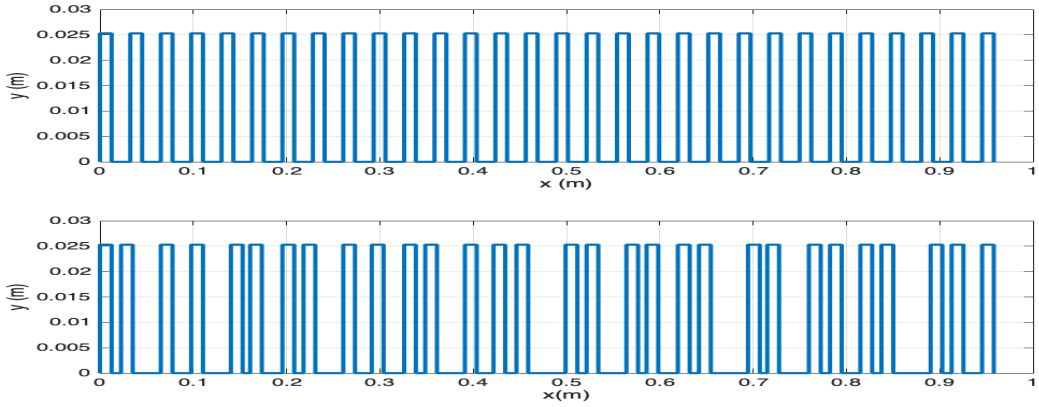

Figure 6. 16 *Strip arrangement for periodic (top) and aperiodic (bottom) arrays of 30 strips.*

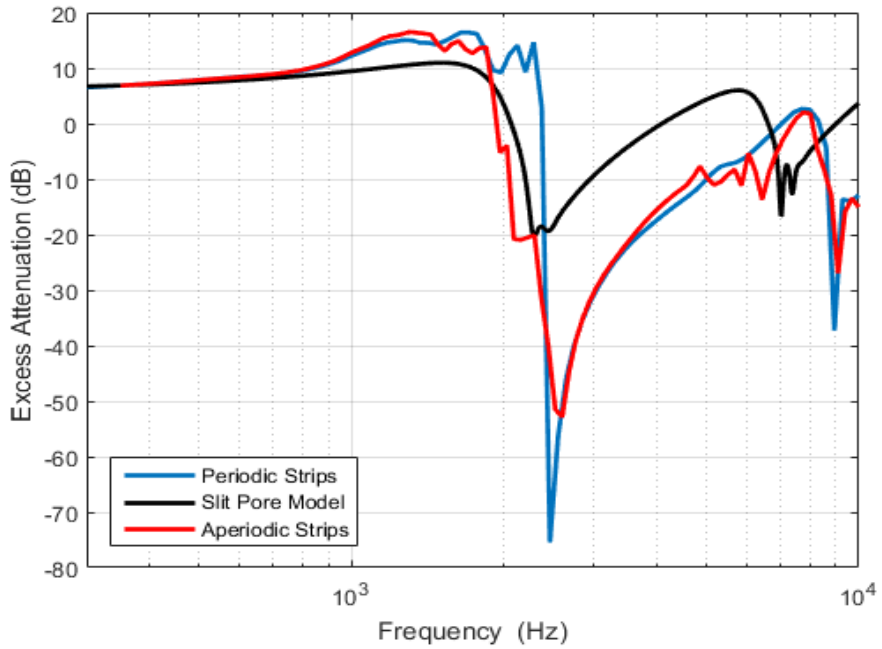

Figure 6. 17 *Excess attenuation spectrum generated using BEM for periodic and aperiodic strip arrays.*

.

To visualise the total sound field over the strips at the frequencies of interest for both periodic and aperiodic arrays, pressure maps can be generated using ContourBEM. The frequencies of interest are displayed in figure 6.18 and are chosen as any peak above 6 dB in the excess attenuation spectrum.

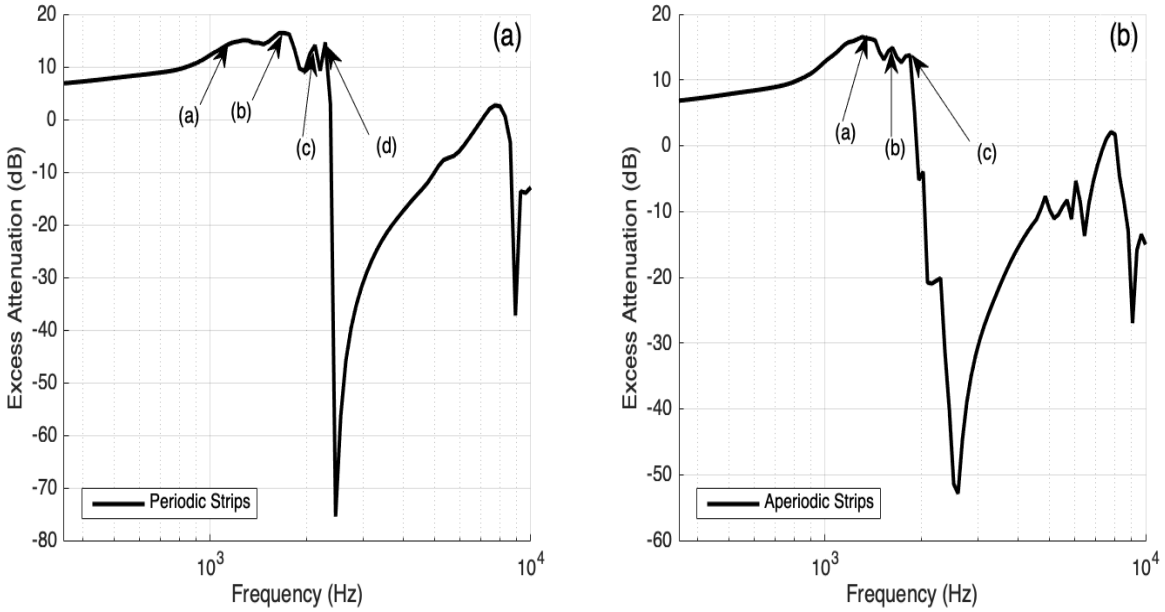

Figure 6. 18 (a) *Excess attenuation spectrum for periodic array of 30 strips separated by 0.01 m* ***(b)*** *Excess attenuation spectrum for aperiodic array.*

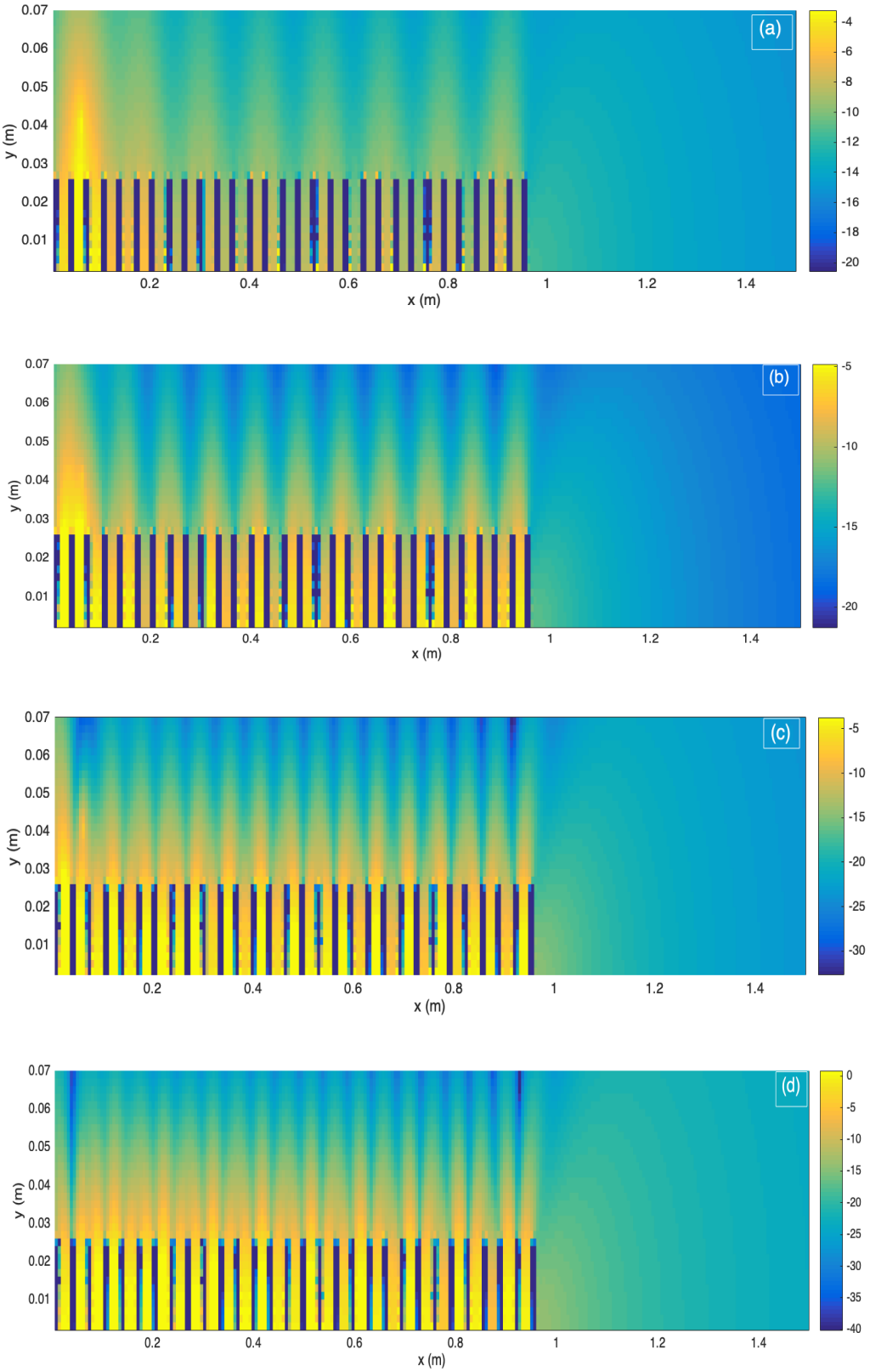

Figure 6. 19 *Total pressure fields predicted over 30 periodically-spaced strips at* ***(a)*** *1305 Hz,* ***(b)*** *1700 Hz,* ***(c)*** *2122 Hz and* ***(d)*** *2284 Hz.*

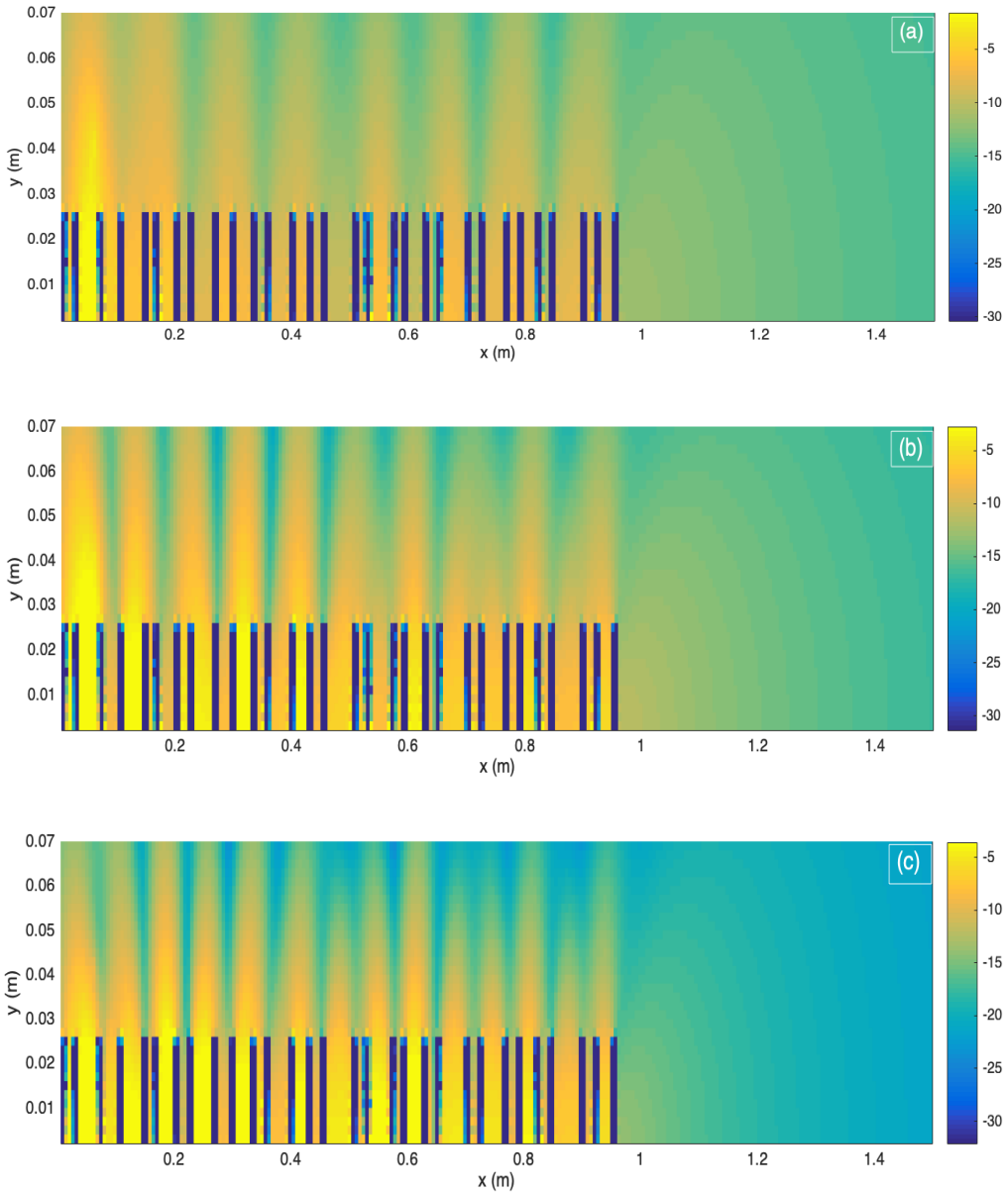

Figure 6. 20 *Total pressure fields predicted over 30 aperiodic strips at* ***(a)*** *1305 Hz,* ***(b)*** *1625 Hz and* ***(c)*** *1842 Hz.*

Figures 6.19 (a) – (d) show the sound field above 30 periodically-spaced strips. There are high-pressure regions above the strip array that originate from quarter-wavelength resonances within the gaps between the strips.

These high-pressure regions are also present at the enhancement frequencies for aperiodic strips. At the peak frequencies, they are coupled strongly which contributes to further enhancement. This surface acts like a slit-pore impedance layer due to the small spacing which implies strong surface wave generation around 1600 Hz. This is further indicated by the broad excess attenuation peak. Gap resonances are still generated but interact less on average due to the variation in gap between the strips.

To further investigate the effect of varying periodicity on the surface wave properties and the pattern modulated onto the gap resonances, two other cases are considered. In the first case, the extent of the array is increased by including extra strips at both ends beyond the source and receiver with decreasing spacing as shown in figure 6.21. The second case involves strips of equal spacing but decreasing height as shown in figure 6.23. Both cases will alter the nature of the impedance discontinuities at the ends of the array and thus the extent of the array.

In both cases, there are 23 strips between the source and receiver separated by 0.0534 m with a thickness of 0.0122 m and a height of 0.025 m. The source and receiver are separated by 1.00 m.

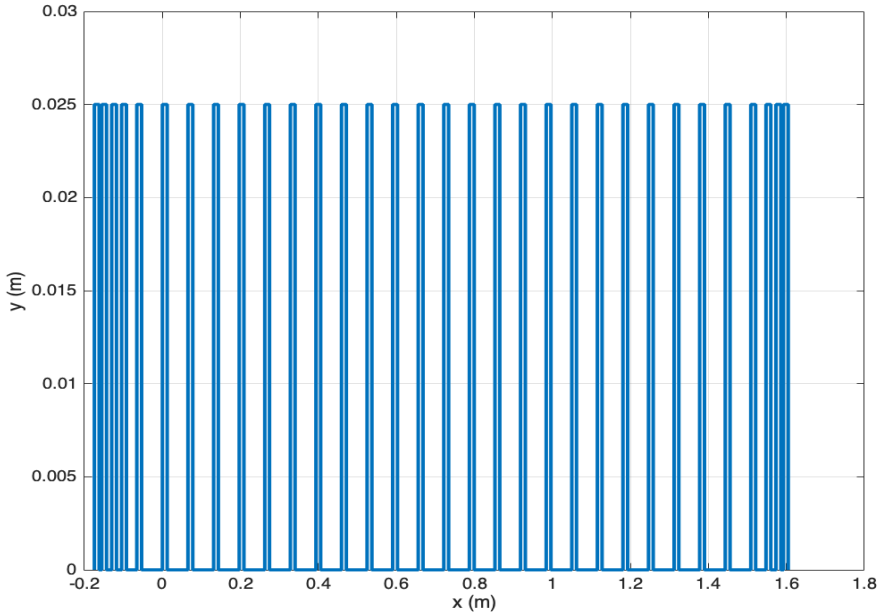

Figure 6. 21 *23 periodically-spaced rectangular strips (blue) separated by 0.0534 m with a thickness of 0.0122 m with 4 strips with decreasing gap at each end.*

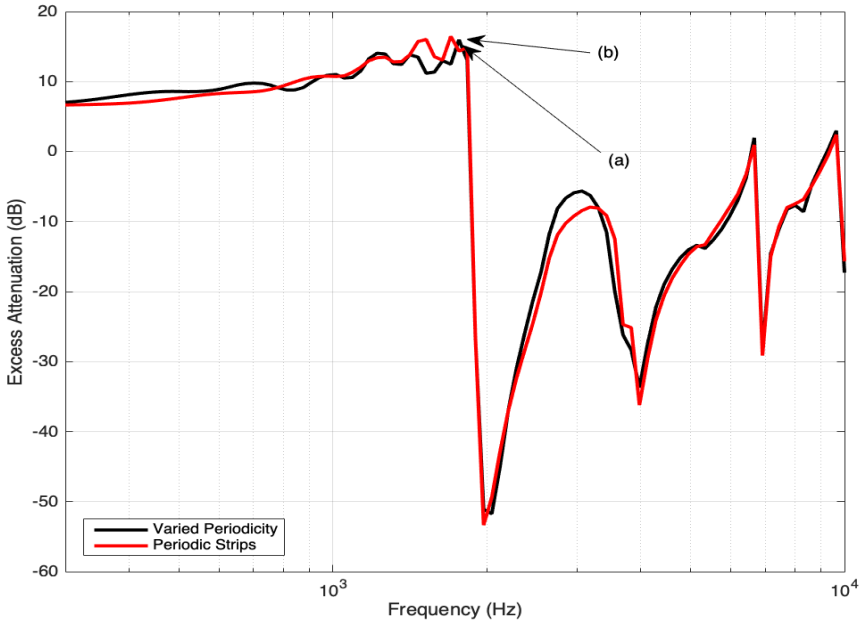

Figure 6. 22 *Excess attenuation spectrum for 23 periodically-spaced rectangular strips spaced by 0.0534 m with a thickness of 0.0122 m and a further 4 strips with decreasing gap at each end.*

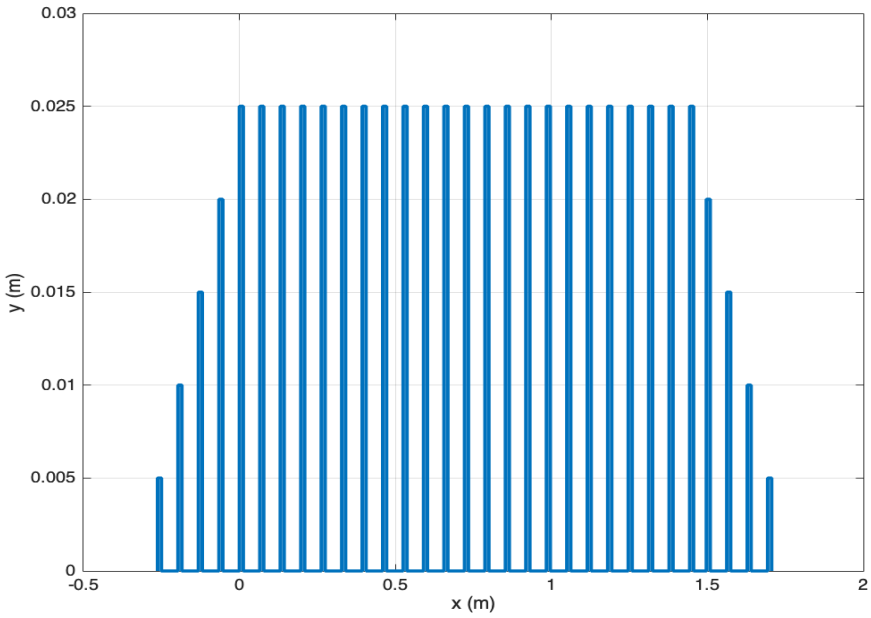

Figure 6. 23 *23 periodically-spaced rectangular strips separated by 0.0534 m with a thickness of 0.0122 m and a further 4 strips with decreasing heights at each end.*

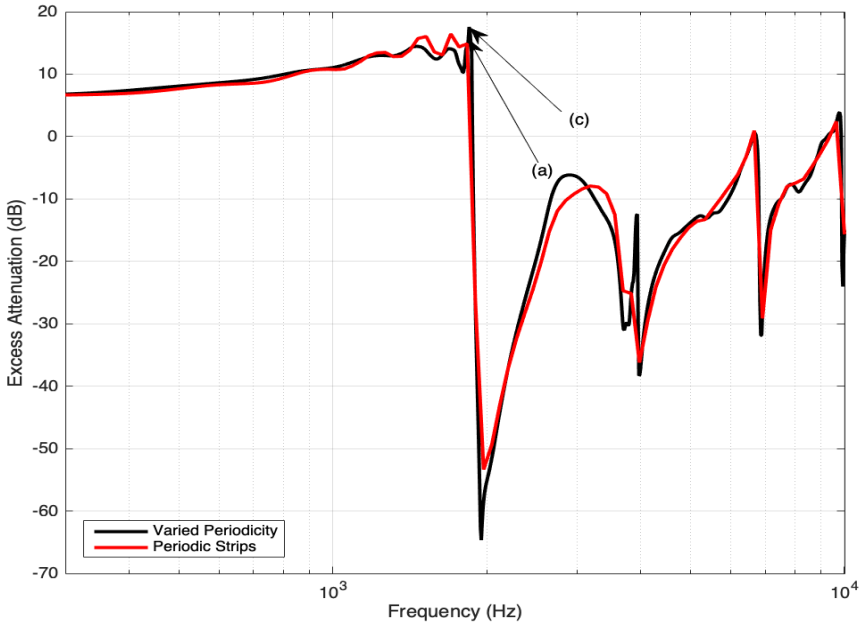

Figure 6. 24 *Excess attenuation spectrum for 23 periodically-spaced rectangular strips spaced by 0.0534 m with a thickness of 0.0122 m and a further 4 strips with decreasing height at each end.*

It is clear from the excess attenuation spectra in figures 6.22 and 6.24 that the introduction of varied periodicity at the ends of the array has little effect on surface wave generation although the surface wave magnitude is reduced slightly. However, there is some increase in the number of excess attenuation peaks which are possibly produced due to variation in the extent of the array. Reflections from the ends of the array contribute to the total signal detected at the receiver and so increasing the length of the array will affect the nature of the excess attenuation maxima.

Pressure maps of the total field over the strip arrays corresponding to figure 6.25 and figure 6.26, generated using ContourBEM, show a change in the sound field above the strips. The complex pattern modulated onto the gap resonances is changed which could arise as a result of interference between waves reflected from the ends of the array due to the impedance discontinuities.

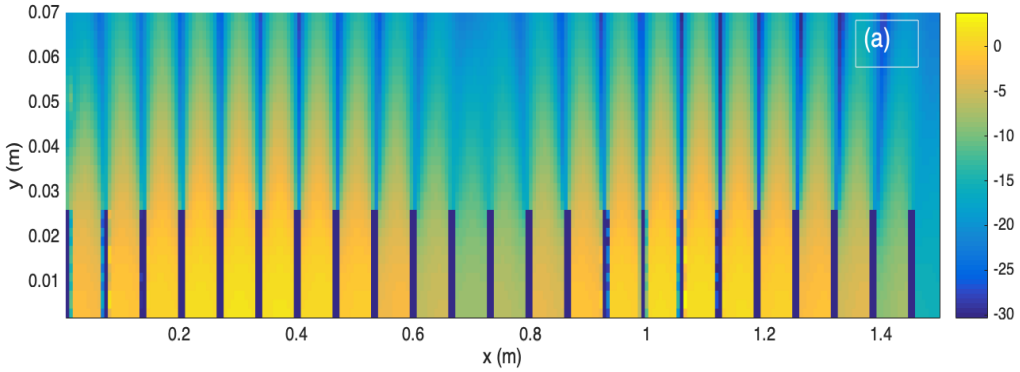

Figure 6. 25 *Total pressure field at 1857 Hz above 23 periodically-spaced strips spaced by 0.0534 m with a thickness of 0.0122 m.*

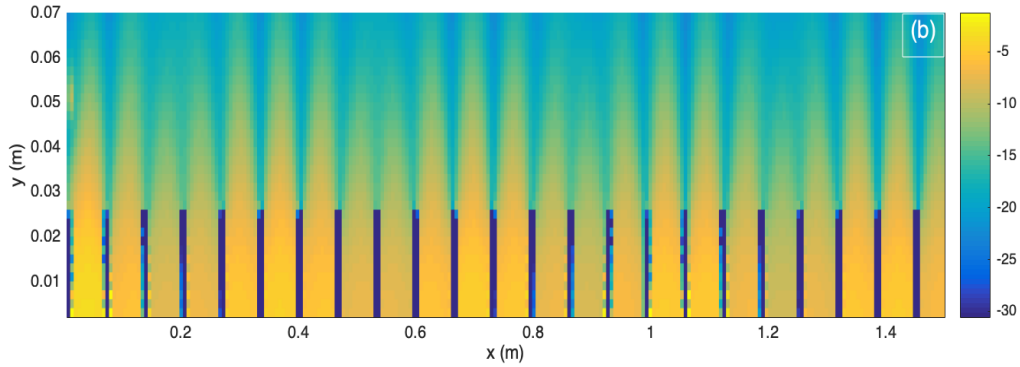

Figure 6. 26 *Total pressure field at 1764 Hz above 23 periodically-spaced strips spaced by 0.0534 m with a thickness of 0.0122 m and further 4 strips of decreasing height at each end.*

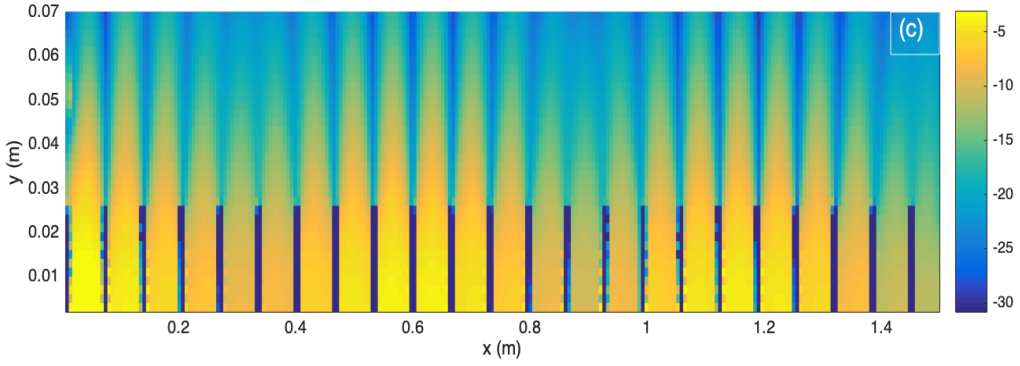

Figure 6. 27 *Total field at 1831 Hz above 23 periodically-spaced strips spaced by 0.0534 m with a thickness of 0.0122 m and a further 4 strips of decreasing height at each end.*

6.3.3 Interference Patterns

The patterns modulated onto the gap resonances in the pressure maps above also resemble interference patterns between the surface wave and other waves such as the direct or reflected waves.

It has been mentioned throughout the literature, and determined experimentally in section 5.3.1, that a surface wave has a reduced phase speed compared with sound in air and so it could be assumed that the interference pattern is a result of interference between two waves of different speed at the frequency of interest. The simplest assumption given the above is that the surface wave is interfering with the direct wave which travels directly between source and receiver.

To determine the surface wave speed, a simple calculation can be carried out assuming the superposition between two waves of equal frequency but differing speeds. Let the two waves, P_1 and P_2 be,

$$P_1 = a_1 \cos\left(\frac{\omega}{c_1} x\right) \tag{0.100}$$

$$P_2 = a_2 \cos\left(\frac{\omega}{c_2} x\right) \tag{0.101}$$

where a_1 and a_2 and c_1 and c_2 are the amplitudes and speeds of the surface wave and the direct wave respectively. The superposition of the two waves yields a new wave P ,

$$P = \cos\left(\frac{\omega x}{2}\left(\frac{1}{c_1} + \frac{1}{c_2}\right)\right)\cos\left(\frac{\omega x}{2}\left(\frac{1}{c_1} - \frac{1}{c_2}\right)\right) \tag{0.102}$$

The second cosine function in equation 6.18 is the envelope function which represents the interference pattern that is modulated onto the gap resonances where the argument is equal to $k_1 x$ where $k_1 = \frac{\omega}{c_1} = \frac{2\pi}{\lambda}$ is the wavenumber associated with the surface wave.

Referring once again to the simple pattern observed figure 6.6 (d) where the wavelength is equal to the length of the strip array, a value for k_1 is easily determined and the argument can be reduced to,

$$\frac{f}{2}\left(\frac{1}{c_1} - \frac{1}{c_2}\right) = \frac{1}{x} \tag{0.103}$$

Where f is the frequency of the wave P and x is the length of the array. The frequency and phase speed of the direct wave are 1857 Hz and 343 ms^{-1} respectively and thus equation 6.19 yields a surface wave speed of $c_1 = 273 ms^{-1}$ This is indeed slower than the phase speed in air. Substitution of this value into equation 6.18 reveals the wave pattern observed in figure 28 (a).

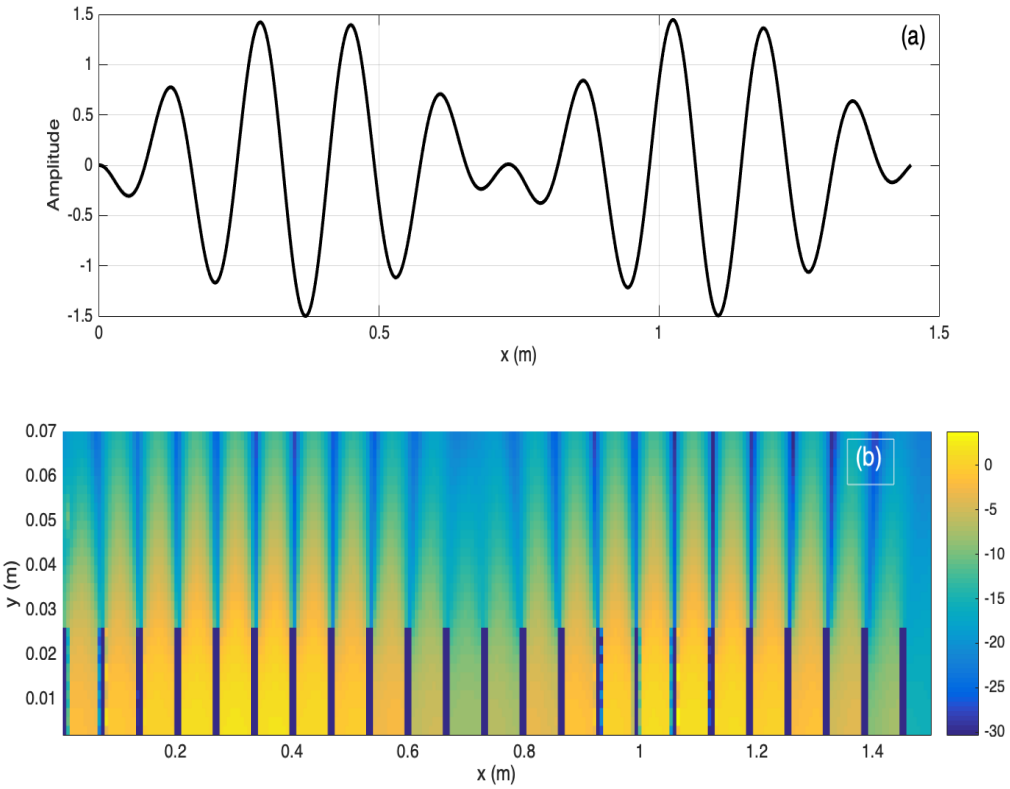

Figure 6. 28 (a) *The resulting wave of the superposition between the direct wave and surface wave, both of frequency 1857 Hz and speeds of 343 ms^{-1} and 273 ms^{-1} respectively* ***(b)*** *Total field over 23 strips at 1857 Hz.*

The resultant waveform exhibited in figure 6.28 (a) strongly resembles that of the interference pattern observed in figure 6.28 (b) (the same as figure 6.6 (d)). The centre of the low-pressure minimum in figure 6.28 (b) lies at a position of x=0.732 m. In figure 6.28 (a), the point of minimum amplitude lies at 0.731 m. This confirms that, at the frequency of 1857 Hz, the low-pressure region observed in the middle of the array is due to interference between the direct wave travelling at 343 ms^{-1} and a surface wave of speed 273 ms^{-1}.

For the more complex patterns observed in figure 6.6 (c), the above method doesn't work. Assuming a wavelength of 0.522 m, the speed of the slower wave interfering with the direct wave is 192 ms^{-1} which is too low.

The peak frequency for the sound field over 40 strips yields the result in figure 6.29 (a). At this frequency, the surface wave has a speed of 272 ms^{-1}, in agreement with the surface wave generated over 23 strips. However, the resonances couple more strongly in this case since the spacing between elements is small.

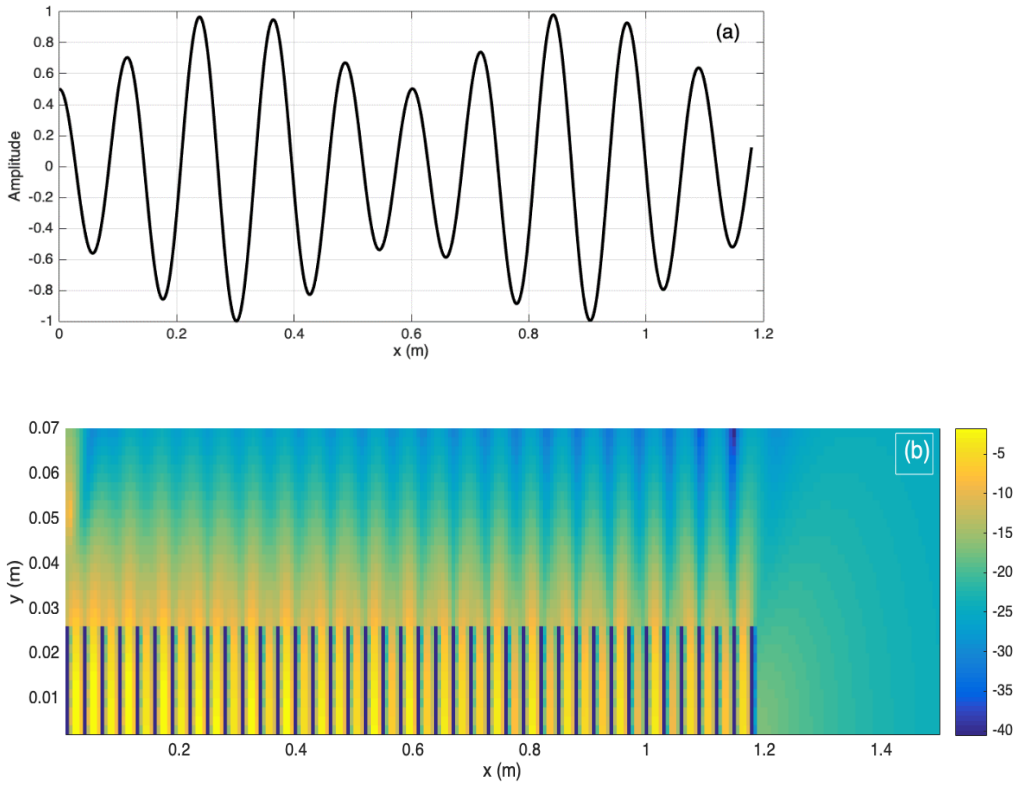

Figure 6. 29 (a) *The resulting wave of the superposition between the direct wave and surface wave both of frequency 2264 Hz and speeds of 343 ms and 272 ms respectively.* ***(b)*** *Total field over 40 strips at 2264 Hz.*

In summary, it appears that many mechanisms contribute to the enhancement of acoustic signals over periodically-spaced rectangular strips.

When there is a high number of edges per wavelength, the surface is closer to a slit-pore impedance layer and so a strong surface wave is generated which is mainly associated with the combination of the vertical motion of the air within the strip gaps (or pore slits) and the horiztontal motion of the incident sound travelling near grazing incidence. There are also extra enhancement features being introduced due to the periodicity and extent of the array as the gap is increased. Once the gap is increased and the number of edges per wavelength is reduced, the surface begins to act more like a rough surface with less interaction between the gap resonances and weaker surface wave generation.

In both cases, at the lowest frequency maxima the organ pipe resonances are weak and there is little evidence of their contribution to surface wave generation. At slightly higher frequencies, the organ pipe resonances become more prominent and increase in magnitude. They also begin to exhibit patterns as a result of spatial interference between the direct wave and the surface wave travelling at different speeds. The interference patterns exhibited in pressure maps of the total field arise as a result of spatial interference between the direct wave and a surface wave of speed 273 ms^{-1} and 272 ms^{-1} for the 23-strip case and the 40 strip case, respectively.

In every case, there will be effects from the finite length of the array which require further investigation. Furthermore, there will be contributions from the waves scattered from the strip edges. These contributions will interfere constructively at the receiver with the direct and surface wave contributions and result in further enhancement.

6.4 Effect of Strip Geometry on Surface Wave Properties

The enhancement features observed in the excess attenuation spectra are thought in some part to be a result of quarter-wavelength resonances that depend on the periodicity and structure associated with the strip array.

This section presents a systematic study on the effect of varying the geometry associated with arrays of periodically-spaced rectangular strips on an acoustically rigid plane. If the geometrical and topographical effects on the enhancement properties are known, then it will be possible to design a periodically rough surface to enhance signals at any desired frequency. The parameters to be varied are,

1. Strip height.
2. Strip thickness.
3. The gap between strips.

Varying the thickness and gap between the strips will vary the number of scattering edges per wavelength between the source and receiver. An experimental study along these lines would have required a range of strip sizes and thicknesses to be available and would have been relatively time-consuming. Since it has been shown to give accurate predictions in chapter 5, this study has been carried out numerically using the Boundary Element Method where parameters can be easily varied. The relevant geometry will be outlined in each section.

6.4.1 Strip Height Variation.

6.4.1.1 Influence on Frequency of First EA Peak

The aim in this set of BEM simulations is to determine the effect of varying the height of the strips on the frequency of the surface wave peak in the excess attenuation spectrum. In this first set of numerical simulations, the height of the strips has been varied between 0.01 m and 0.10 m in increments of 0.01 m. The source is 0.01 m above the top of the first strip and the receiver is at the same height above the array but 0.01 m outside the array. The array consists of 50 strips with the thickness of the strips and the gap between them being fixed at 0.01 m. A small gap is chosen so that the surface is closer to a slit-pore impedance layer and produces a strong surface wave. The length of the array is 0.99 m with the source-receiver separation fixed at 1.00 m. The results are outlined in table 6.2.

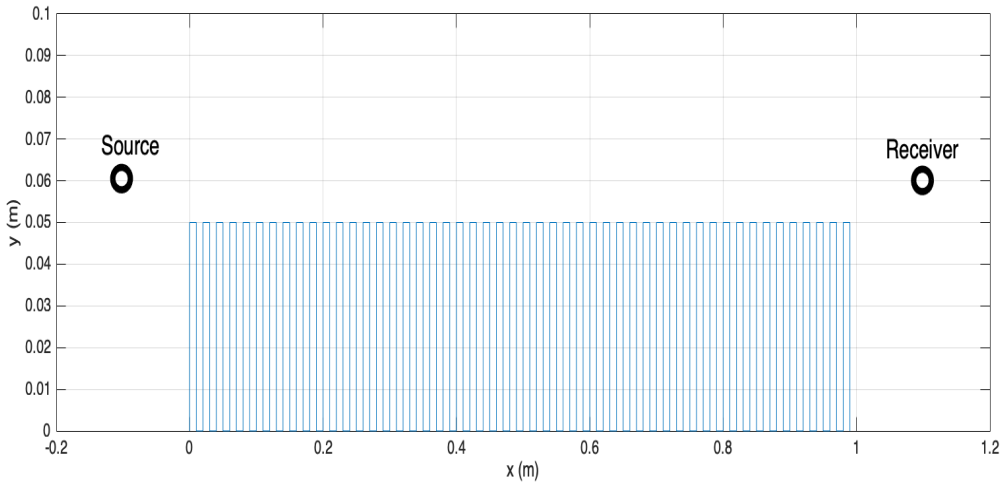

Figure 6. 30 *Diagram of strip setup for a height of 0.05 m showing relative source and receiver positions to strip array.*

Strip Height (m)	Source/Receiver Height (m)	Frequency of First EA Peak (Hz)
0.01	0.02	3638
0.02	0.03	2011
0.03	0.04	1495
0.04	0.05	1153
0.05	0.06	995
0.06	0.07	826
0.07	0.08	767
0.08	0.09	662
0.09	0.10	550
0.10	0.11	511

Table 6. 2 *BEM-predicted variation of frequency of the first EA peak with strip height. The array consists of 50 x 0.01 m thick strips spaced by 0.01 m. The source-receiver separation is 1.00 m.*

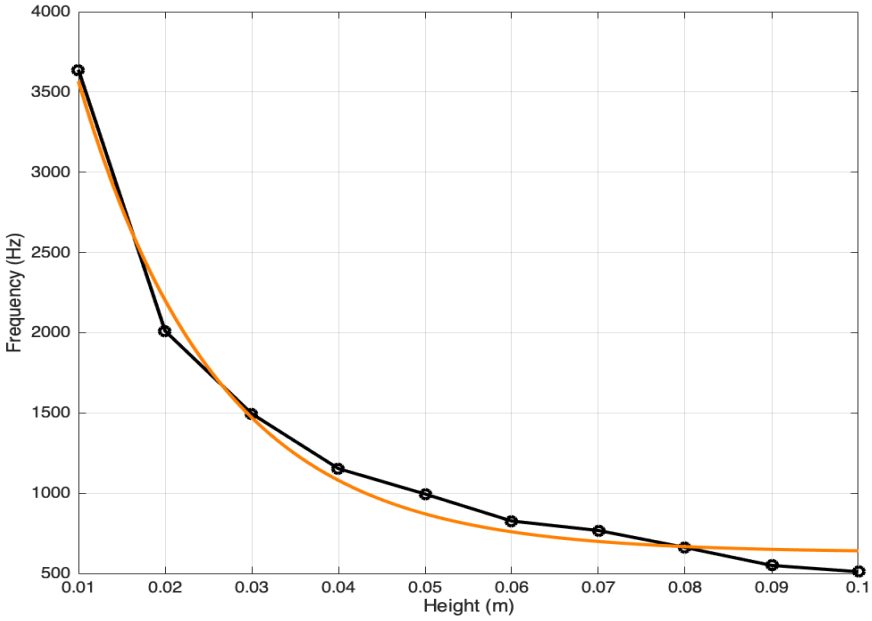

Figure 6. 31 *Frequency of excess attenuation maximum as a function of strip height for 50 strips separated by 0.01 m with a thickness of 0.01 m. The orange curve is an exponential trend line with an R-value of 0.988.*

The frequency, F of the surface wave decreases exponentially with height as,

$$F = ae^{-bh} + c \tag{0.104}$$

where, for the geometry outlined above, $a = 5489.9, b = 62.545, c = 630.27$. It is potentially useful that a 1 m array of narrow grooves of 0.1 m depth can achieve enhancement at as low a frequency as 511 Hz. This also allows for the surface to be manipulated to generated a surface wave at any desired frequency if the strip height is known, However, the predicted exponential relationship with strip height means that it becomes increasingly difficult to amplify low-frequency signals using compact dimensions.

6.4.1.2 Influence on Magnitude of Surface Wave & Vertical Attenuation

The effect of the strip height on the magnitude and vertical attenuation of the surface wave has been studied using an alternative approach. A simple expression for the surface wave is,

$$P_s = P_0 e^{ik_z y} f(x) \tag{0.105}$$

where $f(x)$ is a function that accounts for the horizontal spreading of the surface wave, y is the receiver height and k_z is the z-component of the propagation constant, given by $k_z = k_s + i\alpha$ where α is the attenuation constant in the vertical direction which, for a time dependence of $e^{-i(\omega t - kz)}$, gives phase information and $\mathrm{Im}(k_z)$ gives information on the vertical attenuation above the surface. The term k_s is the surface wave wavenumber.

As mentioned previously, it is possible to model a rough surface as a hard-backed slit-pore layer impedance providing the spacing between roughness elements is less than 50% of the layer depth [32]. Figure 6.17 shows that the slit-pore model predicts only the surface wave contribution so to investigate the variation of surface wave magnitude with strip height, the surface is modelled as a layered slit-pore impedance with rigid backing. The spacing, a and strip width, w were kept constant at 0.005 m and 0.01 m respectively. The porosity, Ω and flow resistivity, R_s can be calculated using equations 3.48 and 3.49 and have values of $\Omega = 1/3$ and $R_s = 26.064$ Nsm^{-4}The source and receiver heights were set at 0.03 m and the source-receiver separation at 1.00 m. The layer depth, equivalent to the strip height, was varied between 0.02 m and 0.10 m in increments of 0.01 m. Once these parameters are

known, the impedance at the enhancement frequency can be used, alongside the wavenumber, in equation 1.3 to calculate the attenuation constant at that frequency.

Layer Depth (m)	**Frequency (Hz)**	**Wavenumber (m^{-1})**	**Attenuation Constant (Np m^{-1})**	**Excess Attenuation at First Peak (dB)**	**Magnitude of First EA Peak (EA-6dB)**
0.02	2023	37.06	13.9904	13.43	7.43
0.03	1461	26.76	12.1646	14.40	8.40
0.04	1150	21.06	10.9066	14.95	8.95
0.05	953	17.46	10.0630	15.28	9.28
0.06	811	14.86	9.1874	15.49	9.49
0.07	710	13.01	8.6784	15.60	9.60
0.08	627	11.49	7.9462	15.67	9.67
0.09	565	10.35	7.5614	15.69	9.69
0.10	512	9.38	7.0590	15.68	9.68

Table 6. 3 *Results obtained from modelling the strip surface with strips of thickness 0.01 m spaced by 0.005 m as as hard-backed slit-pore impedance layer.*

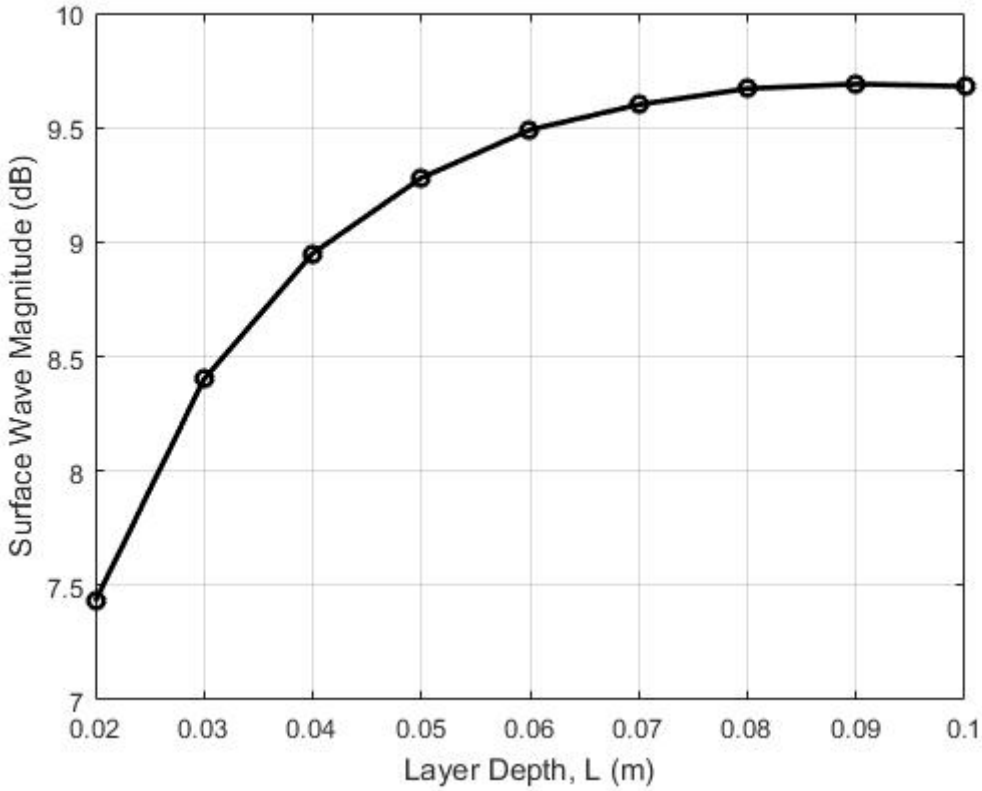

Figure 6. 32 *Surface wave magnitude as a function of layer depth.*

The surface wave magnitude increases rapidly with layer depth but plateaus at a depth of around 0.06 m. This suggests that increasing groove depth or roughness element height will not affect the surface wave magnitude past a certain limit.

The attenuation normal to the slit pore surface is obtained by taking the imaginary part of the vertical propagation constant, k_z . Figure 6.32 shows the vertical attenuation as a function of layer depth.

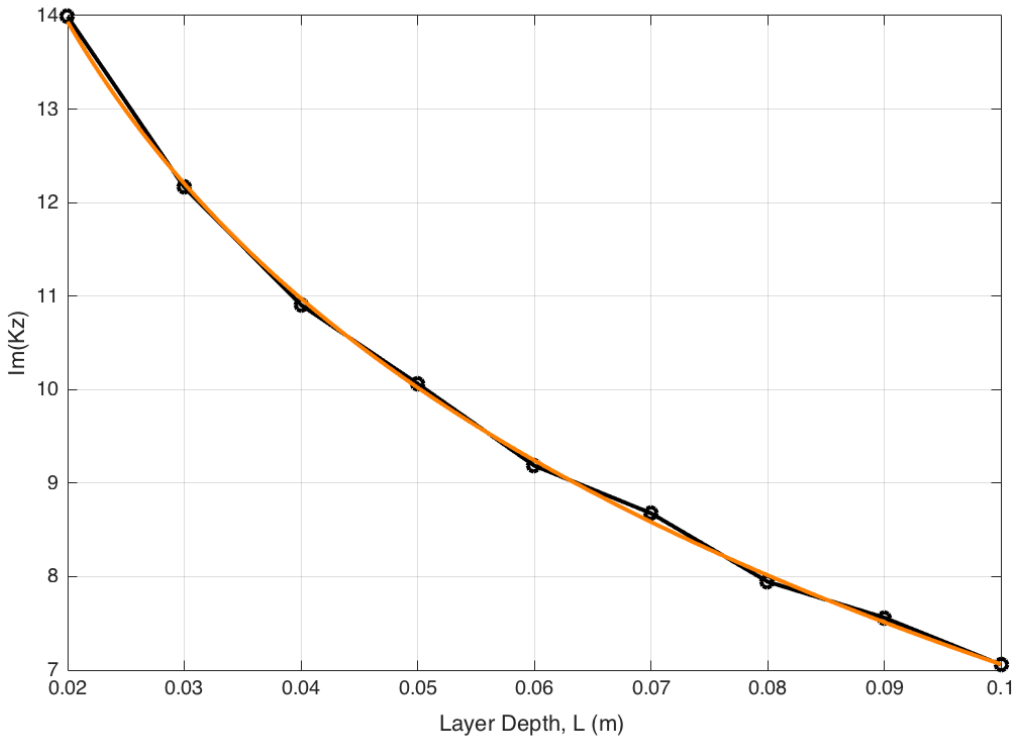

Figure 6. 33 *The imaginary part of the propagation constant as a function of layer depth. The orange trendline has an R-value of 0.99.*

The fitted curve in figure 6.32 has the equation,

$$\mathrm{Im}\left(k_z\right) = a\log\left(bL\right) \tag{0.106}$$

where for the above geometry, $a = -4.2705$ and $b = 1.1933$. These results suggest that the vertical attenuation reduces logarithmically above a slit-pore impedance surface with increasing layer depth. The fact that the surface wave magnitude increases with layer depth agrees with this result since the lower the surface wave frequency, the stronger the surface wave and the less the attenuation.

6.4.2 Strip Thickness & Gap Variation

6.4.2.1 Thickness Variation

The strip thickness is varied using BEM to, again, investigate the effect on the surface wave magnitude and frequency content. The gap between strips was kept constant at 0.01 m and the height of the strips was kept constant at 0.02 m. The thickness of the strips was varied between 0.01 m and 0.10 m in increments of 0.01 m. The source-receiver separation was set at 1 m so the number of strips between source and receiver will inevitably vary. To account for this, the effective porosity of the surface has been plotted as opposed to the thickness. The effective porosity, Ω_{eff} is given by equation 3.48.

As the strip thickness is increased, the number of edges per wavelength between the source and receiver decreases. As the number of elements decreases, the first peak becomes a dominated by the formation of discrete quarter-wavelength resonances within the gaps between the strips. These resonances interact less as the gap is increased. This is discussed further later in this section. The surface wave frequency reaches a peak at a thickness of 0.03 m ($\Omega_{eff} = 0.25$) and then begins to decline rapidly with increasing strip thickness. This is, once again, due to the fact that the number of edges per wavelength between source and receiver is decreasing.

Strip Thickness, w (m)	**Effective Porosity,**	**Number of Strips**	**Frequency (Hz)**	**Excess Attenuation Maximum (dB)**	**Surface Wave Magnitude (EA – 6 dB)**
0.01	0.500	50	2011	12.36	6.360
0.02	0.333	33	2247	10.85	4.850
0.03	0.250	25	2511	9.388	3.388
0.04	0.200	20	2420	7.902	1.902
0.05	0.160	16	2247	7.468	1.468
0.06	0.143	14	2087	5.100	-0.900
0.07	0.125	12	1938	4.779	-1.221
0.08	0.111	11	1734	3.182	-2.818
0.09	0.100	10	1551	2.608	-3.392
0.10	0.099	9	1338	3.147	-2.853

Table 6. 4 *Output of BEM simulation for strips with thickness varied between 0.01 m and 0.10 m separated by 0.01 m with height 0.02 m.. The source- and receiver were separated by 1.00 m.*

.

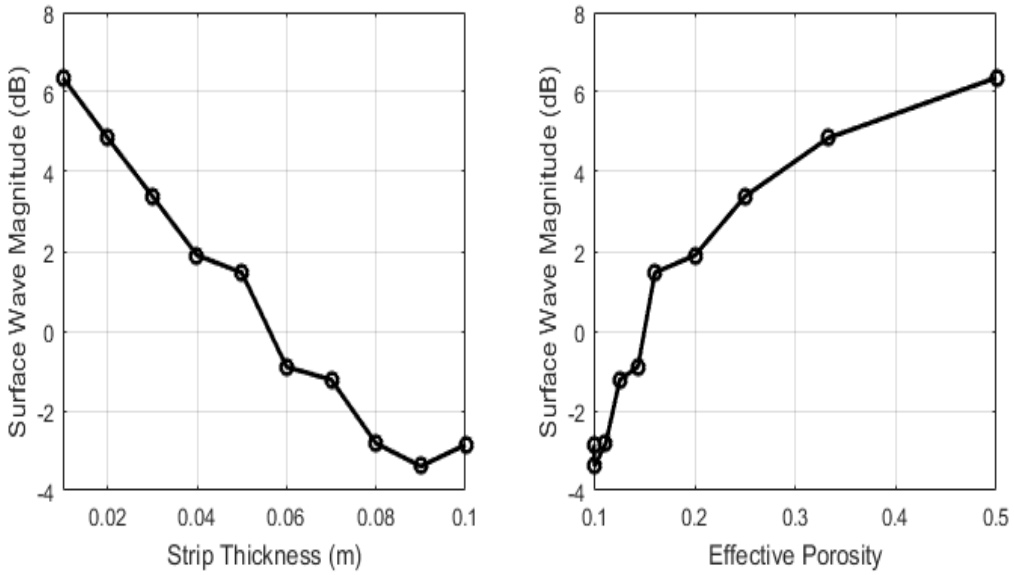

Figure 6. 34 *Surface wave magnitude as a function of strip thickness (left) and the associated effective porosity (right).*

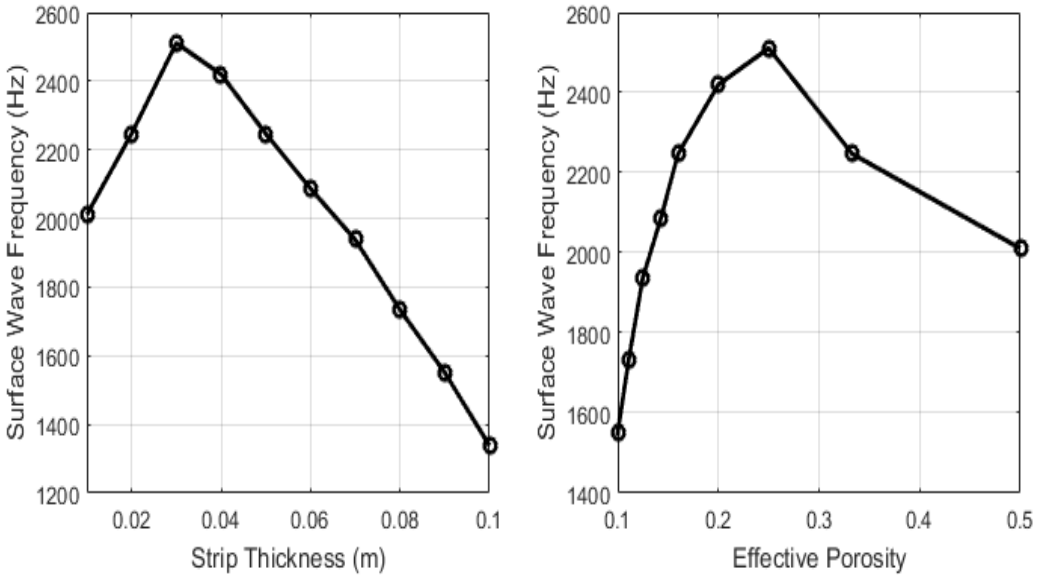

Figure 6. 35 *Surface wave frequency as a function of strip thickness (left) and the associated effective porosity (right).*

The approach detailed above gives a useful method of simply determining the frequency and magnitude of the surface wave generated above any desired geometry. It has been found that the surface wave frequency decrases exponentially with the height of the strips. This highlights the difficulty in enhancing low-frequency signals. Furthermore, the surface wave magnitude increases with strip height (effective layer depth) and figure 6.31 provides a limit to the amount of signal enhancement one can expect from such a surface. These results would be useful if required to enhance acoustic signals within areas where there is limited space.

Another approach taken in this part of the study included BEM calculations in which the gap is varied for a given thickness, allowing for a more detailed investigation of the result in figures 6.33 and 6.34. The strip thickness has been set at 0.005 m, 0.02 m, 0.03 m and 0.04 m with the gap being varied in 0.005 m increments between 0.005 m and 0.10 m. The source and receiver are separated by 1.00 m and the number of strips between them has been calculated from the periodicity which is simply the sum of the gap and the thickness. The strip height was kept constant throughout at 0.02 m.

Further to the excess attenuation output from BEM, the complex pressure output has been input to the TDBEM script. A normalised 4096-point FFT is then calculated for the wave-train that follows the main pulse to obtain the spectra.

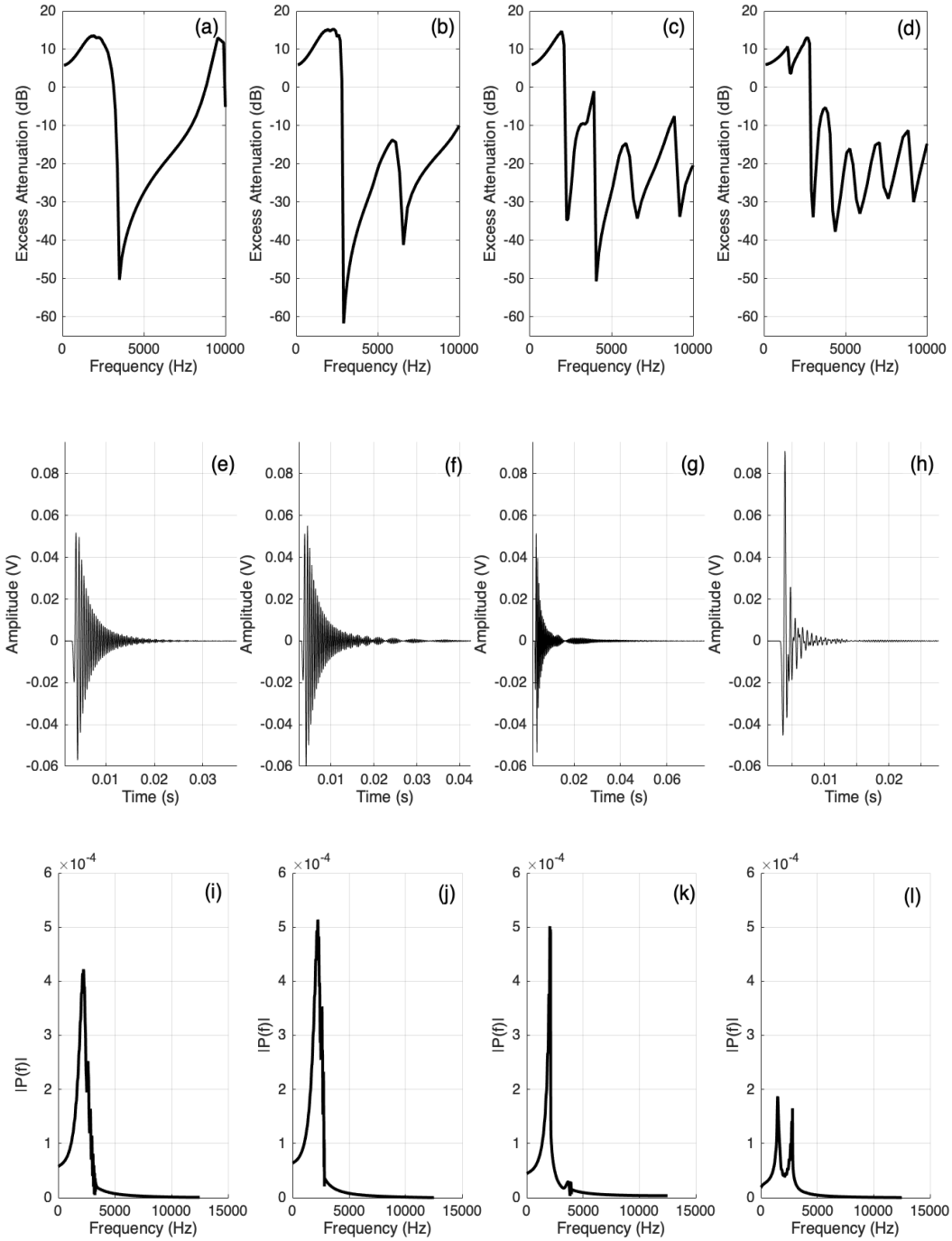

Figure 6. 36 (a) – (d) *Excess attenuation spectra obtained from a BEM simulation over strips with thickness of 0.005 m separated by* ***(a)*** *0.01 m (67 strips),* ***(b)*** *0.03 m (29 strips),* ***(c)*** *0.06 m (16 strips) and* ***(d)*** *0.10 m (10 stirips) with a height of 0.025 m.* ***(e) – (h)*** *TDBEM time-series for the above geometry.* ***(i) – (l)*** *Spectrum of the wave-train following the arrival of the main pulse in figures (e) – (h) obtained via a 4096-point FFT.*

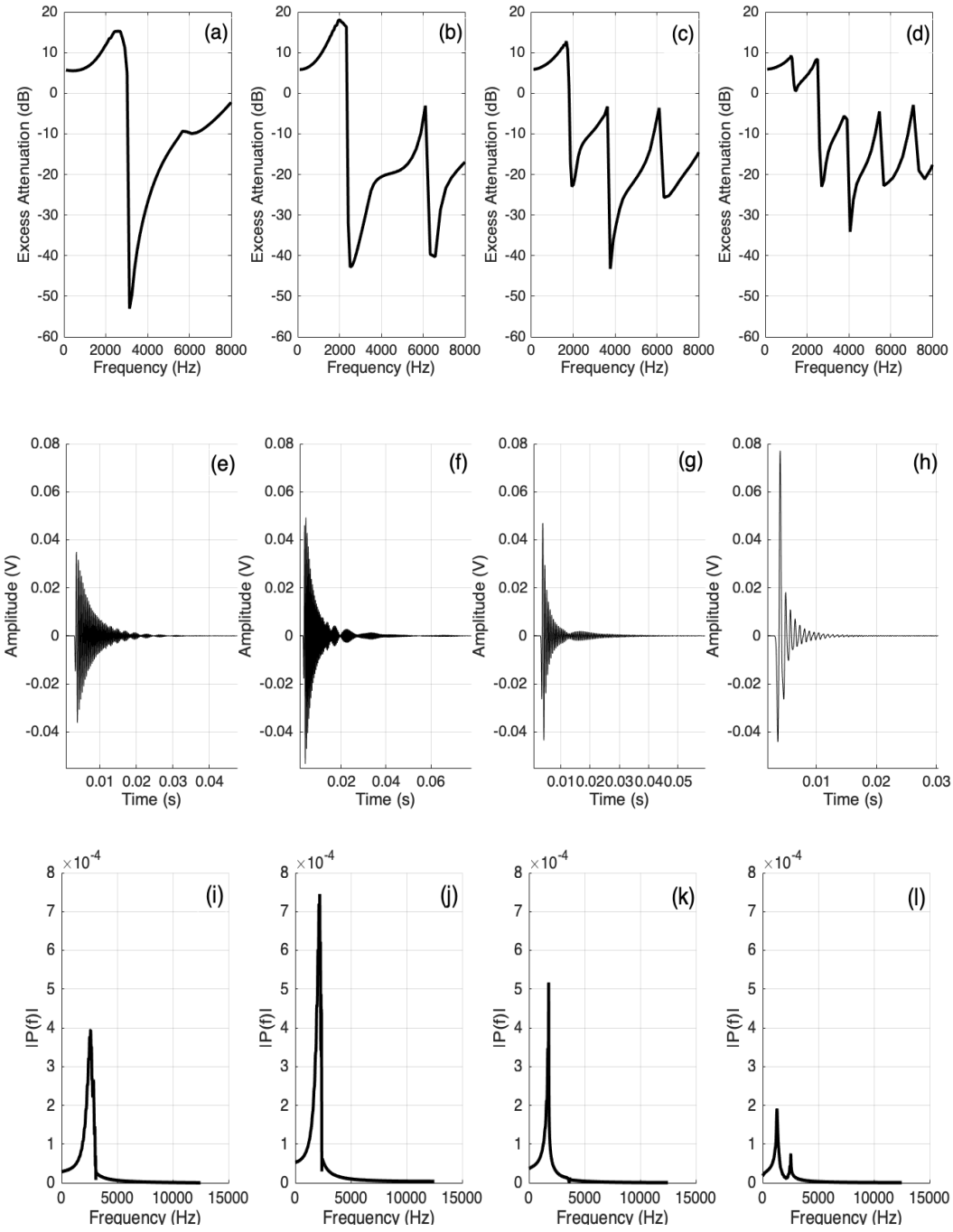

Figure 6. 37 (a) – (d) *Excess attenuation spectra obtained from a BEM simulation over strips with a thickness of 0.02 m separated by* ***(a)*** *0.01 m (34 strips),* ***(b)*** *0.03 m (21 strips),* ***(c)*** *0.06 m (13 strips) and* ***(d)*** *0.10 m (9 strips) with a height of 0.025 m* ***(e) – (h)*** *TDBEM time-series for the above geometry.* ***(i) – (l)*** *Spectrum of the wave-train following the arrival of the main oulse in figures (e) – (h) obtained via a 4096 point FFT.*

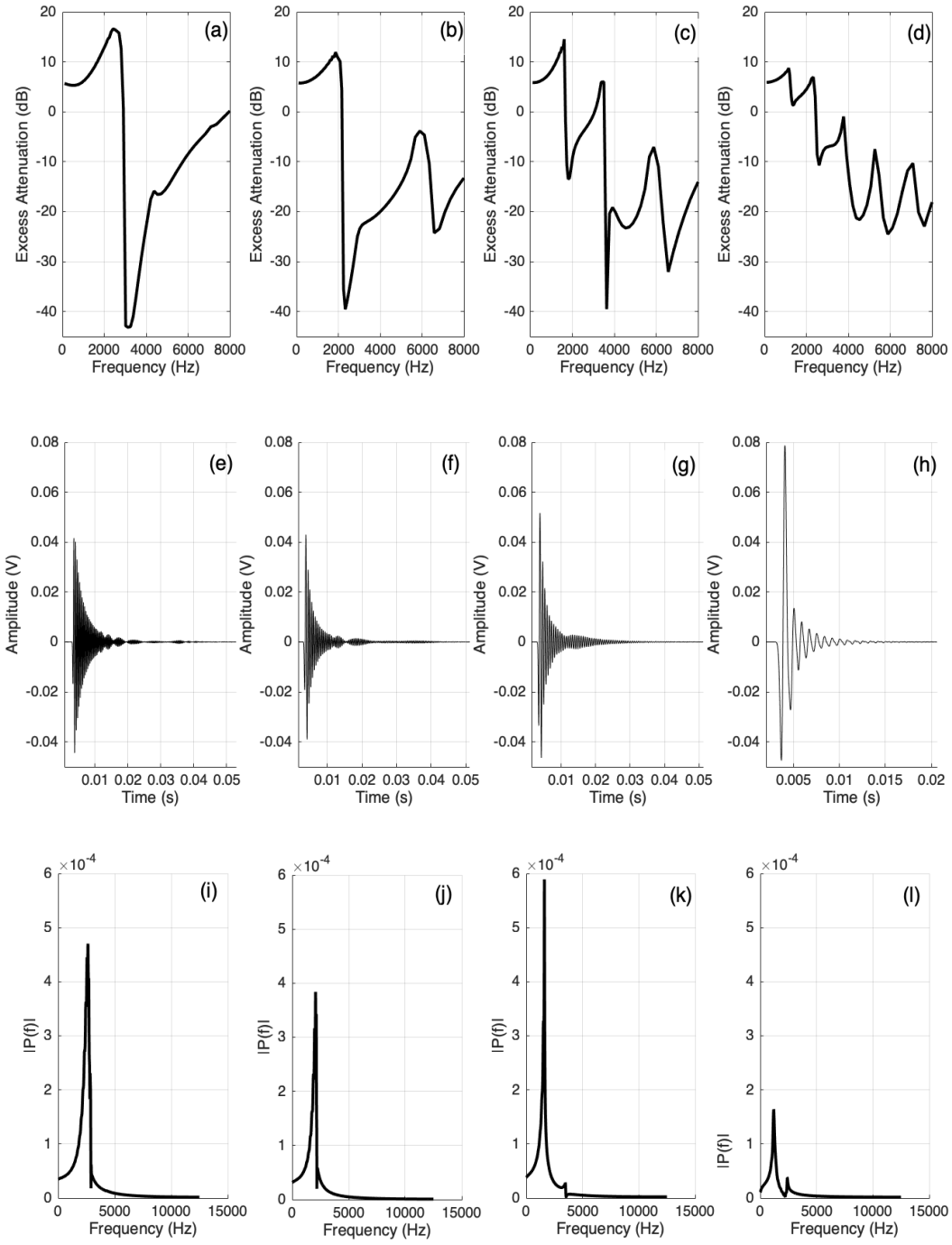

Figure 6. 38 (a) – (d) *Excess attenuation spectra obtained from a BEM simulation over strips with a thickness of 0.03 m separated by* ***(a)*** *0.01 m (26 strips),* ***(b)*** *0.03 m (17 strips),* ***(c)*** *0.06 m (12 strips) and* ***(d)*** *0.10 m (8 strips) and with a height of 0.025 m.* ***(e) – (h)*** *TDBEM time-series for the above geometry* ***(i) – (l)*** *Spectrum of the wave train following the arrival of the main pulse in figures (e) – (h) obtained via a 4096 point FFT.*

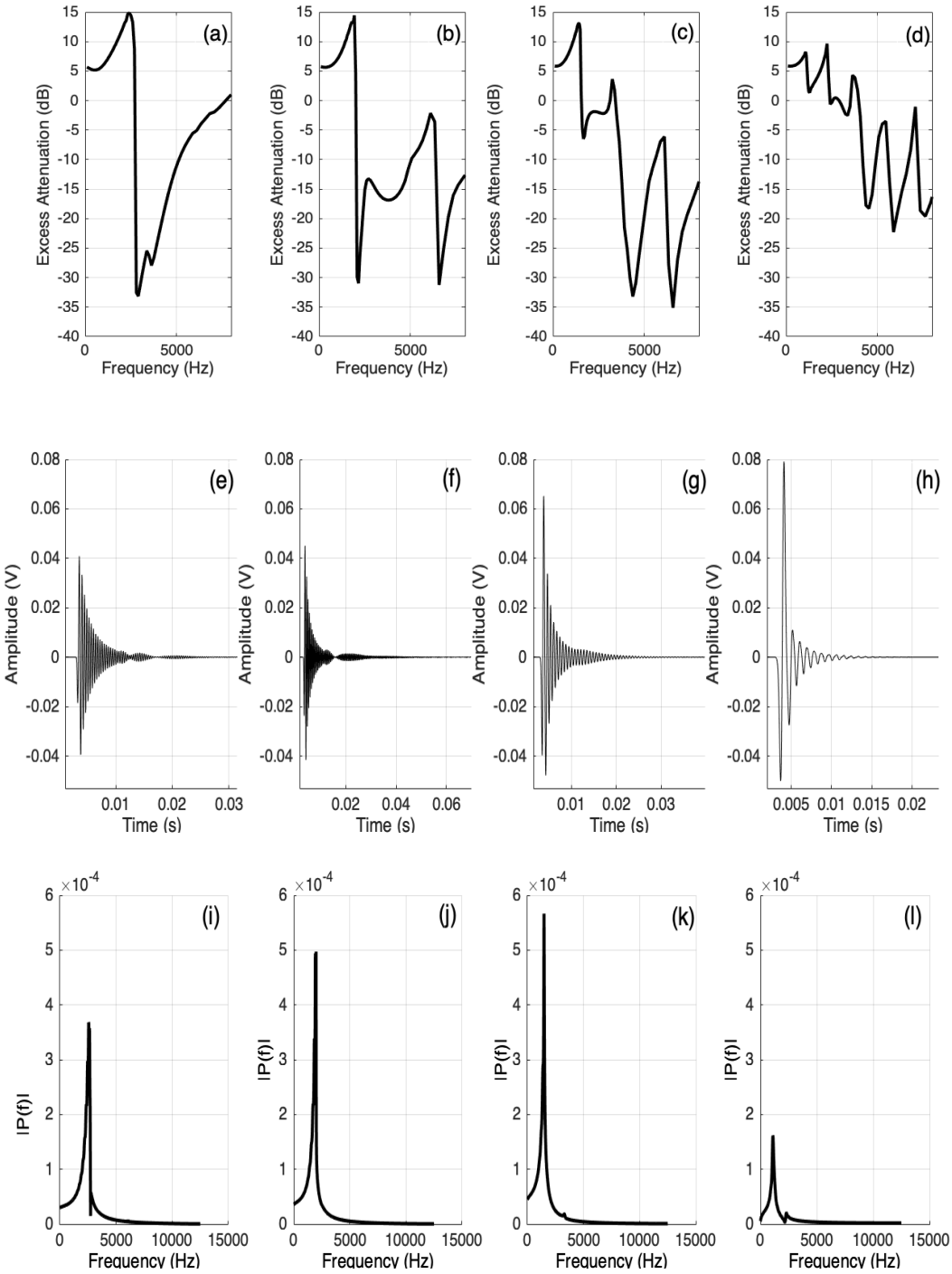

Figure 6. 39 (a) – (d) *Excess attenuation spectra obtained from a BEM simulation over strips with a thickness of 0.04 m separated by* ***(a)*** *0.01 m (21 strips),* ***(b)*** *0.03 m (15 strips),* ***(c)*** *0.06 m (12 strips) and* ***(d)*** *0.10 m (8 strips) and with a height of 0.025 m.* ***(e) – (h)*** *TDBEM time-series for the above geometry* ***(i) – (l)*** *Spectrum of the wave-train following the arrival of the main pulse in figures (e) – (h) obtained via a 4096 points FFT.*

6.4.2.2 Gap Variation

The gap between the strips has been varied between 0.01 m and 0.10 m in increments of 0.01 m using BEM. The thickness of the strips is 0.01 m and the height has been kept constant at 0.02 m although the number of adjacent strips will vary and thus, once again, the effective porosity is used to account for this.

Gap Between Elements, g (m)	**Effective Porosity,** Ω_{eff}	**Number of Elements**	**Frequency (Hz)**	**Excess Attenuation Maximum at First Peak (dB)**	**Magnitude of First EA Peak (EA-6dB)**
0.01	0.500	50	2011	12.36	6.360
0.02	0.666	34	2420	15.38	9.380
0.03	0.750	25	2087	14.93	8.930
0.04	0.800	20	2087	15.26	9.260
0.05	0.833	17	1938	14.64	8.640
0.06	0.857	15	1799	13.94	7.940
0.07	0.875	13	1799	14.15	8.150
0.08	0.888	12	1551	11.80	5.800
0.09	0.900	10	1495	11.43	5.430
0.10	0.999	10	1388	10.08	4.080

Table 6. 5 *Output of BEM simulation for strips with gap varied between 0.01 m and 0.10 m with thickness 0.01 m and height 0.02 m. The source and receiver are separated by 1.00 m.*

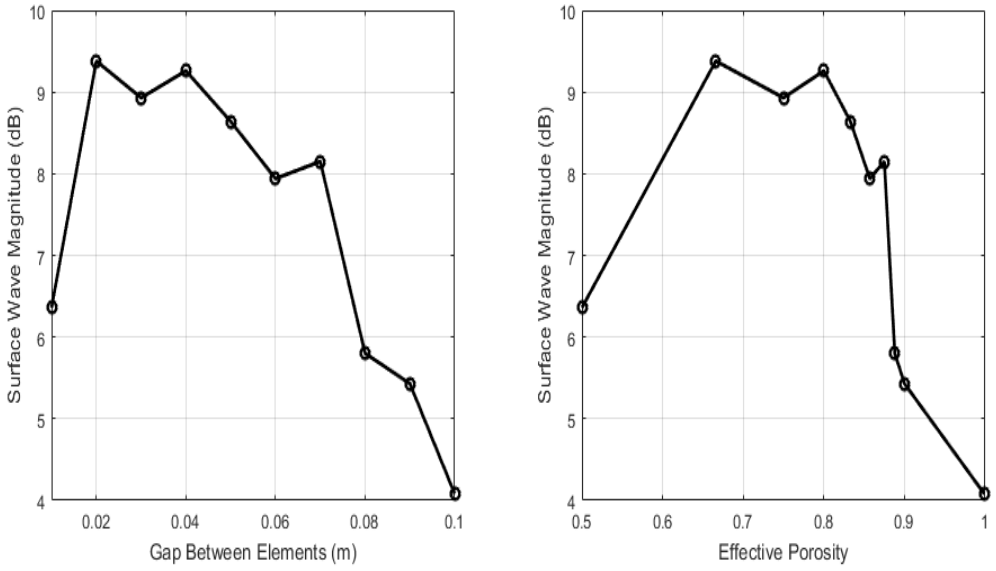

Figure 6. 40 *Surface wave magnitude as a function of the gap between strips (left) and the associated effective porosity (right).*

As before, a second approach has been taken. The thickness was varied between 0.005 m and 0.10 m in increments of 0.005 m. This has been done for strip spacing of 0.005 m, 0.02 m, 0.03 m and 0.04 m. The corresponding excess attenuation spectra, TDBEM time-series and corresponding spectra are shown below.

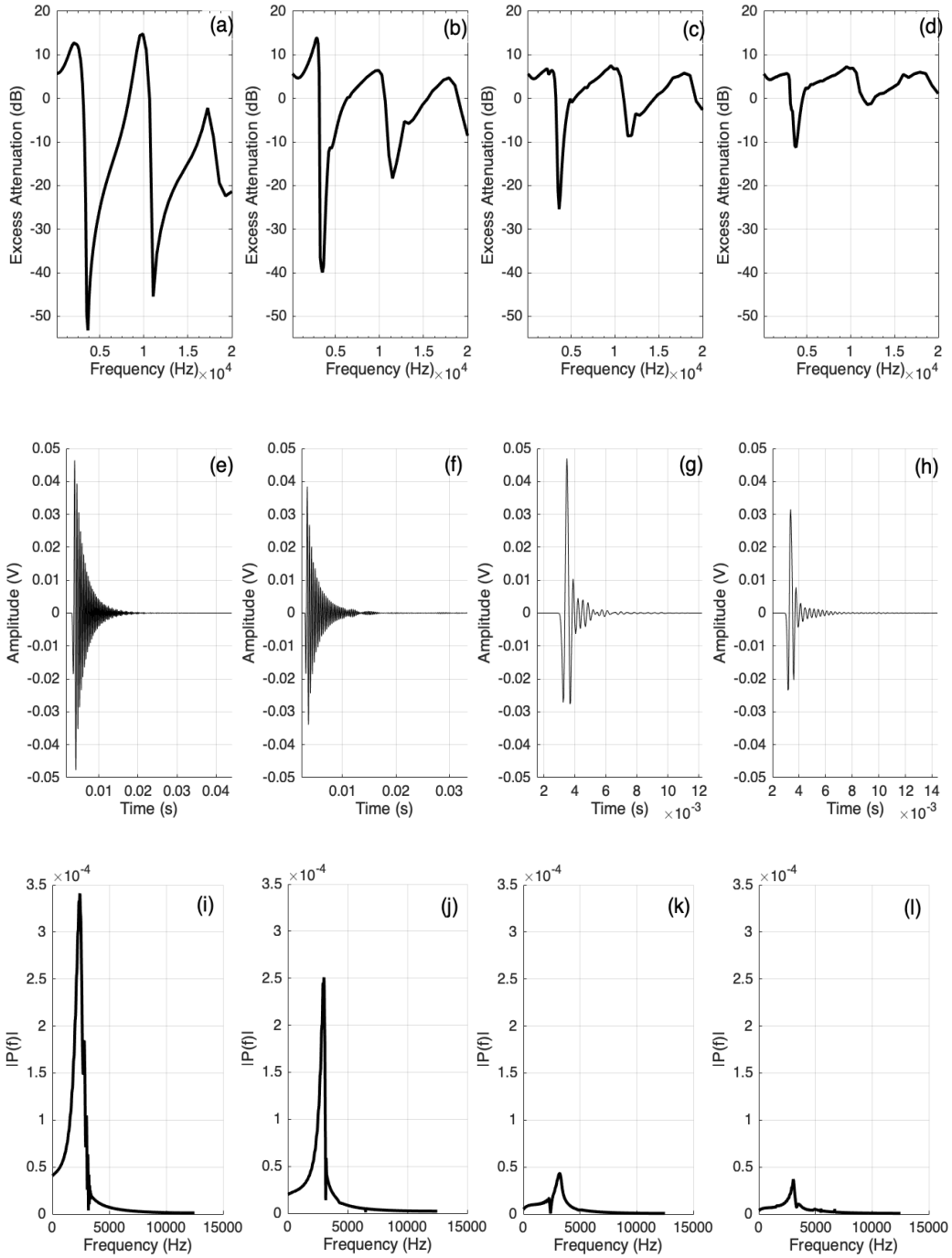

Figure 6. 41 *(**a) – (d)** Excess attenuation spectra obtained from a BEM simulation over strips separated by 0.005 m with a thickness of **(a)** 0.005 m (101 strips), **(b)** 0.035 m (26 strips), **(c)** 0.065 m (15 strips) and **(d)** 0.10 m (10 strips) and with a height of 0.025 m **(e) – (h)** TDBEM time-series for the above geometry **(i) – (l)** Spectrum of the wave-train following the arrival of the main pulse in figures (e) – (h) obtained via a 4096 points FFT.*

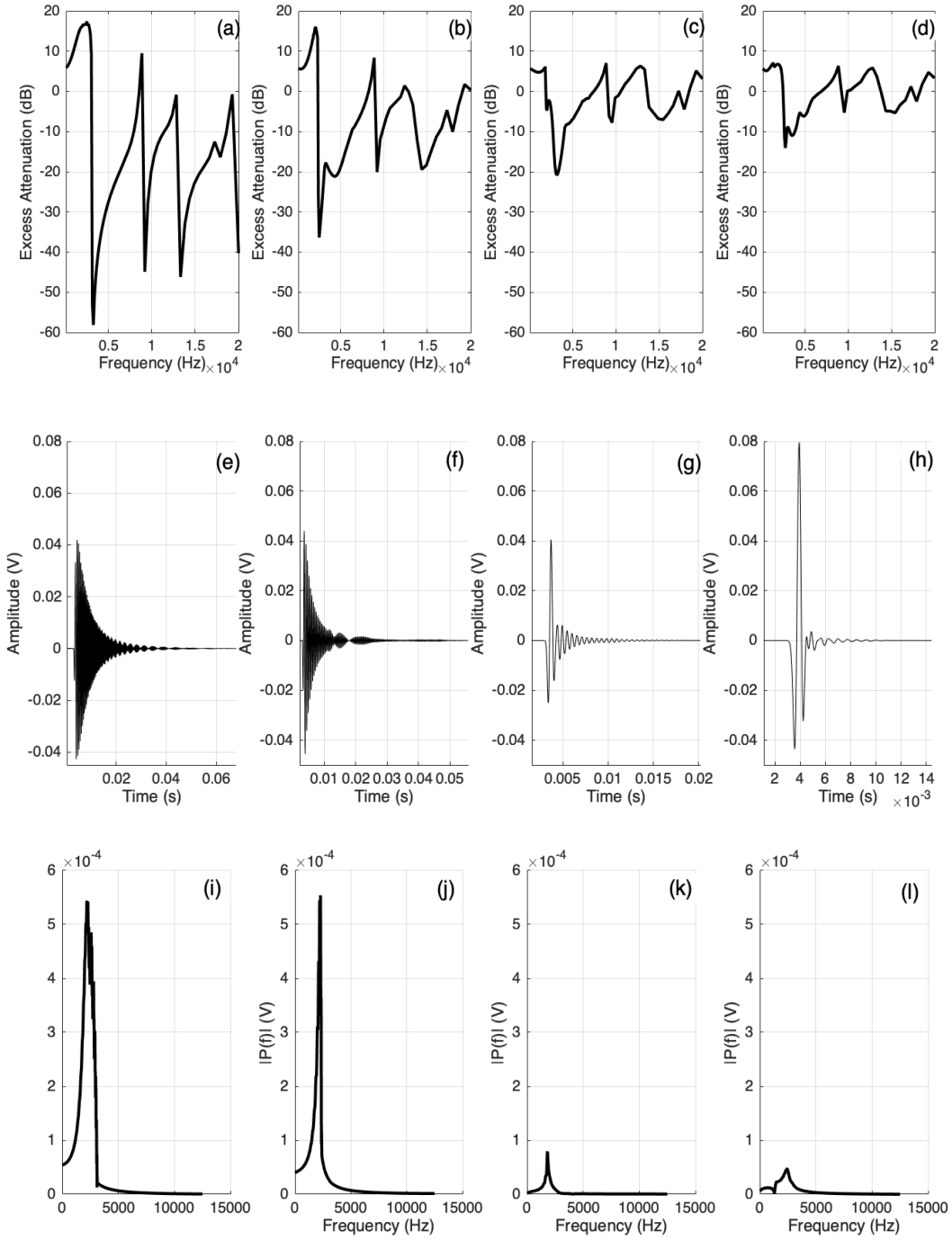

Figure 6. 42 (a) – (d) *Excess attenuation spectra obtained from a BEM simulation over strips separated by 0.02 m with a thickness of* ***(a)*** *0.005 m (41 strips),* ***(b)*** *0.035 m (19 strips),* ***(c)*** *0.065 m (12 strips) and* ***(d)*** *0.10 m (9 strips) and with a height of 0.025 m* ***(e) – (h)*** *TDBEM time-series for the above geometry* ***(i) – (l)*** *Spectrum of the wave-train following the arrival of the main pulse in figures (e) – (h) obtained via a 4096 points FFT.*

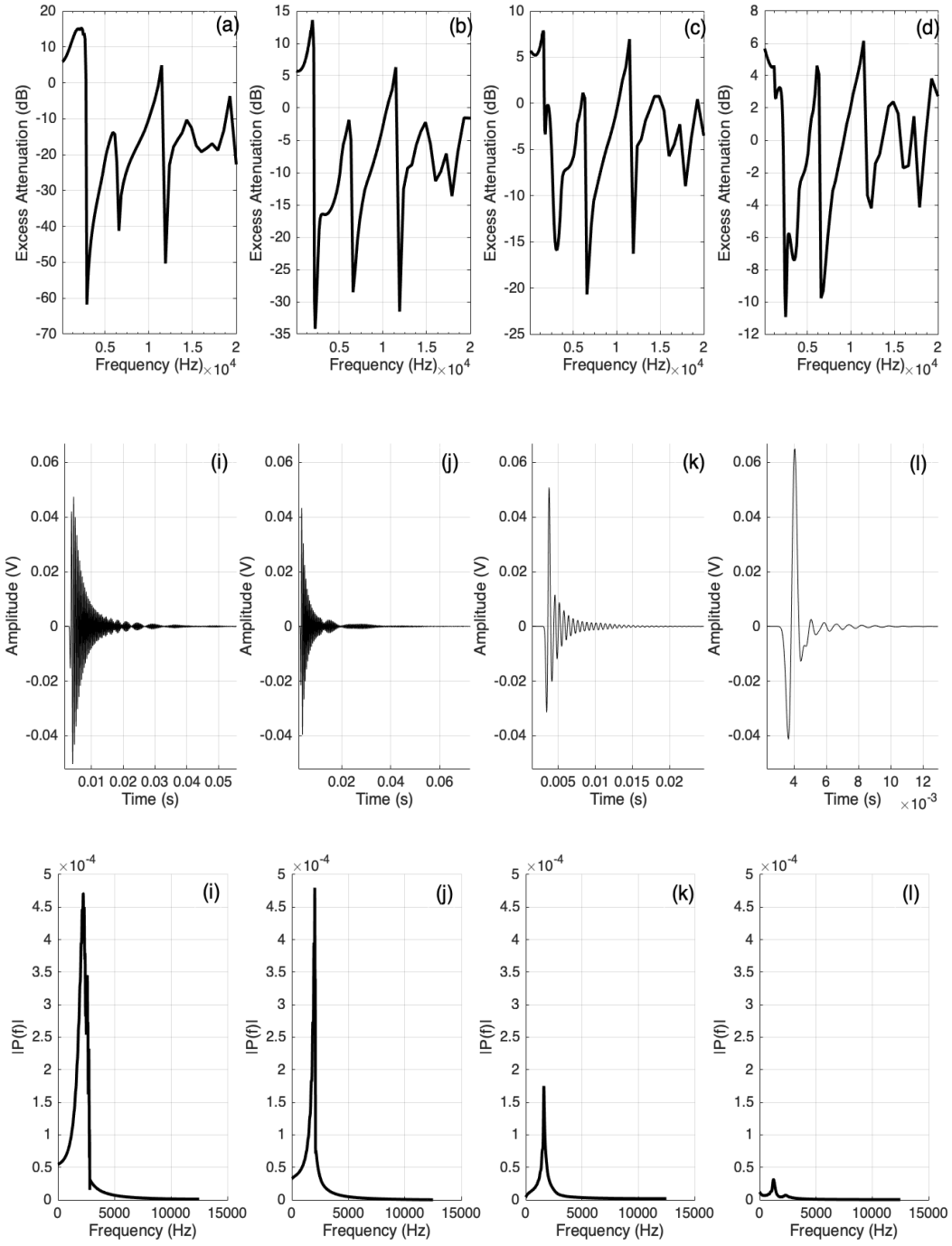

Figure 6. 43 (a) – (d) *Excess attenuation spectra obtained from a BEM simulation over strips separated by 0.03 m with a thickness of* ***(a)*** *0.005 m (29 strips),* ***(b)*** *0.035 m (16 strips),* ***(c)*** *0.065 m (12 strips) and* ***(d)*** *0.10 m (8 strips) and with a height of 0.025 m* ***(e) – (h)*** *TDBEM time-series for the above geometry* ***(i) – (l)*** *Spectrum of the wave-train following the arrival of the main pulse in figures (e) – (h) obtained via a 4096 points FFT.*

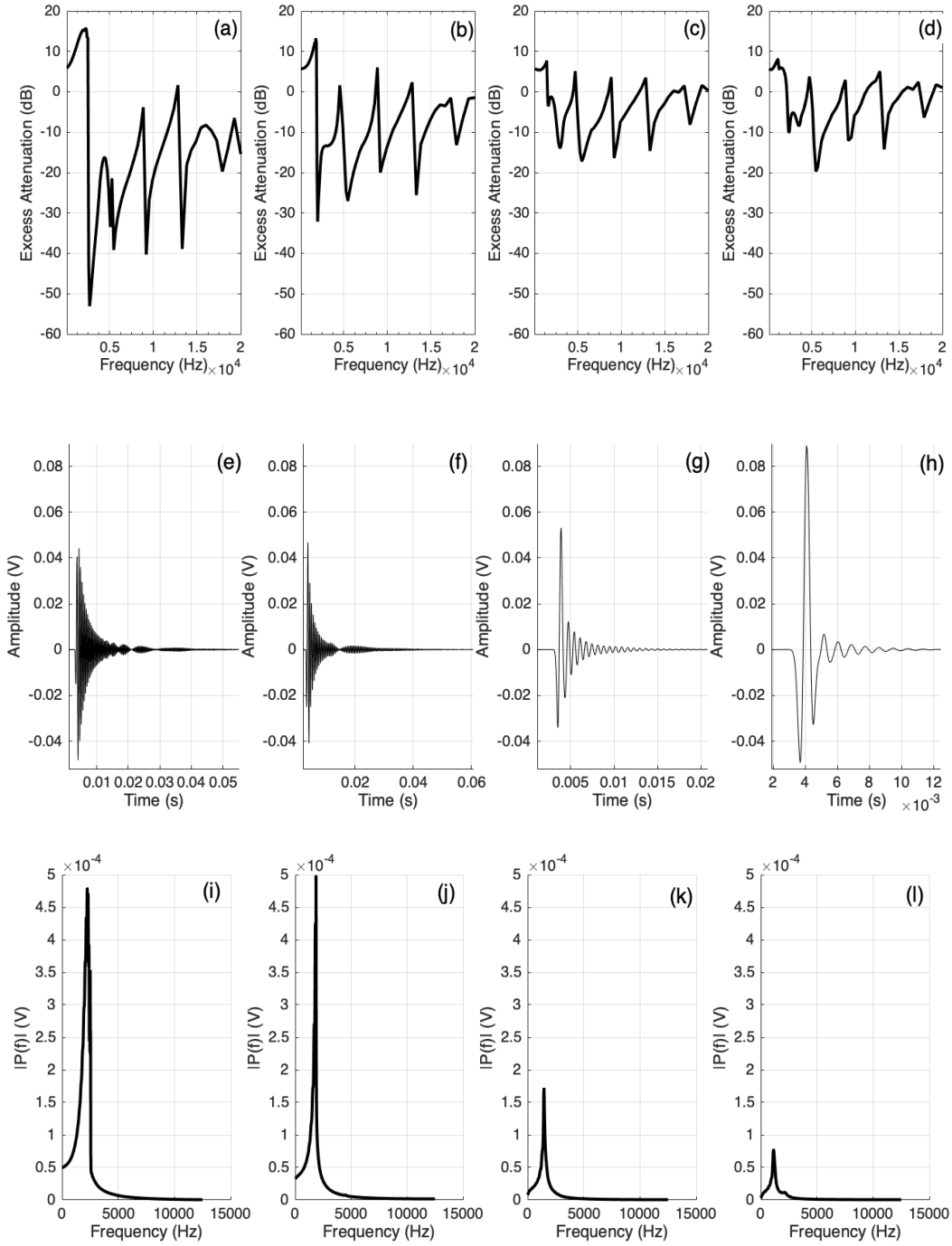

Figure 6. 44 (a) – (d) *Excess attenuation spectra obtained from a BEM simulation over strips separated by 0.04 m with a thickness of* ***(a)*** *0.005 m (23 strips),* ***(b)*** *0.035 m (14 strips),* ***(c)*** *0.065 m (10 strips) and* ***(d)*** *0.10 m (8 strips) and with a height of 0.025 m* ***(e) – (h)*** *TDBEM time-series for the above geometry* ***(i) – (l)*** *Spectrum of the wave-train following the arrival of the main pulse in figures (e) – (h) obtained via a 4096 points FFT.*

6.5 Effect of Varying Number of Edges

From the results in figure 12 to figure 6.20 it appears that for the thinnest strips and smallest gaps, the surface appears to behave more like a slit-pore layer due to the widths of the associated gaps being less than 50% of the layer depth. In the time-domain plots, a smaller spacing produces a much longer wave-train following the main pulse at between 4 ms and 10 ms. The peak frequency of this wave-train for the smallest gap of 0.005 m (figure 6.20(i)) is 2423 Hz whereas the excess attenuation peaks at 2247 Hz. This slight discrepancy can be attributed to the influence of other effects. First, the ground effect minimum associated with the ground and the source-receiver geometry could have a frequency content close to that of the enhancement feature. Secondly, the high number of edges introduces many scattered components which interfere with the surface wave at the receiver. This is also apparent in the time-series outputs since there appears to be a beat-like pattern in the wave-train following the main pulse (see figures (e) in 6.11 – 6.14 and 6.17 – 6.20) indicative of the spatial interference between the surface wave and other contributions. The effect of surface wave interference with the direct signal is investigated in section 6.3.2. However, there are many reflected contributions that can interfere at the receiver and their effect on the patterns observed in pressure maps require further investigation. In every case, there will be effects from the ends of the array which will contribute to the overall signal detected at the receiver, which require further investigation also.

A surface with a high number of edges per wavelength behaves as a slit-pore impedance surface with a high reactive component to its effective impedance. The effect of visco-thermal dissipation at the slit walls means the surface wave is dispersive where its speed is dependent on its frequency (51). The BEM software used throughout this project does not include visco-thermal interactions which results in the surface wave peaks being less sharp

than that predicted by the slit-pore model. Modelling the surface geometries above as a slit-pore impedance layer yields interesting results. As the strip thickness increases for a given gap, the effective porosity decreases and thus the magnitude of the effective reactance decreases. The result is a slightly weaker surface wave that is higher in frequency, travels at an increased speed and is less dispersive. As the effective porosity is increased by increasing the gap between elements, the surface wave speed decreases and the dispersion increases. This shows that BEM is not able to accurately predict surface wave properties for smaller spacings that resemble slit-pore impedance surfaces. Decreasing the number of edges per wavelength gives rise to narrow-band quarter wavelength resonances which results in sharper excess attenuation peaks. The BEM used throughout this project is useful for determining the topographical effects of the strip surface on the sound field but not necessarily the surface wave properties.

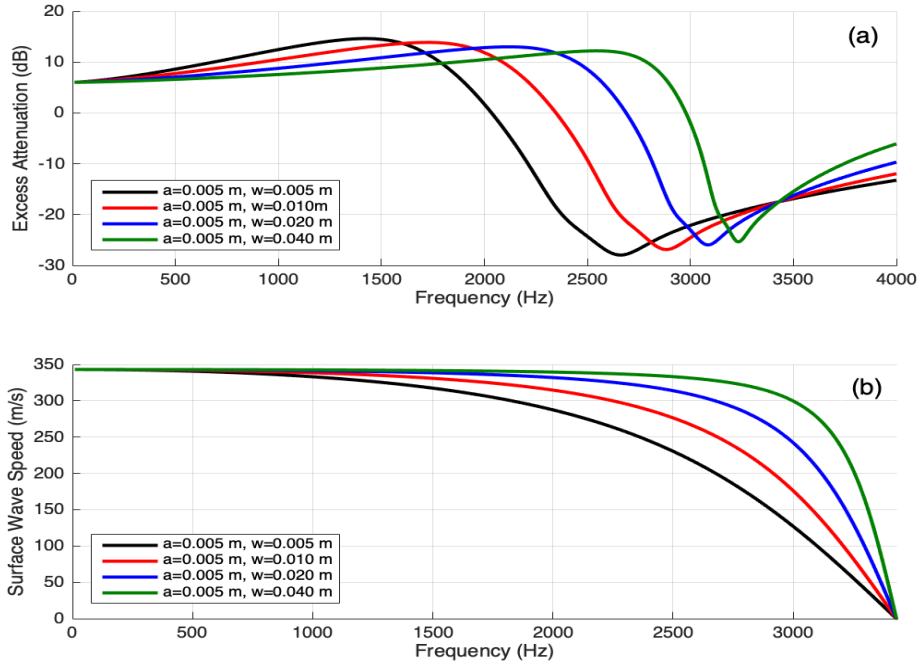

Figure 6. 45 (a) *Excess attenuation for strips modelled as an effective slit-pore impedance layer with a fixed gap of 0.005 m and a thickness of 0.005 m, 0.10 m, 0.20 m and 0.40 m* ***(b)*** *Surface wave speed over these surfaces.*

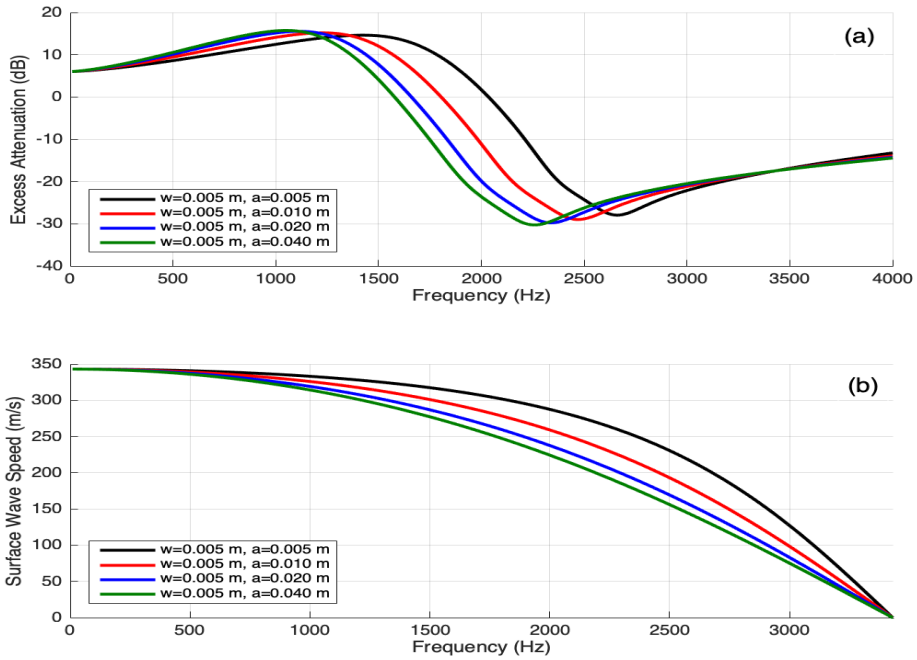

Figure 6. 46 (a) *Excess attenuation for strips modelled as an effective slit-pore impedance layer with a fixed thickness of 0.005 m and a gap of 0.005 m, 0.10 m, 0.20 m and 0.40 m* ***(b)*** *Surface wave speed over these surfaces.*

To investigate the influence of quarter-wavelength resonances over such a layer, the speed of sound inside the layer must be determined. However, the sound speed in a slit-pore impedance layer is frequency dependent. It can be calculated via the ratio of the real part of the complex propagation constant and the angular frequency. Figure 6.46 shows the sound speed within the slit-pore layer as a function of frequency and shows that the speed is 343 ms^{-1} at all frequencies. For the slit-pore impedance layer simulated in figure 6.2, the surface wave peak is around 1450 Hz. The quarter-wavelength layer resonance is dependent on the height of the strips and thus equation (QWR equation) predicts a quarter-wavelength layer resonant frequency in the slit-pore layer of 3389 Hz. This shows that for a periodic strip surface with a small gap and a high number of edges per wavelength, the gap resonance has

little influence on the surface wave, which is generated primarily as a result of the combination of the vertical motion of air between the strips and the horizontal motion of the incident sound.

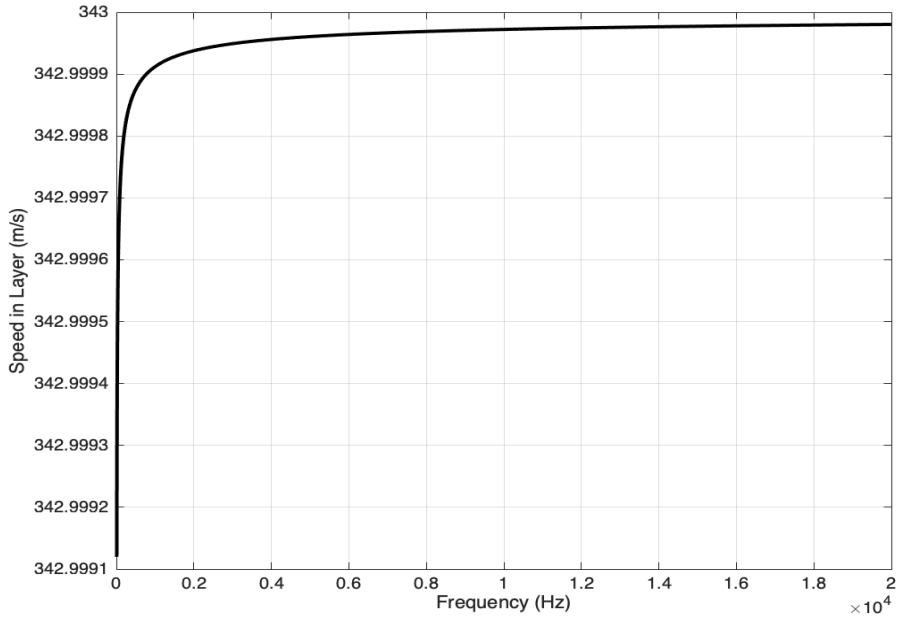

Figure 6. 47 *The sound speed within a slit-pore layer as a function of frequency.*

As the number of edges per wavelength decreases, the surface behaves less like a slit-pore layer since the effective reactance of the surface decreases (see fig 5.4). This results in weaker surface wave generation and a greater influence from the quarter-wavelength resonances generated in the gaps. This is indicated by sharper excess attenuation peaks since the gap resonances are narrowband and therefore non-dispersive. The predicted end corrections for every strip geometry in figures 6.12 to 6.20 are outlined in tables 6.9 and 6.10. For the strip surface with a thickness and gap of 0.005 m, the end correction is sufficiently small that that the quarter-wavelength resonant frequency will be near 3389 Hz.The end correction is slightly larger since the neighbouring quarter-wavelength resonances interact resulting in larger regions of high pressure above the strip surface. Further to this,

contributions from Bragg diffraction become involved as the number of edges per wavelength reduces. Bragg diffraction occurs when two diffracted waves scatter coherently from points on a crystal lattice, in this case the strip edges. These waves interfere both constructively and destructively depending on the path length difference between them. The Bragg frequencies, f_{br} at which interference occurs is derived from Bragg's law and is given by,

$$f_{br} = \frac{nv}{2d\sin\alpha}, \quad n = 1, 2, 3... \tag{0.107}$$

where v is the sound velocity at the Bragg frequency, d is the centre-to-centre spacing between elements and α is the angle of incidence. Bragg's law as stated in (6.25) assumes scattering from infinitesimal points and is thus independent of the size of the scattering elements. The calculated Bragg frequency for every geometry in figures 6.35 to 6.43 are shown in table 6.6 and compared to the frequencies of the first excess attenuation peaks.
In the case of the strip surface with a 0.005 m gap and thickness (figure 6.17 (a)), the predicted Bragg frequency is 17150 Hz and so the peak in the excess attenuation spectrum is mainly due a surface wave generated in the slit-pore impedance layer. As the thickness is increased for this case, the porosity decreases resulting in a reduction in the imaginary part of the effective impedance. This results in a reduction in the surface wave magnitude and an increased influence on the signal enhancement from the generation of quarter-wavelength resonances and Bragg diffraction. In the case where the gap is 0.005 m and the thickness is 0.035 m, the predicted Bragg frequency is 4288 Hz and so contributions from Bragg diffraction may have an increased influence along with quarter-wavelength resonances on the excess attenuation spectrum and the wave-train spectra. In the case of the 0.10 m thickness, the first Bragg frequency is predicted at 1633 Hz which implies that the main contribution to excess attenuation peaks is from Bragg diffraction and surface wave contribution is

negligible. This implies that the larger strip thicknesses increase the relative contribution of Bragg diffraction.

As the number of edges per wavelength decreases, the frequencies associated with the gap resonances and Bragg diffraction also decrease. This increases their relative contribution to the enhancement features observed in the excess attenuation spectra.

In summary, it has been shown that surface wave generation is strongest when the gap is small so that there is a high number of edges per wavelength and a high imaginary component to the effective impedance. As the gap is increased, the frequency of the gap resonance and the Bragg contributions decreases and becomes more influential. This is indicated by sharper peaks in the excess attenuation due to more narrow-band contributions.

Thickness (m)	0.005		0.02		0.03		0.04	
	Bragg Frequency (Hz)	Frequency of First EA Peak (Hz)	Bragg Frequency (Hz)	Frequency of First EA Peak (Hz)	Bragg Frequency (Hz)	Frequency of First EA Peak (Hz)	Bragg Frequency (Hz)	Frequency of First EA Peak (Hz)
Gap (m)								
0.01	11433	1938	5717	2606	4288	2420	3430	2420
0.03	4900	1938	3430	2011	2858	1867	2450	1938
0.06	2638	1938	2144	1671	1906	1610	1715	1441
0.10	1633	1441	1429	1242	1319	1153	1225	1071
Gap (m)	0.005		0.02		0.03		0.04	
	Bragg Frequency (Hz)	Frequency of First EA Peak (Hz)	Bragg Frequency (Hz)	Frequency of First EA Peak (Hz)	Bragg Frequency (Hz)	Frequency of First EA Peak (Hz)	Bragg Frequency (HZ)	Frequency of First EA Peak (Hz)
Thickness (m)								
0.005	17150	2087	6860	2511	4900	1938	3811	224 7
0.035	4288	2807	3118	2087	2638	1938	2287	1799
0.065	2450	2247	2018	1799	1805	1551	1633	1441
0.100	1633	2705	1429	1289	1319	1153	1225	1071

Table 6. 6 *Calculated Bragg frequencies compared with peaks in excess attenuation spectra in figures 6.*

First Peak						
Thickness (m)			0.005	0.02	0.03	0.04
Gap (m)	Minimum End Correction	Maximum End Correction	End Correction	End Correction	End Correction	End Correction
0.01	0.003	0.008	0.0189	0.0076	0.0101	0.0115
0.03	0.009	0.023	0.0189	0.0173	0.0206	0.0189
0.06	0.018	0.047	0.0189	0.0260	0.0279	0.0342
0.10	0.03	0.80	0.0342	0.0437	0.0491	0.0548

Table 6. 7 *End corrections for the enhancement features at each frequency associated with elements varying in spacing for a fixed thickness.*

First Peak						
Gap (m)			0.005	0.02	0.03	0.04
Thickness (m)	Minimum End Correction	Maximum End Correction	End Correction (m)	End Correction (m)	End Correction (m)	End Correction (m)
0.005	0.0015	0.0039	0.0052	0.0088	0.0129	0.0129
0.035	0.0105	0.0274	0.0158	0.0158	0.0189	0.0224
0.065	0.0195	0.0511	0.0129	0.0224	0.0299	0.0342
0.100	0.0300	0.0800	0.0064	0.0412	0.0491	0.0548

Table 6.8 *End corrections for the enhancement features at each frequency associated with elements varying in thickness for a fixed spacing.*

6.5.1 Bragg Diffraction for Larger Gaps.

To investigate the Bragg-diffraction effect over a longer array, a series of simulations have been carried out for large strip separations with an increased source-receiver geometry. The source-receiver separation was set at 2.00 m and the source and receiver heights were set at 0.03 m. The thickness and height of the strips were 0.04 m and 0.02 m respectively. The gaps were set at 0.125 m, 0.25 m and 0.5 m corresponding to 13, 7 and 5 strips, respectively. The geometry was chosen such that there was one element per wavelength which is in agreement with Bragg theory.

Gap (m)	**First Bragg Frequency (Hz) (n=1)**	**First Excess Attenuation Peak frequency (Hz)**
0.125	1039	950
0.250	591	523
0.500	318	281

Table 6. 9 *Frequency of the first excess attenuation peak for strip gaps of 0.0125 m, 0.250 m and 0.500 m and the correspoinding Bragg diffraction frequencies calculated from equation 6.23.*

.

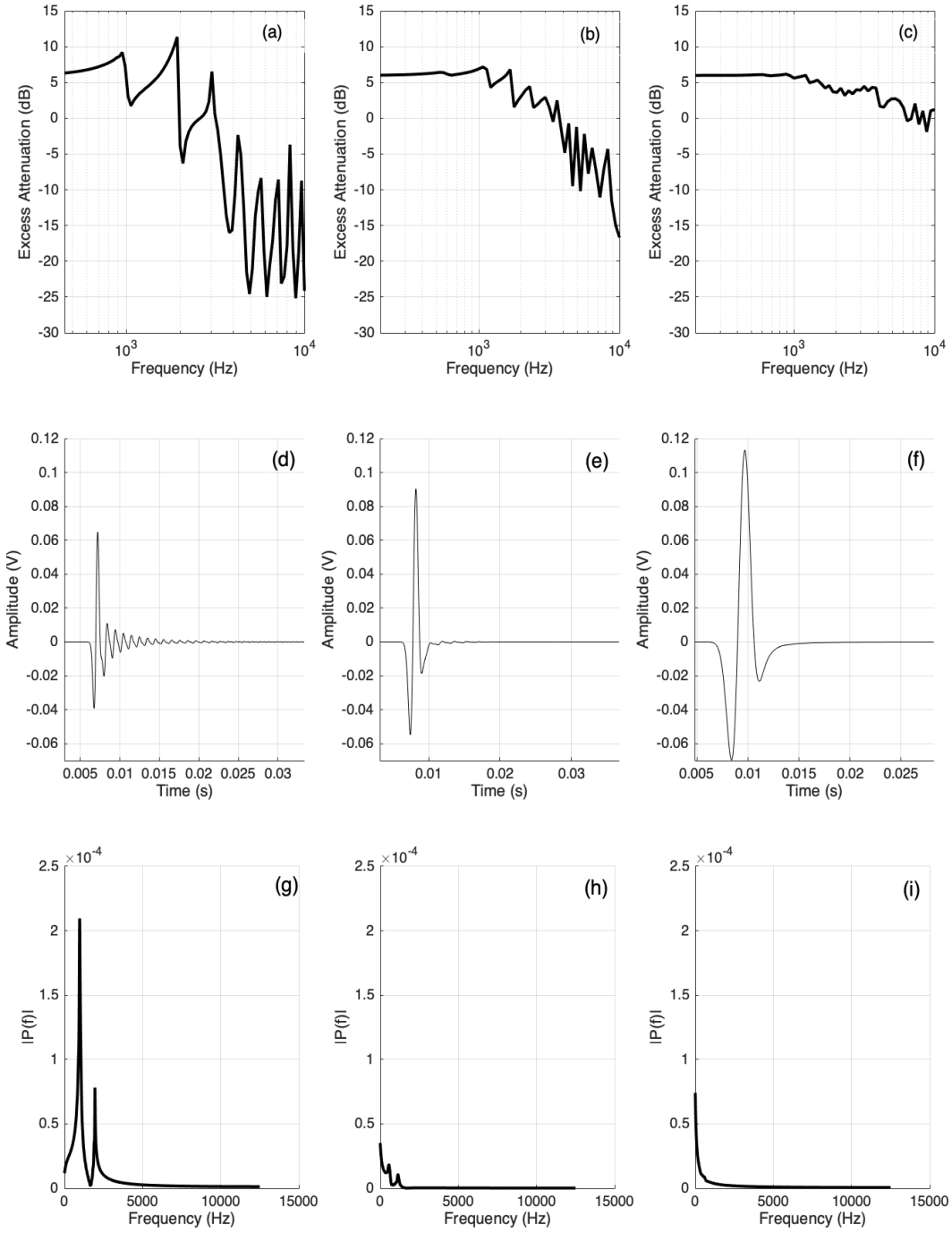

Figure 6. 48 (a) – (c) *Excess attenuation spectra obtained from a BEM simulation over strips with a thickness of 0.04 m separated by* ***(a)*** *0.0125 m,* ***(b)*** *0.25 m and* ***(c)*** *0.50 m with a height of 0.025 m* ***(d) – (f)*** *TDBEM time-series for the above geometry* ***(g) – (i)*** *Spectrum of the wave train following the arrival of the main pulse in figures* ***(d) – (f)*** *obtained via a 4096 point FFT.*

There is good agreement between the frequencies of the first peaks in the excess attenuation spectra and the Bragg frequencies calculated from the geometry associated with the spectra. One assumption in Bragg theory is that the periodicity remains constant between scattering elements. To investigate the effect on the sound field of aperiodicity, the spacing between elements was varied The results are displayed in figure 6.23 and it is clear to see that the peaks due to Bragg diffraction have diminished. The peaks in the spectra are a result of constructive interference between scattered waves from the tops of the strips and it is also clear that the amplification potential of such an array is inferior to that of a periodic array.

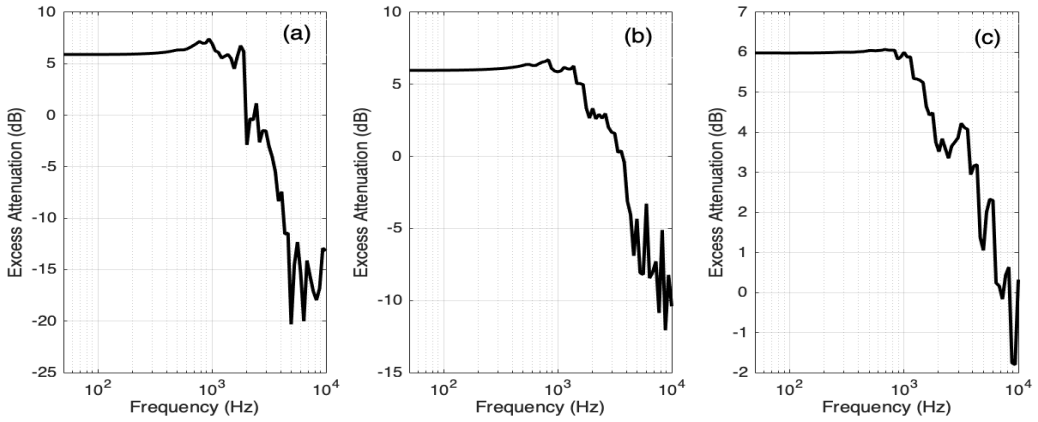

Figure 6. 49 (a) *Excess attenuation spectrum for 13 strips with varied spacing* ***(b)*** *Excess attenuation for 7 strips with varied spacing and* ***(c)*** *Excess attenuation for 4 strips with varied spacing.*

.

Chapter 7

Conclusions

7.1 Summary of Conclusions

This project has provided an original, in-depth study into the sound field generated above periodically-rough surfaces. The aim of this project was to improve the performance of (audio-frequency) acoustic and seismic sensors. The sensors themselves run on every-day lightweight batteries and so increasing the energy demand on the sensors by increasing sensitivity and therefore requiring heavier batteries, is not desirable. Periodically-spaced rectangular strips create a surface that supports the generation of air-borne acoustic surface waves which trap sound close to the ground at a frequency, dictated by the geometry, which results in enhancement at that frequency. This improves the performance of the sensor without actually modifying the sensor itself.

The generation of surface waves is well documented in the literature. This provides a potentially useful mechanism for the enhancement of acoustic signals. Experimental and numerical results yield simple relationships between surface wave frequency and magnitude and the geometry and topography of the strip surface a which simplifies the design of surfaces for acoustic signal-enhancement. Furthermore, new enhancement features associated with the finite width and periodicity of the structure allow for further enhancement at a broad range of frequencies with further inreases the enhancement potential of periodically-rough surfaces.

7.2 Conclusions

A surface wave is identifiable as a peak in excess attenuation spectra with magnitude greater than the maximum enhancement achievable through constructive interference between the direct wave and the reflected wave off an acoustically rigid surface i.e. 6 dB. It also has a speed slower than that of sound in air and is identifiable as a late-arrival or an extended wave-train i.e. 'ringing' in the time-domain. Measurements involved the transmission of a Maximum Length Sequence (MLS) and Ricker pulses across a strip array for excess attenuation and time-domain measurements respectively. Indeed, a peak above 6.02 dB was observed in excess attenuation spectra and a wave-train followed from the arrival of the Ricker pulse in the time-domain. Plotting the amplitude of this wave train at a chosen point in time against increasing receiver height yielded the expected exponential decrease. It was also found that increasing the gap (and therefore increasing the effective porosity) made the surface less likely to support the generation of a surface wave due a decrease in the effective reactance.

The broad nature of the excess attenuation peak implied that the surface wave generated over a slit-pore impedance layer with a high reactive component is dispersive with its speed dependent on frequency. More interestingly, as the gap is increased and the number of edges per wavelength reduced, other signal-enhancing effects that contribute to enhancement at a wider range of frequencies than just that of the surface wave. These 'extra enhancement features' are not generated when sound propagates over a slit-pore impedance layer and are therefore a result of the periodicity and structure of the strip array and had not previously been reported in literature.

An original study in which pressure maps of the total field over the strips are generated show that the surface wave arises as a result of quarter-wavelength resonances forming within the gaps between strips. These high-pressure regions couple together over the top of the strip array and result in an increased end correction than expected over a strip surface with a low number of edges per wavelength. Varying the periodicity of the array reduced the extra excess attenuation peaks which confirmed that the enhancement potential is greater for a periodic structure.

There are enhancement effects in every case due to the finite-array width effect. This effect arises as a result of reflections due to the impedance discontinuity at the strip edges and can be reduced via the introduction of absorbing material to the ends of the array. These waves constructively interfere at the receiver and thus allow for further signal enhancement.

There are further contributions from the diffracted waves that are scattered from the strip edges. For a strip surface with a high number of edges per wavelength, there is greater signal enhancement over a wider range of frequencies. Furthermore, the quarter-wavelength resonances interact with one another and couple more strongly. Once the gap is increased, and the number of edges per wavelength reduced, the gap resonances act individually and couple less strongly. The surface begins to act less like a slit-pore impedance layer and more like a rough surface for near-grazing sound propagation.

Another interesting feature is the periodic regions of high and low pressure that exist within the gap resonances. These complex patterns arise as a result of interference between the surface wave and the direct and reflected signals or ‘edge effects.’ This has been confirmed by a study of the waveform generated between the spatial interference of two waves travelling at different speeds.

An investigation the effect of varying the strip thickness and gap on the observed enhancement features yielded interesting results. First, to investigate the variation of surface

wave magnitude and vertical attenuation with strip height, the surface was modelled as a hard-backed slit-pore impedance layer. It was found that the surface wave magnitude plateaus at a strip height of 0.06 m and so the height of the roughness element will not affect the surface wave magnitude beyond this limit. It was also found that the vertical attenuation reduces logarithmically with strip height. The effect of strip height on surface wave frequency was investigated numerically using BEM. It was found that the frequency of the surface wave decreases exponentially with strip height. This suggests that the higher the strip the stronger, and lower in frequency, is the surface wave produced. However, the exponential relationship means it becomes increasingly difficult to enhance frequencies lower than around 500 Hz.

The effect of varying strip thickness and the gap between strips was also investigated numerically using BEM and the resulting time-response modelled using the TDBEM program. This program was developed to look at the enhancement features as later arrivals in the time-domain and calculates the response through the convolution of the spectra of a source-function, namely a Ricker pulse, and a transfer function which is generated as an output from the BEM program. It has already been mentioned that as the spacing between the strips increases, the effective reactance decreases so the surface produces weaker surface waves. It was found that the physical mechanism which drives the generation of these enhancement features depends on the number of edges per wavelength. From this, three primary conclusions have been drawn:

- For a high a number of edges per wavelength, the surface behaves like a slit-pore impedance layer with a large effective reactance. The surface wave generated in this case is associated with the combination of the verticle motion of the air within the pores and the horizontal motion of the incident sound field.

- As the number of edges per wavelength decreases, the surface produces weaker surface waves since there is a reduction in the effective reactance of the surface. The frequency of the gap resonance (associated with the height of the strips) reduces since the end correction (associated with the gap) becomes larger. The surface wave becomes less influential and the gap resonances become the dominant enhancement mechanism.
- Once the number of edges decreases further and approaches one per wavelength, the strips begin to behave like individual Bragg scatterers. The Bragg frequency also reduces as the spacing between strips is increased. This is characterised by sharp peaks in the excess attenuation spectra which correspond almost perfectly to the predicted frequencies calculated using Bragg's formula. Once the gap is increased beyond 0.25 m, the strips begin to act independently, and no signal enhancement is achieved.

When determining surface wave properties individually, the BEM used throughout this project fails to account for the influence of visco-thermal dissipation at the strip walls. This results in sharper surface wave peaks than predicted by a slit-pore impedance model. However, BEM *does* predict the effects associated with interaction between the sound field and the strip array. This should be taken into consideration when using strip arrays as effective impedance surfaces.

The numerical studies have suggested that it is possible to achieve signal enhancement near 1 kHz even with as few as eight 0.0253 m high strips. The geometries required for other frequency targets are easily calculated from basic formulae for the frequency of quarter-wavelength resonators and Bragg-frequencies. Maximum enhancement however is achieved

by a surface with a high number of scattering edges per wavelength which requires thin strips to be spaced close together between source and receiver.

These signal-enhancing mechanisms are not detected by a geophone through acoustic-seismic coupling since the gap resonances and associated surface waves are heavily damped by the absorbing ground surface.

7.2 Suggestions for Future Work

The models outlined throughout the thesis have been validated under anechoic conditions. Future work should involve applying and validating these models outdoors. Moreover, the exploitation of acoustic-seismic coupling at the receiver has been explored using sand. Hardening the ground surface between strips could result in enhanced signals at collocated seismic sensors. Field measurements with a strong acoustic source are required for this.

As mentioned, there are complex patterns superimposed onto the gap resonances. These arise as a result of interference between direct and reflected contributions. Further work into this could involve varying the periodicity and introducing a finite impedance to the strip edges. This would give a greater understanding of exactly how the sound field interacts with the surface roughness. Furthermore, Particle Image Velocimetry (PIV) methods could be exploited to investigate the nature of the surface wave at the excess attenuation maxima. The generation of elliptical particle motion associated with the surface wave could be explored in detail.

Daigle & Stinson [30] found that their low frequency strip array design was strongly directional which can be useful in locating acoustic sources and increases the potential for use of these strip arrays. Future work should investigate the directionality of strip array geometries considered in this thesis.. A 3D-BEM model would benefit this work.

Bibliography

[1] Lord Rayleigh (1885), 'On waves propagated along the Plane Surface of an Elastic Solid', *Proc. London Math. Soc.*, **17**, 4 – 11

[2] K. Attenborough, K. M. Li, K. Horoshenkov (2007), *Predicting Outdoor Sound*, Taylor & Francis, Abingdon

[3] A. Sommerfield (1909), 'On the propagation of waves in wireless telegraphy,' *Ann. Phys*, **28**, 665 – 737

[4] A. Banos, '*Dipole radiation in the presence of a conducting half-space,'* Pergamon Press, New York, 1996

[5] U. Ingard (1951), 'On the reflection of a spherical sound wave from an infinite plane,' *J. Acoust. Soc. Am*, **23**, 329 – 335

[6] A. R. Wenzel (1972), 'Propagation of waves along an impedance boundary', *J. Acoust. Soc. Am*, **55 (5)**, 956 – 963

[7] S. I. Thomasson (1976), 'Reflection of waves from a point source by an impedance boundary,' *J. Acoust. Soc. Am*, **59**, 780 – 785

[8] L. M. Brekhovskikh (1959), 'Surface waves in acoustics,' *Sov. Phys. Acoust,* **5**, 3 – 12

[9] L. M. Brekhovskikh (1960), *'Waves in Layered Media (Translated from Russian by D. Liberman and R. T. Beyer)',* Academic Press, London & New York, 44 – 61

[10] K. M. Ivanov-Shits, F. V. Rozhin (1960), 'Investigation of surface waves in air,' *Sov. Phys,* **5**, 510 – 512

[11] R. J. Donato (1976), 'Propagation of a spherical wave near a plane boundary with complex impedance,' *J. Acoust. Soc. Am*, **60**, 34 – 39

[12] R. J. Donato (1978), 'Model experiments on surface waves', *J. Acoust. Soc. Am*, **63(3)**, 700 – 703

[13] K. Attenborough, S. I. Hayek, J. M. Lawther (1980), 'Propagation of sound above a porous half-space,' *J. Acoust. Soc. Am*, **68** (5), 1493 – 1500

[14] R. Raspet, G. E. Baird (1988), 'The acoustic surface wave above a complex impedance plane.' *J. Acoust. Soc. Am*, **85** (2), 638 – 640

[15] I. Tolstoy (1973), *Wave Propagation*, McGraw Hill, USA

[16] K. Attenborough, T. L. Richards (1988), 'Solid particle motion induced by a point source above a poroelastic half-space,' *J. Acoust. Soc. Am*, **86** (3), 1085 – 1092

[17] J. F. Allard, G. Jansens, G. Vermeir, W. Lauriks (2002), 'Frame-borne surface waves in air-saturated porous media,' *J. Acoust. Soc. Am*, **111** (2), 690 – 696

[18] I. Tolstoy (1979), 'The scattering of spherical pulses by slightly rough surfaces,' *J. Acoust. Soc. Am*, **66** (4), 1135 – 1144

[19] H. Medwin, G. L. D'Spain, E. Childs, S. J. Hollis (1984), 'Low-frequency grazing propagation over periodic steep-sloped rigid roughness elements,' *J. Acoust. Soc. Am*, **76** (6), 1774 – 1790

[20] I. Tolstoy (1981), 'Coherent sound scatter from a rough interface between arbitrary fluids with particular reference to roughness element shapes and corrugated surfaces,' *J. Acoust. Soc. Am*, **72** (3), 960 – 972

[21] G. A. Daigle (1989), 'Surface waves above porous ground surfaces,' *J. Acoust. Soc. Am. Suppl*, 1 **85**, 82

[22] C. Hutchinson-Howorth, K. Attenborough (1992), 'Model experiments on air-coupled surface waves,' *J. Acoust. Soc. Am*, **63** (3), 2431 – 2436

[23] G. A. Daigle, M. R. Stinson, D. I. Havelock (1996), 'Experiments on surface waves over a model impedance plane using acoustical pulses,' *J. Acoust. Soc. Am*, **99** (4), 1993 – 2005

[24] M. R. Stinson, G. A. Daigle (1997), 'Surface wave formation at an impedance discontinuity,' *J. Acoust. Soc. Am*, **102** (6), 3269 – 3275

[25] W. Zhu, M. R. Stinson, G. A. Daigle (2002), 'Scattering from impedance gratings and surface wave formation,' *J. Acoust. Soc. Am*, **111**, 1996 – 2012

[26] Albert. D (1992), 'Observations of acoustic surface waves propagating above a snow cover,' *Proceedings of the 5th International Symposium of Long Range sound Propagation,',* 10 – 16

[27] L. Kelders, J. F. Allard, W. Lauriks (1998), 'Ultrasonic surface waves above rectangular groove gratings,' *J. Acoust. Soc. Am*, **103** (5), 2730 – 2733

[28] W. Lauriks, L. Kelders, J. F. Allard (1998), 'Surface waves above gratings having a triangular profile,' *Ultrasonics*, **36**, 865 – 871

[29] J. F. Allard, L. Kelders, W. Lauriks (1998), 'Ultrasonic surface waves above a doubly periodic grating,' *J. Acoust. Soc. Am*, **105** (4), 2528 – 2531

[30] W. Zhu, G. A. Daigle, M. R. Stinson (2003), 'Experimental and numerical study of air-coupled surface waves generated above strips of finite impedance,' *J. Acoust. Soc. Am*, **114** (3), 1243 – 1253

[31] G. A. Daigle, M. R. Stinson (2004), 'Passive amplification and directivity from air-coupled surface waves generated above a structured ground,' *J. Acoust. Soc. Am*, **115** (5), 1988 – 1992

[32] I. Bashir (2014), *'Acoustical Exploitation of Rough, Mixed Impedance and Porous Surfaces Outdoors,'* PhD Thesis, The Open University

[33] I. Bashir, S. Taherzadeh, K. Attenborough (2013), 'Surface waves over periodically-spaced strips', *J. Acoust. Soc. Am,* **134** (6)

[34] H. Bougdah, I. Ekici, J. Kang (2006), 'A laboratory investigation of noise reduction by riblike structures on the ground', *J. Acoust. Soc. Am,* **120** (6), 3714 – 3722

[35] C. D. Field, F. R. Fricke (1998), 'Theory and applications of quarter-wave resonators: A prelude to their use for attenuating noise entering buildings through ventilation openings', *Applied Acoustics,* **53 (1 – 3)**, 117 – 132

[36] U. Ingard (1953), 'On the theory and design of acoustic resonators', *J. Acoust. Soc. Am*, **25** (6), 1037 – 1061

[37] D. Berry, S. Taherzadeh, K. Attenborough (2018), 'Acoustic pulse propagation over arrays of rigid circular cylinders on a rigid plane,' *Unpublished Manuscript*

[38] M. C. Junger (1975), 'Helmholtz resonators in load-bearing walls,' *Noise Control Engineering,* **4** (1), 17 – 25

[39] J. G. Beadle, T. Starkey, J. A. Dockrey, J. R. Sambles, A. P. Hibbins (2018), 'The acoustic phase resonances supported by a compound rigid grating,' *Nature: Scientific Reports,* **8**.

[40] R. Tayong, T. Dupont, P. Leclaire (2011), 'Experimental investigation of holes interaction effect on the sound absorption coefficient of micro-perforated panels under high and medium sound levels,' *Applied Acoustics,* **72**, 777 – 784

[41] S. M. Kirkup (2007), '*The Boundary Element Method in Acoustics,' Journal of Computational Acoustics*

[42] S. Taherzadeh, K.M Li, K. Attenborough (2001), A Hybrid BIE/FFP Scheme for Predicting Barrier Efficiency Outdoors, *J. Acoust. Soc. Am,* **110** (2), 918

[43] J. W. Cooley, J. W. Tukey (1965), 'An algorithm for the machine calculation of complex Fourier series,' *Math. Computation*, **19**, 297 – 301

[44] J. F. James (1995), '*A student's guide to Fourier transforms*,' Cambridge University Press, Cambridge

[45] W. T. Cochrane, J. W. Cooley, D. L. Flavin, H. D. Helms, R. A. Kaenel, W. W. Lang, G. C. Maling, D. E. Nelson, C. M. Rader, P. D. Welch (1967), 'What Is the Fast Fourier Transform?' *Proceedings of the IEEE*, **55** (10), 1664 – 1674

[46] A. V. Oppenheim, R. W. Schafer (2010), '*Discrete-Time Signal Processing: Third Edition,'* Pearson, New Jersey

[47] F. B. Jensen, W. A. Kuperman, M. B. Porter, H. Schmidt (1994), *'Computational Ocean Acoustics,*' American Institute of Physics, New York

[48] ISO 9613-2: *Acoustics – Attenuation of Sound During Propagation Outdoors – Part 2: General Method of Calculation* (International Standard Organisation, Geneva, Switzerland, 1996)

[49] K. Attenborough, I. Bashir, S. Taherzadeh (2011), 'Outdoor ground impedance models,' *J. Acoust. Soc. Am*, **129** (5), 2806 – 2819

[50] M. R. Schroeder (1979), 'Integrated-impulse method for measuring sound day without using pulses,' *J. Acoust. Soc. Am*, **66** (2), 496

[51] N. D. Harrop (2000), *'The exploitation of acoustic-to-seismic coupling for the determination of soil properties,'* PhD Thesis, The Open University

[52] S. Tooms, S. Taherzadeh, K. Attenborough (1991), 'Sound propagation in a refracting fluid above a layered porous medium,' *J. Acoust. Soc. Am,* **93** (1), 173 – 181

[53] J. M. Sabatier, H. E. Bass, L. N. Bolen (1986), 'The interaction of airborne sound with porous ground: The theoretical formulation,' *J. Acoust. Soc. Am,* **79** (5), 1345 – 1352

[54] M. A. Biot (1955), 'Theory of propagation of elastic waves in a fluid-saturated porous solid I. Low frequency range', *J. Acoust. Soc. Am,* **28** (2), 168 – 178

[55] K. Attenborough, I. Bashir, T. Hill, S. Taherzadeh (2011), 'Applicable ground models,' FP7 HOSANNA Deliverable 4.1

[56] Lord Rayleigh (1940), *'Theory of Sound: Vol II',* Macmillan and Company, London

[57] H. M. Bosquanet (1877), 'Notes on the theory of sound.' *The London, Edinburgh and Dublin Philosophical Magazine and Journal of Science,* **4** (24), 216 – 222

[58] A. D. Pierce (1989). '*Acoustics: An introduction to its physical principles and applications,'* Acoustical Society of America, New York